A Study of Coherent Noise in Binary Read-Out Systems and its Applications to the ATLAS SemiConductor Tracker End-Cap

INAUGURAL-DISSERTATION
zur
Erlangung des Doktorgrades
der
Fakultät für Mathematik und Physik der
Albert-Ludwigs-Universität Freiburg i. Brsg.

vorgelegt von
Ashfaq Ahmad
aus
Swabi (Pakistan)

Dekan:	Prof. Dr. R. Schneider
Leiter der Arbeit:	Prof. Dr. K. Runge
Referent:	Prof. Dr. K. Runge
Korreferent:	Prof. Dr. K. Königsmann
Tag der Verkündung des Prüfungsergebnisses:	9. Februar 2004

Contents

Chapter 1

Introduction

The goal of particle physics is to describe the most fundamental constituents of the universe and the way in which they interact with one another. The Standard Model [1, 2, 3] is the name given to the best current mathematical description of the subatomic particles and of the forces between them. This model classifies all elementary particles into two types: fermions, with half-integer quantum number of the quantum mechanical property called spin, and bosons with integer spin. The fermions make up matter and the bosons carry the known forces. The fermions of the Standard Model are either quarks, which carry a single colour charge or leptons, which do not interact strongly. Both of these fermions come in three types, which are classified in so-called families or generations summarised in Table 1.1. The leptons comprise three charged and massive particles, the electron, muon and tau, and three massless (very light) and uncharged neutrinos. A mass hierarchy is present among the three families i.e the particles of the first family are the lightest and the particles of the third family are the heaviest. All fermions have corresponding anti-particles.
The six quarks are named up, down, charm, strange, top and bottom. A proton is a combination of three valence quarks, (uud) and a neutron is (udd). Three forces are included in the Standard Model: the electromagnetic, weak and strong force. The electromagnetic force is mediated by the exchange of massless photons. Only charged fermions interact electromagnetically. All particles interact via the weak force which is mediated by three massive gauge bosons, $W^{\pm}$ and Z, which carry charges of ± 1 and 0 respectively, in units of the electronic charge. The strong force is present between particles carrying a colour charge. There are three types of colour charge denoted red, green and blue. The strong force is mediated by a massless gauge boson called gluon. The gluon carries two colour charges. The forces and their corresponding bosons are summarised in Table. 1.2. The fourth

Fermion	Family 1	Family 2	Family 3	Charge
Leptons	e^- (electron)	μ^- (muon)	τ^- (tau)	-1
	ν_e (neutrino)	ν_μ (neutrino)	ν_{tau} (neutrino)	0
Quarks	u(up)	c(charm)	t(top)	+2/3
	d(down)	s(strange)	b(bottom)	-1/3

Table 1.1: The fermions of the Standard Model and their electric charge in units of the absolute electron charge.

force, the gravitational force is not included in the Standard Model. This force is, however, so small that it is negligible between fundamental particles when compared to the other forces. For symmetry reasons, the Standard Model requires massless particles, unless some mechanism is incorporated that (partially) distorts the symmetry. The favoured mechanism is that of spontaneous gauge-symmetry breaking, caused by the Higgs field. The Higgs field [4, 5, 6] comprises a two component complex scalar field which is postulated to give mass to the weak gauge bosons but is also responsible for fermion masses. The Higgs mechanism also predicts the existence of a scalar particle, the Higgs boson, which has not yet been observed. The Large Electron-Positron Collider (LEP) [7] has extensively tested the Standard Model. The Higgs particle has not been observed and a lower limit on the Higgs mass of 114.4 GeV with 95% confidence level is given [8]. Precise measurements of the observed processes give rise to an indirect upper limit on the Higgs mass of 196 GeV with 95% confidence level [9].
The Standard Model is able to describe essentially all basic phenomena in the field of high energy physics with great accuracy. To date, no experimental evidence has been found to contradict the Standard Model[1]. There are however, reasons to believe that the Standard Model is not the ultimate description of fundamental particles and interactions. Nor has the Standard Model been totally verified i.e the sector of the theory responsible for particle masses remains untested. The Standard Model, despite its success in describing the experimental observations to an amazing precision, has some short-comings which call for other more complete theories of nature. One of the most attractive of these theories, beyond the Standard Model, is the SUperSYmmetric extension to it, i.e. SUSY. The supersymmetric models have been discussed in recent years and guide us where to look for new physics beyond the Standard Model. Although the particle content of these models is quite rich and although they introduce yet more parameters (> 100) into the theory, some restricted versions of SUSY exist, making it possible to perform searches and studies. One of these models is the Minimal Su-

[1]There is good experimental evidence [10, 11, 12] that neutrinos have a small mass. In the Standard Model neutrinos are massless but massive neutrinos could be incorporated into the theory without making fundamental changes.

Boson	Interaction	Mass(GeV)	Spin
γ (photon)	Electromagnetic	0	1
$W^{\pm}$	Weak (charged current)	$m_W = 80.43 \pm 0.05$	1
Z	Weak (neutral current)	$m_Z = 91.1882 \pm 0.0022$	1
$8\times g$(gluon)	Strong	0	1

Table 1.2: The three fundamental forces described by the Standard Model and the associated gauge bosons.

persymmetric extension to the Standard Model (MSSM) with a rich Higgs sector including five Higgs bosons, three neutral and two charged, instead of the single neutral Higgs in the minimal version of the Standard Model.

It is obvious that based on these arguments any future experiment should aim at the question of the symmetry breaking mechanism and at searching for the Higgs particle(s). The Large Hadron Collider (LHC) [13], which will replace LEP at CERN, is the machine which will address these question. The LHC is a pp collider, with a centre of mass energy of 14 TeV, scheduled to start operation in 2007. At the LHC two general purpose experiments are ATLAS [14] and CMS [15]. The main physics goals of the ATLAS experiment are,

- Search for the Higgs Boson: ATLAS will look for the Standard Model Higgs boson in various decay channels to reconstruct from these what happened immediately after the collision. The ATLAS experiment has the potential to discover the Higgs boson irrespective of its mass (provided it is below 1 TeV). A Higgs can decay in many different ways and discovery potential is given by the signal rates and the signal-to-background ratios in various mass regions. The ATLAS collaboration requires good efficiency and resolution for the most important decay channels: $H \rightarrow \gamma\gamma$ for the lowest mass range and $H \rightarrow b\overline{b}$ and $H \rightarrow ZZ^{(*)} \rightarrow 4l$ for intermediate and high masses. A detailed analysis of the detection of the Standard Model Higgs boson in ATLAS is presented in [18, 19].

- B-physics: A challenge in high energy physics is understanding the asymmetry between matter and anti-matter. Decays of short-lived particles can be used to study this asymmetry, e.g by looking with high precision at branching ratios into different decay channels. Mesons and baryons containing bottom quarks are a promising probe into the field of matter antimatter asymmetry. By studying b-decays with great precision, it is possible to determine whether the observed asymmetry is within or exceeding the boundaries defined by the Standard Model.

- Electroweak: The precision measurements of the top-quark and the W boson masses, and of the electroweak gauge boson couplings. If and when the Higgs boson is discovered, such measurements will help to over-constrain the parameters of the combined electroweak theory.

- Strong interactions: measurements of the strong coupling constant, α_S, and the parton density functions. The basic principles behind the strong nuclear force are well described by the gauge theory of QCD. However, experimental measurements of QCD parameters are crucial since non-perturbative interactions between particles make many calculations extremely difficult.

- Physics beyond the Standard Model: The aim is to find a better and simpler model of the universe. Many extensions to Standard Model have already been proposed. An example described above is the Minimal Supersymmetric Model (MSSM). The model suggests a symmetry between fermions and bosons i.e all fermions have a boson counterpart and vice versa. The theory predicts a whole spectrum of super-symmetric partners to the known particles. Non of these super-symmetric partners have yet been discovered. A promising experimental signature is the missing momentum carried away undetectable by the weakly interacting sparticles. For SUSY theories with Higgs mechanism, detection of several of the Higgs bosons should be possible for most viable combinations of parameters.

ATLAS will investigate the open issues presented above and many more not mentioned here. This means ATLAS has to be very versatile, to have a large potential for the discovery at the TeV energy scale of many new phenomena, both expected and unexpected.
This thesis describes my own contributions to one of the sub-detectors of the ATLAS experiment: the Semi-Conductor Tracker (SCT). Chapter 2 describes briefly the LHC, the ATLAS experiment and the SCT. Chapter 3 describes capacitance measurements on silicon micro-strip detectors and how capacitance contributes to noise in silicon micro-strip modules. Chapter 4 describes different methods to measure common mode noise in binary readout systems. Chapter 5 discusses the application of the common mode noise methods to ATLAS SCT end-cap modules. In chapter 6, different steps and software needed to perform the SCT simulation under the Athena framework are discussed. The effect of increased SCT noise and inefficiency on single track reconstruction efficiency of ATLAS Inner Detector is discussed in this chapter. The final chapter concludes with a summary of the main results of this work.

Chapter 2

The ATLAS experiment

Particle physicists believe that many of the fundamental questions left unanswered or even raised by high energy experiments so far could probably be answered at still higher energies. The upcoming accelerator facility, CERN's next big machine, the LHC due to start operating in 2007 and its related experiments are being designed to answer these questions and to look for theoretically predicted phenomena. However, they must also be prepared, as far as possible for unforseen phenomena. This task is a great challenge and requires great effort on the part of the physicists and engineers involved.

2.1 The Large Hadron Collider

The Large Hadron Collider (LHC) is currently under construction in the former LEP tunnel at the European particle physics laboratory (CERN) in Geneva, Switzerland. The machine will accelerate protons to energies of 7.0 TeV. Two beams of opposite orientation will be made to collide at four interaction points, each of which will be equipped with a large experimental apparatus: ATLAS, CMS, LHC-B and ALICE.
The LHC has the potential to greatly advance our understanding of fundamental physics, and to constrain the theories which can describe it. Its high energy and luminosity allow exploration of a variety of important questions, such as the origin of mass, the predominance of matter over ant-matter, and the relationship of matter to the forces that act on it. Some parameters of the LHC can be found in Table 2.1
In the LHC the collision of (heavy) protons allows to reach much higher ener-

Collision energy (p-p)	14 TeV (CM)
Collision energy (Pb-Pb)	3 TeV/nucleon
Maximal luminosity	$10^{34} cm^{-2} s^{-1}$
Collision rate	40 MHz
Circumference	27 km
Particles per bunch	10^{11}
Bunch length (σ_z)	7.5 cm
Bunch width (σ_x)	15.9 μm
Bunches per beam	2835
Beam current	0.53 A
Magnetic field strength	8.36 T
Commissioning year	2007

Table 2.1: Some design parameters of the LHC.

gies than electron-positron storage rings (such as the LEP collider, previously operated at CERN) as a much smaller fraction of the beam energy is lost due to synchrotron radiation. For the LHC the greatest design challenge, in terms of maximal collision energy, will be the maximum magnetic field achievable in the bending magnets. The design value of the field is 8.6 T.
The major problem in hadron colliders as compared to lepton colliders is that hadrons are not fundamental particles. As protons are compound objects, the hard collision does not involve the full momentum of the protons: the partons (quarks and gluons) that make up the proton each carry a fraction of the proton momentum. The momentum transfer occurs between for example two gluons or two quarks. Thus, even if the cross section for a proton-proton interaction is relatively large, the transferred momentum in the collisions span over a large range. Only a small fraction of the collisions will have sufficiently large momentum transfer to open interesting physics channels.
For the accelerator to be an effective probe into the new energy range, a large number of interesting events has to be accumulated. The LHC combines a bunch crossing frequency of 40 MHz with the highest luminosity achieved up to date. The accelerator is intended to ramp up from initial low luminosity $\mathcal{L} \sim 10^{33} s^{-1} cm^{-2}$ to the design luminosity of $\mathcal{L} = 10^{34} s^{-1} cm^{-2}$ in the first years.
The counter-rotating beams of protons will be made to collide at four points each surrounded by a detector as shown in Fig. 2.1. ATLAS and CMS are general purpose detectors, with wide-ranging physics programs. ALICE (A Large Ion Collider Experiment) [16] has been design to study the products of heavy ion collisions, while LHCb [17] is intended to measure the decay products of hadrons containing b-quarks. These decays are very important for the study of matter anti-matter asymmetry, more precisely CP-violation.

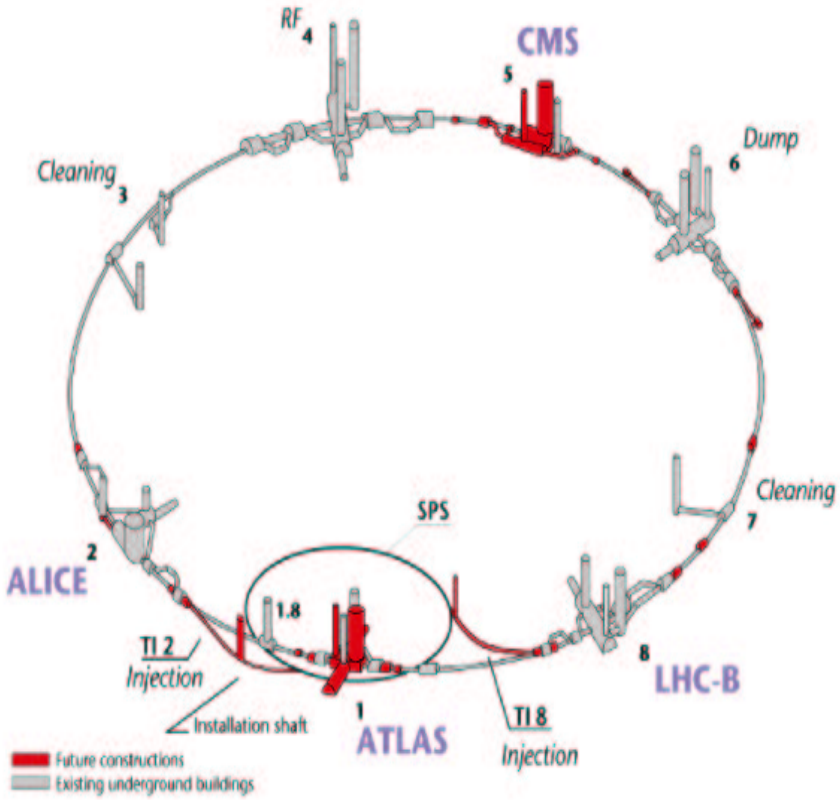

Figure 2.1: Layout of the LEP tunnel including future LHC infrastructure. Protons will be accelerated progressively in CERN's chain of accelerators, of which only the largest two (the SPS and the LHC) are shown.

2.2 The ATLAS Experiment

The ATLAS (A Toroidal LHC ApparatuS) experiment is a general purpose experiment designed to exploit the full discovery potential of the LHC from the startup of the machine.
A major focus in the design and optimization of the ATLAS detector has been the discovery potential of the mass generating Higgs boson(s). In addition, many expected physics processes and also a large variety of physics phenomena beyond the Standard Model, like SUSY searches, have played an important role in the detector optimization. The primary goal is a detector with the ability to cope with a broad range of important physics processes.
To meet the physics goals the ATLAS experiment has to measure all products of the collision that have a sufficiently long lifetime to be detected. Of all parti-

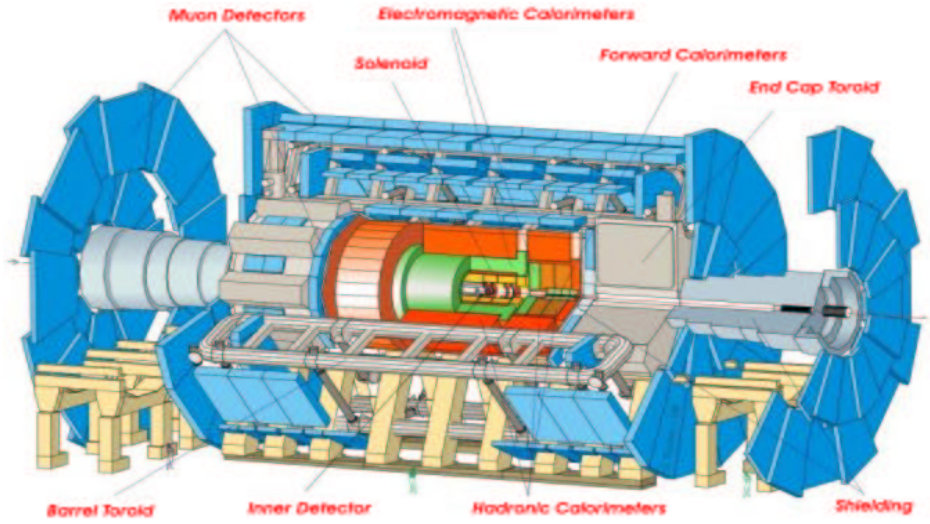

Figure 2.2: Overall layout of the ATLAS detector.

cles, the energy-momentum four-vector is to be determined with great precision. Where possible, the particle type should be determined with high efficiency. A three dimensional view of the overall layout of the ATLAS detector is shown in Fig. 2.2.

The detector has three distinct sub-systems which, in order of increasing distance from the beam pipe, are: an inner tracker, a calorimeter and a muon spectrometer. The Inner Tracker, also known as the **Inner Detector**, will provide precise tracking and vertexing of charged particles. The momentum of charged particles is determined from the curvature of the trajectory in the 2 T magnetic field generated by the solenoid magnet around the inner detector. The calorimetry system is situated between the inner detector and the muon spectrometer. Its purpose is to accurately measure the energy of all collision products. The first layer after the inner detector in Fig. 2.2 is the **electromagnetic calorimeter** [22]. It measures the energy of the shower produced by photons, electrons and positrons traversing dense material.

The showers produced by hadrons are contained in the **hadronic calorimeter** [23]. The calorimeters provide an energy measurement for jets of particles.

The **muon spectrometer** [24] forms the outer layer of the ATLAS experiment. The muon spectrometer is optimized for high-momentum final-state muons, which are among the most promising physics signatures at the LHC environment. Low transverse momentum muons are of major interest for b-physics and CP-violation studies. The overall length of ATLAS is 44 m and the diameter is 22 m, including the muon spectrometer.

ATLAS has three levels triggers in the event selection. The **Level 1 trigger** [25] makes use of a limited set of information from the muon spectrometer and the

calorimeters at 40 MHz bunch crossing rate. The Level 1 trigger must identify unambiguously the bunch crossing containing the interaction of interest and introduce only negligible dead-time. The target latency, i.e the time taken to form and distribute the trigger decision, consisting of particle time of flight, detector response, signal collection in the detectors, analogue signal processing, digitization, cable delay and digital processing, is ~ 2 μs with a 0.5 μs contingency. Awaiting the Level 1 decision, event data is stored in pipeline buffers locally in the sub-detectors. The acceptance rate from the Level 1 trigger is expected to be 100 kHz. For the **Level 2 trigger** [26] information from all sub-detectors is used, but only from certain regions of the detector acceptance. These regions of interest are defined by the Level 1 decision. The latency of the Level 2 trigger is variable depending on the event complexity, and varies within the range $\sim 1-10$ ms. The acceptance rate for the Level 2 trigger is about 1 kHz.
The **Event Filter** is the third and last level on the online event selection path of the ATLAS trigger system. Full event data from all sub-detectors at full granularity and precision is accessed by the event filter. The complete event reconstruction plus the subsequent decision will take up to ~ 1 s. The latency depends on the event complexity. The event rate at the output of the event filter is about 10-100 Hz. A combination of the event selection and data compression at this level will reduce the total data rate for permanent storage.

2.2.1 The Inner Detector

Reconstruction of tracks and (secondary) vertices are the tasks of the Inner Detector [20, 21]. Given the very large track density expected at LHC, high precision measurements on momentum and vertex resolution require fine-granularity detectors. The Inner Detector is contained within a cylinder parallel to the beam axis, centered at the interaction point. It covers the range $|\eta| < 2.5$[1], in accord with the other precision measurement systems in ATLAS. The Inner Detector is mechanically divided in a barrel and two identical forward units. A transition from the barrel layer geometry (parallel to the beam axis) to the forward (also called end-cap), disk geometry (perpendicular to the beam axis), is made starting at $|\eta| < 1$ in order to minimize the amount of material traversed by particles.

The Inner Detector consists of several layers of position sensitive detectors of three different technologies, as shown in Fig. 2.3. It combines high-resolution detectors at inner radii followed by continuous tracking elements at outer radii. The high precision tracking detector layers are in the barrel arranged on concentric cylinders around the beam axis, and in the forward directions mounted on disks

[1]The pseudorapidity η is defined as $\eta = -\ln(\tan(\frac{\theta}{2}))$

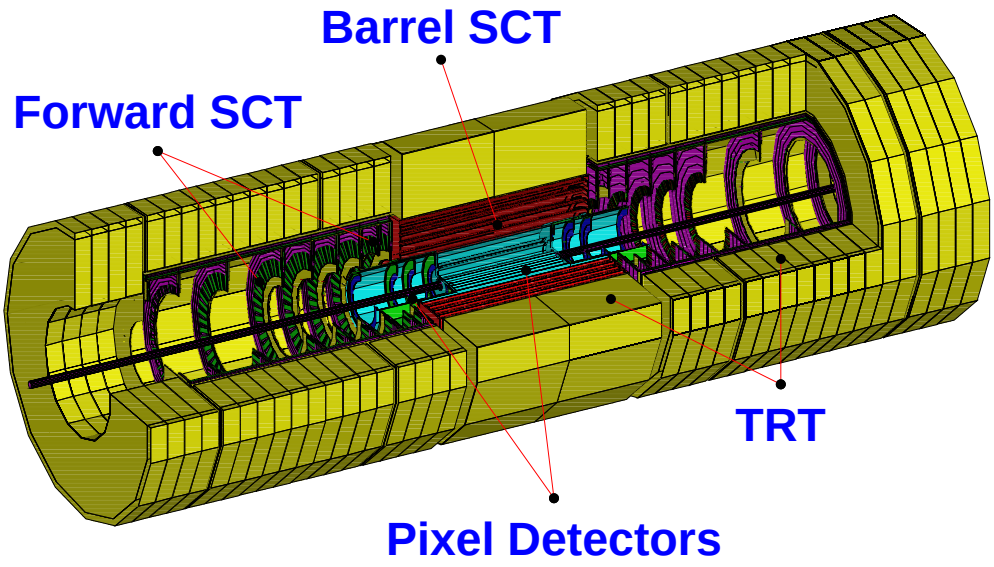

Figure 2.3: Overall layout of the ATLAS detector.

perpendicular to the beam axis. Some basic design parameters of the Inner Detector are given in Table. 2.2. The Inner Detector is made of the three sub-detectors described below.

2.2.2 The Pixel Detector

In the vicinity of the beam pipe (from 5 to 16 cm in radius) high precision, silicon substrate, Pixel detectors are used to achieve highest granularity (3 space points per track). The entire system consists of 2586 modules. Each module consists of 16 chips, with 160×24 pixels each. Each pixel is bump-bonded to a readout

System(read-out channels)	Position	η-coverage	Resolution (μm)
Pixel (140×10^6)	B-layer	± 2.5	$R\phi = 12, z = 66$
	barrel layers	± 1.7	$R\phi = 12, z = 66$
	end-cap discs	1.7 - 2.5	$R\phi = 12, R = 77$
SCT (6.2×10^6)	barrel layers	± 1.4	$R\phi = 16, z = 580$
	end-cap discs	1.4 - 2.5	$R\phi = 16, z = 580$
TRT (420×10^3)	barrel straws (axial)	± 0.7	$R\phi = 170$
	end-cap straws (radial)	0.7 - 2.5	$R\phi = 170$

Table 2.2: Table summarising the principal design parameters of the Inner Detector.

channel in the front-end chips that are mounted on the diode. The readout electronics amplifies and shapes the detector signal. The pixel readout is *binary*. A discriminator on the readout chip reduces the analog signal to one bit (hit/no hit) of digital information, thus limiting the amount of data from the $\sim$ 100 million channels.
The pixel size is 50×300 μm^2. The narrow side of the pixel is oriented in the $R\phi$ plane while the 300 μm side is oriented in z in the three barrel layers or in R in the three discs of each end-cap. Thus the pixel detector yields a good resolution($R\phi$ = 12 μm) in the bending plane of the solenoidal magnetic field, essential to the transverse momentum measurement. The resolution of the second coordinate in the three barrel layers is z = 66 μm and in the end-cap discs is R = 77 μm.
The innermost silicon layer of the pixel detector located at about 5 cm from the Interaction Point (IP), known as the B-layer, improves secondary vertex measurements considerably. The B-layer receives a particle flux five times higher than the next layer. It will have to be replaced every few years, due to damage by this high level of radiation.

2.2.3 The Semi-Conductor Tracker

The ATLAS Semi-Conductor Tracker is the silicon micro-strip tracker of the Inner Detector. It covers the region from 30 to 56 cm in radius from the beam axis. The Semi-Conductor Tracker (SCT) consists of a barrel system and two end-cap systems. The barrel detector consists of four barrel-shaped layers and each end-cap consists of nine disks as shown in Fig. 2.4. The cylindrical barrel covers the pseudo-rapidity range $|\eta| < 1.4$, whereas the end-caps extend the acceptance to $|\eta| < 2.5$. The inner radius of the SCT is 30 cm from the interaction point, the outermost layer is at 56 cm. The barrel extends to a distance along the

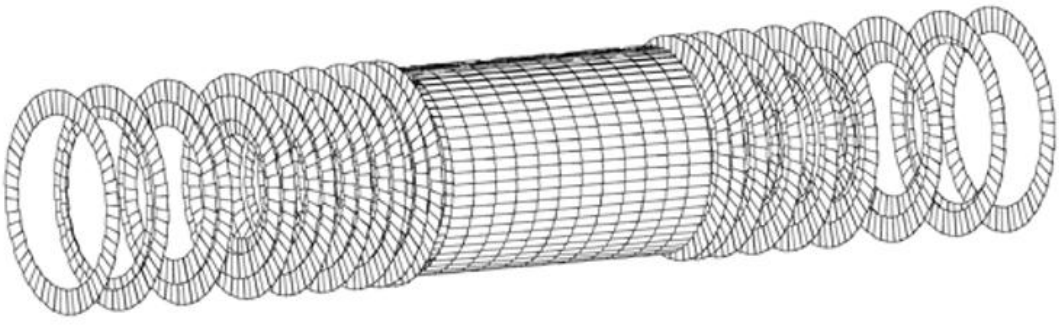

Figure 2.4: SCT layout showing only silicon sensors.

beam of 80 cm in both directions. Nine wheels with different inner radii provide measurements in the region from z = 80 to z = 270 cm. In this way the SCT provides four precision points per track in the intermediate radial range of the Inner Detector. Each precision point is provided by two back-to-back silicon strip sensors, which have a small stereo angle($\sim 2.3°$) with respect to each other. Each sensor has 768 strips with 80 μm pitch. Each SCT layer is expected to provide a spatial resolution of ~ 17 μm in the $R\phi$ plane in the barrel. The resolution of the second coordinate is of the order of 580 μm. The second coordinate is essential to resolve ambiguities in the pattern recognition, i.e to assign hits to tracks in the dense tracking environment.
Silicon micro-strip detectors, like pixel detectors, are based on a depleted diode. In this case however, the readout plane is segmented in narrow bands or strips. Thus, a single sided silicon micro-strip detector measures a single coordinate of the position of the track. As for the pixels, the SCT readout is binary.

2.2.4 The Transition Radiation Tracker

The Transition Radiation Tracker (TRT) uses straw detectors to improve momentum reconstruction, pattern recognition and electron identification (36 points per track). The straws have a diameter of 4 mm and a length between 39 cm and 150 cm depending upon their position in the detector. A thin wire extends through the centre of the straw and forms the detector anode. The conductive wall of the straw acts as the cathode. The straws are filled with a gas mixture of Xenon, Carbon Fluoride CF_4 and Carbon Dioxide CO_2 in the proportion 70:20:10. The Xenon content of the gas ensures efficient X-ray absorption. The addition of fast CF_4 minimises the pile-up of signals from consecutive bunch crossings. Ionising radiation traversing the straw produces free charge in the gas which drifts under the action of an applied electric bias and is collected at the anode.
The space between straws is filled with polypropylene/ployethylene fibres. Electrons traversing these fibres emit transition radiation (X-rays) which are detected in the straws tubes. The TRT will thus contribute to electron identification.
The straws are read out on both sides by a Transition Radiation Detector Analogue integrated circuit. After the amplification and shaping stages two thresholds are applied. The low-level threshold is used to detect the signal from ionisation. The Drift-Time Measuring Readout Chip uses the low-level signal to determine the drift time with a resolution of 3.125 ns. The drift time in the straw is used to determine the distance of the track to the anode wire. The high-level threshold is roughly a factor 30 higher and detects the absorption of transition radiation photons that produce larger signals.

2.3 The Silicon Strip Detector Module

The design of the detector modules for mounting on the barrel cylinder and on the end-cap disks are different in many aspects. The differences are due to different geometries required and to some deliberate design choices. There is a single module design for the SCT barrel region, and three designs for the various radial

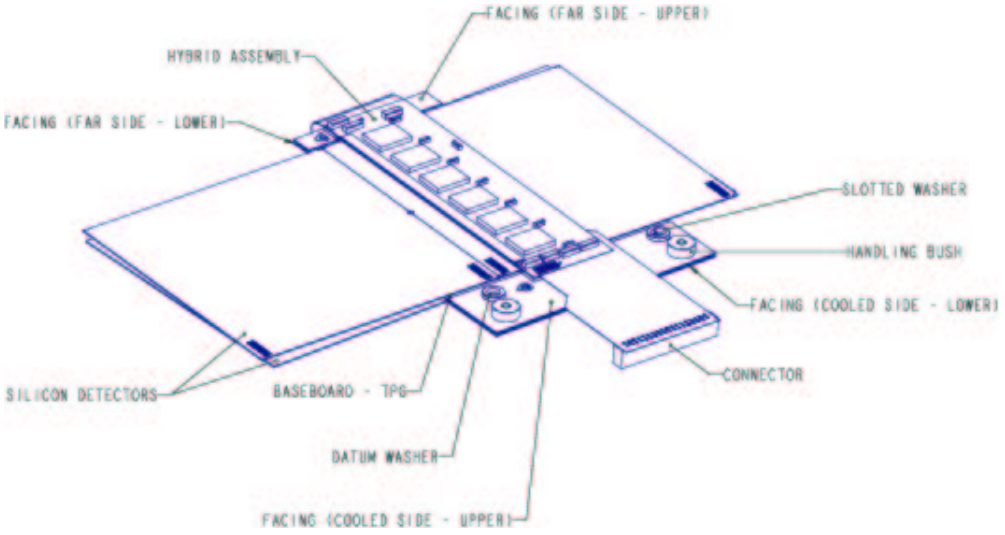

Figure 2.5: Drawing of a SCT barrel detector module.

locations in the SCT forward regions. The module design follows, however, the same concept. Fig. 2.5 shows a barrel module [27] and Fig. 2.6 shows an exploded view of an end-cap middle module [28].
Any SCT detector module has two distinct parts: the hybrid, a Cu/Polyimide flexible circuit laminated onto a carbon-carbon substrate, which is the support of readout ASICs[2], and the detector section. Both are thermally decoupled. The carbon-carbon used is unidirectional material with very good heat conduction and high Youngs modulus in the direction of the carbon fibres. The direction of the fibres is chosen to give a good thermal path from chips to the cooling interface. The barrel module has two single-sided hybrids bridged over the detector and the cooling contact is made at one side, as shown in Fig. 2.5. The end-cap module has one double sided hybrid placed at one end of the module.
The hybrid is connected to the detector section of an end-cap module by the 300 μm thick glass fan-ins which through wire bonds establish the electrical connection of the detector strips to the ASICs. This configuration implements a thermal split between the hybrid and the silicon sensors which largely avoids heating the

[2]Application Specific Integrated Circuits

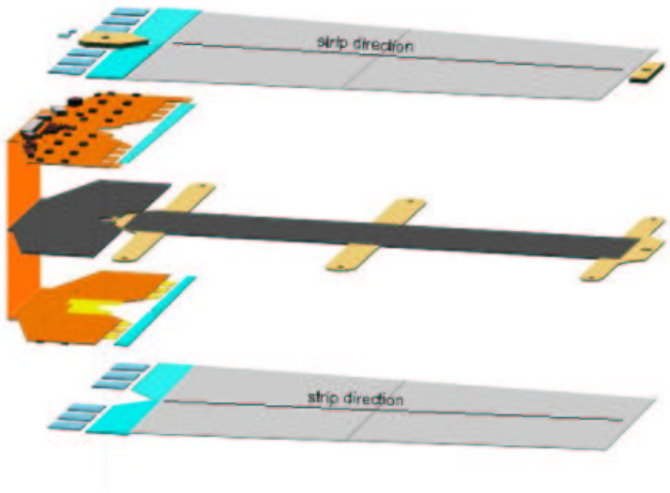

Figure 2.6: Exploded view of a middle end-cap detector module.

sensors by the power dissipation of the ASICs. The primary cooling contact is at this break, oriented along the module axis. Additional cooling is provided by a contact to the far end of the detector section.
In the detector section, for a **barrel detector module** two pairs of rectangular silicon sensors are glued either side of a spine or baseboard giving mechanical stability and providing a heat path from the sensors to the cooling block. The baseboard is made of a substrate of Very High Thermal Conductivity Pyrolytic Graphite (VHCPG) encapsulated in epoxy. The interface to the cooling block consists of Beryllium Oxide (BeO) facings laminated to the baseboard. The strips in each pair are daisy-chained to form approximately 12 cm long strips. The active strip length is constrained by the capacitive load of the readout ASICs and by the occupancy at high luminosities. The strips on opposite sides are rotated by a stereo angle of 40 mrad ($\sim 2.3°$) that will provide z measurement capability. The choice of a small stereo angle has been dictated by a compromise between the resolution on z, and therefore on vertex/mass reconstruction, and the need to reduce the number of ghost hits near a real track in high multiplicity events.
A binary architecture has been chosen for the readout of the sensors, which dictates the readout of individual strips, rather than charge division. The required tracking precision in $R\phi$ in the barrel is therefore obtained by an 80 μm pitch, giving an intrinsic point resolution of $\sigma_{strip} = \frac{80}{\sqrt{12}} = 23$ μm and a space point resolution of $\sigma_x = \frac{\sigma_{strip}}{\sin(40mrad)} = 580$ μm and $\sigma_y = \frac{\sigma_{strip}}{\sqrt{2}} = 16$ μm. In the barrel region, the modules are mounted at an angle of about 10° to the tangent, depending on

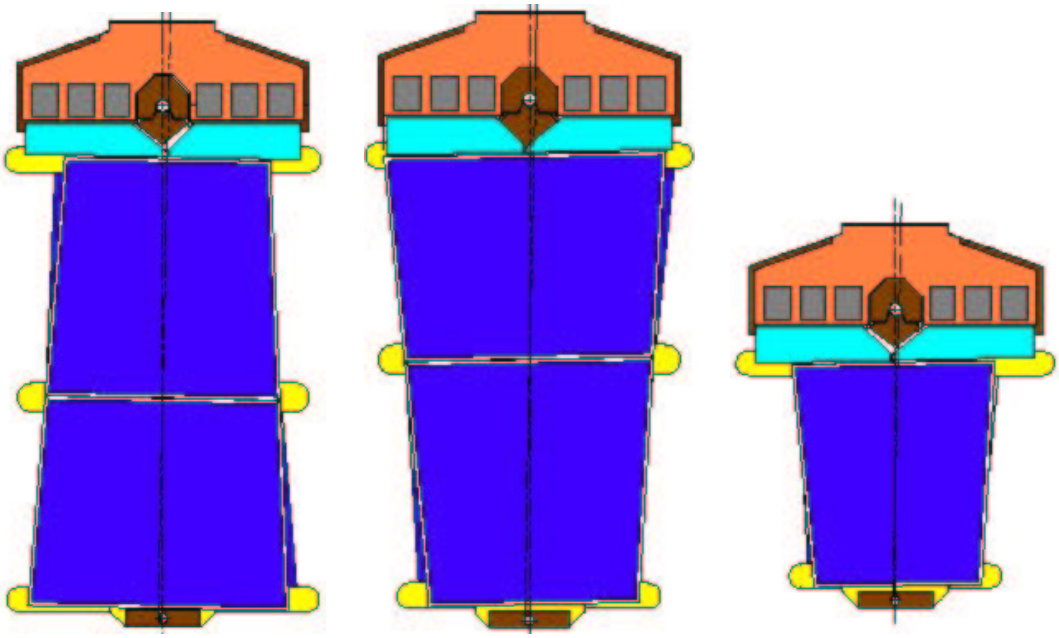

Figure 2.7: The three types of ATLAS SCT end-cap modules. These are the outer, middle and inner module (from left to right).

the layer, to minimise the signal spread during operation in the solenoid field.
The **end-cap detector modules** are mounted on disks in the plane orthogonal to the z-axis with the strips on one side of the modules in the radial direction. The strip pitch varies (from about 50 and 90 μm) along the length of the sensors so the strip implants are pointing in the R direction across the whole detector module. The three types of end-cap detector modules are shown in Fig. 2.7. The modules depending on their position on the disks are: inner, middle and outer detector modules. The layout of the silicon sensors of the three types are adapted to their respective radial position.
The middle and outer modules carry two pairs of wedge shaped silicon micro-strip sensors in a back-to-back configuration. The strips in each pair are daisy-chained like in a barrel module to form 12 cm long strips. Inner modules have just one sensor on each side and about 6 cm strip length.
The silicon sensors are mounted on a spine providing mechanical stability and a thermal path between the detectors and the cooling block. The spine is made of Thermal Pyrolytic Graphite (TPG) coated with a 10 μm layer of Parylene-C for mechanical protection and electrical insulation. The TPG has an extremely high thermal conductivity of about 1700 W/mK in the plane, runs over the cooling blocks and provides the required cooling of the silicon.
The 12 ASICs on a module dissipate a power of 4.75 W for nominal operation and a maximum of up to 7.0 W. After irradiation the silicon sensors show a sig-

nificant amount of self-heating due to the increased leakage current and operating voltage. Cooling the silicon to a target temperature of $-7°C$ limits the leakage current such that it hardly affects the electronics noise and also eliminates the risk of thermal runaway. Furthermore, it avoids reverse annealing of the radiation induced change to the effective doping of the silicon. In the following subsections some of the components of a module will be described briefly.

2.3.1 Silicon Microstrip Detectors

There are several advantages of using silicon as a detection medium for charged particles [29]:

- The high mobility of the charge carriers enables fast charge collection times (approximately 5 ns for electrons).
- The high density of silicon in combination with the relatively low energy needed to create an electron-hole pair (3.6 eV, compared to the 30 eV needed for single ionisation in a gaseous medium).

The single sided silicon sensors with 768 AC-coupled p-type readout strips implanted in n-type silicon of 285 ± 15 μm thickness have been chosen as the technology for the SCT. The resistivity of the substrate is specified to be between 3 and 8 kΩ.cm. The geometrical constraints on detectors for the barrel and end-cap regions are very different: whereas in the barrel region the detectors are arranged parallel to the beam axis, in the end-caps the modules are placed on wheels perpendicular to the beam axis. Therefore different sensors have been designed. The barrel region uses rectangular shaped sensors with parallel strips and for the end-caps modules five flavors of wedge-shaped detectors are used. Apart from these geometrical considerations the detectors have very similar properties.
The detectors are designed to operate reliably at high bias voltages (up to 500 V). Guard rings are used to step down the voltage towards the edge of the detector as shown in Fig. 2.8.
In the SCT detectors the coupling capacitor is integrated in the detector design. This is achieved by implementing an insulating silicon oxide layer between the strip implants and the surface strip metallisations. The capacitance to the back plane and neighbouring strips, are drawn in Fig. 2.8. These make up the load capacitance on the amplifier and are the main determining factor in the noise performance. Moreover the coupling between the neighbouring strips leads to signal loss in the binary readout scheme. Measurements of inter-strip and back plane capacitances, its contribution to the equivalent noise charge and signal loss due to coupling will be discussed in detail in chapter 3. In order to keep the strip

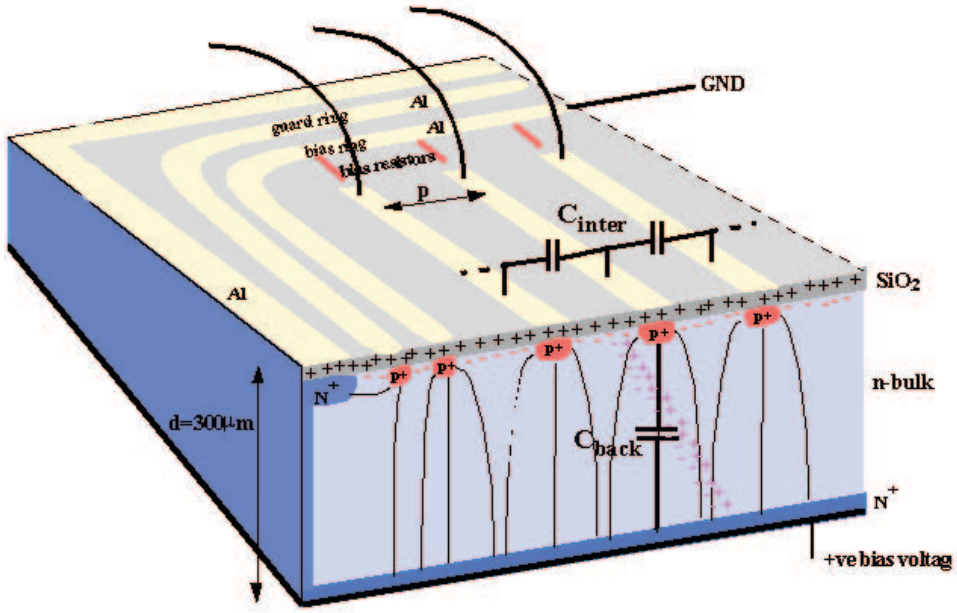

Figure 2.8: Schematic of a silicon strip-sensor.

implants at a defined potential (ground in this case), they are connected to a common ground rail which surrounds all strips on a wafer through a poly-silicon or implanted bias resistor. The implementation of a large resistance, 1.25 ± 0.75 MΩ, ensures that the contribution to the noise related to the bias resistance is negligible.

The metal strips present a resistance that leads to an additional noise contribution. With the specified aluminium strip resistance for the SCT detectors of less than 15 Ω/cm this contribution is small.

The electrical integrity of all detectors delivered to the SCT is tested extensively. Two specifications are set: the current measured at a temperature of 20°C has to be below 6 μA when the detector is biased to 150 V and below 20 μA at a bias voltage of 350 V. Incase the current at one of these voltages exceeds the specification or a breakdown is observed below 350 V the detector is not accepted.

The effect of radiation on the electrical performance of SCT detectors has been studied extensively. For the wafers to be used in the SCT, type inversion is found to occur after around 0.5×10^{14} NIEL[3] equivalent 1 MeV neutrons/cm^2. Due to the type inversion, the detector junction moves to the back side of the sensor. High bias voltage will be needed to ensure full depletion so that charge is efficiently

[3]Non-Ionising Energy Loss arises from elastic or inelastic interactions with the silicon nucleons in the lattice

collected. After a fluence of 3×10^{14} protons/cm^2 the depletion voltage is found to be of the order of 200-300 V. Irradiated detectors will anneal at temperature above 0°C [30, 31]. Although on the time scale of days the annealing reduces the depletion voltage with time, at much longer time it starts increasing. The leakage current can be reduced and reverse annealing effects can be suppressed by operating the detectors below 0°C. Due to this reason the SCT will be maintained at a temperature of −7°C.

2.3.2 Readout ASICs

The silicon sensors of a module are readout by twelve front-end ASICs, named ABCD3TA [32, 33, 34], which are fabricated in the radiation tolerant DMILL [35] process. A block diagram of the ABCD3T chip is shown in Fig. 2.9.
The strong point of the DMILL technology is the possibility to integrate fast, low-noise analog circuits and digital functions in a single chip. The analog functionality required for the front-end can be implemented in bipolar devices, while the digital part can profit from fast CMOS devices. The implementation of ASICs in DMILL is described in [36].
Each of the 128 channels in a ABCD3T chip contains an analogue front-end, an input register for masking of failing channels, a digital pipeline which stores the data for about 3 μs until a first level trigger decision is taken, data reduction and readout buffers. The analogue functionality of the ABCD3T includes pulse shaping with a time constant of about 25 ns, amplification and a comparator with a threshold which is adjustable for each individual channel.
The noise performance of the amplification stage is very important for the overall performance of the detector. There are many noise sources contributing to the total noise at the amplifier. For details see [37, 38, 39]. One can divide the noise sources in two main parts. The first kind of sources are the series noise sources, like thermal noise in the input channel of the preamplifier, flicker noise(1/f-noise), noise from series resistors on the detector or from resistors between detector and amplifier. The second type of sources are the so-called parallel noise sources, like noise due to the detector leakage current, noise due to the feedback resistor, and noise due to the bias resistor of the detector. For a front-end system based on *npn* bipolar transistors the equivalent noise charge due to thermal noise is proportional to the load capacitance C_{load} and will be discussed in detail in chapter 3.
The shot noise contribution is independent of the load capacitance and is given by,

$$ENC = \frac{e^3}{36q_e}\left\{\frac{5T_p}{3}\left(\frac{2q_eI_c}{\beta} + \frac{4kT_c}{R_f} + 2q_eI_l + \frac{4kT_s}{R_b}\right)\right\}^{\frac{1}{2}} \tag{2.1}$$

Where I_l is the detector leakage current, β is the DC current gain of the input transistor, I_c is the collector current, T_c and T_s are the chip and sensor tempera-

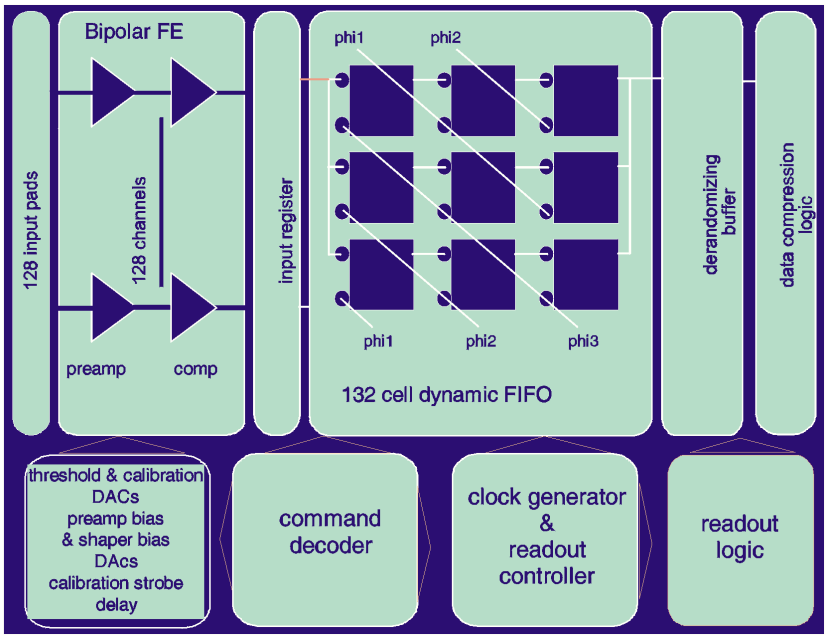

Figure 2.9: Block diagram of the ABCD3T front-end ASIC.

tures, T_p is the peaking time of the shaper, R_f and R_b are the feedback and bias resistors. Due to the short peaking time of the ABCD3T shaper/amplifier shot noise due to the detector leakage current is not significant for leakage currents up to 2-3 mA.
In the binary readout scheme the pulse obtained by amplification and shaping of the signal is reduced to one bit of digital information on the chip by comparing with a preset threshold. The discrimination threshold is set in the chip configuration register and is the same for all 128 channels. Small non-uniformities in the response of the amplifiers across the channels are corrected by adjusting the 4 bit trimDAC of each channel. The range of all trimDACs on a chip is chosen by setting two bits in the configuration register. Thus, fine matching can be obtained before irradiation, while no channels drift out of the trimmable range after the irradiation.
Due to the binary readout scheme the data is reduced to the bare hit information (for each channel only one bit information remains) already at the front-end which simplifies the data transmission and processing, but is also very demanding on the system performance since any common mode noise has to be kept at negligible levels. The measurement of common mode noise using the binary readout will be discussed in chapter 4 and 5.
An integrated calibration circuit allows a fast and accurate characterisation of the analog stages of the chip channels. A digital to Analog Converter (DAC) and a chopper circuit generate a voltage step of settable height. This voltage step is

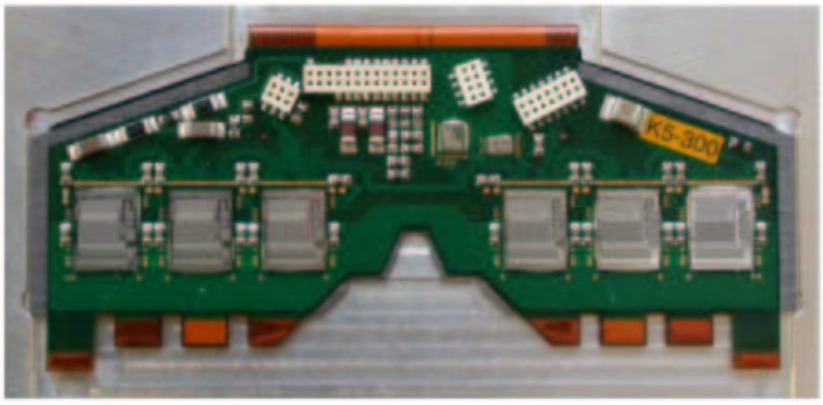

Figure 2.10: A picture of a fully populated forward hybrid, laminated onto the carbon-carbon substrate.

applied to a 100 fF calibration capacitor, thus creating a fast charge pulse that is injected into the input of the preamplifier. By scanning the threshold voltage and registering the binary response, the S-curve can be reconstructed, where the S-curve is the plot of number of hits as a function of threshold. The S-curve for a fixed charge and Gaussian noise is described by a complementary error function. The threshold where 50 % efficiency is obtained, is the threshold corresponding to that input charge. The width of the S-curve is a measure of the output noise. The relation between input charge and threshold voltage is known as the response curve. It is determined repeating the threshold scans as described above for a number of input charges in the range of interest (0.5-10 fC). The gain of the analog stage of the chip is obtained as the derivative of the response curve. Typical values are in the range 50-60 mV/fC. The equivalent noise charge at the input of the amplifier (in fC) is obtained by dividing the output noise (measured in units of threshold voltage, mV) by the gain (in mV/fC). The input noise value shows a slight dependence on input charge due to the non-linearity of the response curve at high charges and of the calibration circuit at low charges.

2.3.3 Hybrids

The readout ASICs are mounted on a Cu/polyimide, multilayered, flexible circuit laminated onto a carbon-carbon substrate. The same technology is used both in barrel and end-cap modules.
The hybrid plays a major role in the electrical readout as well as in the mechanical support and cooling. It must have sufficient thermal conductivity to allow most of the heat generated by the front-end chips to be removed by the coolant and must support the front-end ASICs sufficiently to allow reliable wire bonding to the detectors. The circuitry in the hybrid distributes and filters the power, provides

ground, clock and control lines to the ASICs, supplies and filters the bias voltage to the detectors, returns the data to the optical links and supports the redundancy mechanisms of the ASICs. Here is described briefly only the forward hybrid, the most relevant to this thesis. The forward hybrid [40] is a double sided device carrying six readout ASICs on each side. It is composed of a six layer flexible circuit board with copper traces between polymide layers, folded around a carbon-carbon substrate as shown in Fig. 2.10. Layers 3 to 6 of the hybrid are reserved for the distribution of power, while signal lines run in layers 1 and 2. In the wrap around region only two metal layers run from the hybrid front to back side to facilitate the bending of the flex. Typical feature sizes are 75 μm and there are about 3000 microvias establishing connections between different layers. The hybrid supplies a bias voltage of up to 500 V to the silicon sensors. The hybrid carries two more ASICs called DORIC and VDC which in conjunction with the opto package are receiver and transmitter for the optical link. The heat generated by the ASICs is removed by the highly heat conducting carbon-carbon substrate into the central cooling block. Ceramic thermal plugs under each ASIC establish direct thermal contact between the ASIC and the substrate. The temperature of the hybrid is measured by a thermistor located on top of the hybrid.

Chapter 3

Capacitance Measurements and Detector Noise

The capacitance is a sensitive parameter in the operation of a silicon detector, as it directly affects the noise and cross talk. In order to understand its effects, it is essential to have a proper method for the capacitance measurements. Capacitance measurements have been made on a silicon miniature detector using different techniques and are discussed in the first part of this chapter. From these measurements it is concluded that the best mode for the capacitance measurement is the parallel mode.
In the second part of the chapter the detector noise is discussed. The ATLAS SCT specifications for efficiency and noise occupancy are 99% and 5×10^{-4} respectively, as given in the Inner Detector TDR [20]. For an equivalent noise charge of about 1900e, the noise occupancy reaches the SCT specification of 5×10^{-4} at 1 fC threshold.
In the real detector, if the noise occupancy grows, then more hits that are not associated to any track will be found which will increase the fake track rate. Also, reading out more data can cause inefficiencies in the read-out chain. The noise can be reduced by raising the threshold to maintain as clean a signal as possible. However, at some point the rising threshold will begin to remove the low pulse height signals from genuine particles and therefore will affect the efficiency. The effect of noise on the module charge collection efficiency is therefore discussed in this chapter, noise effects on the reconstruction efficiency will be discussed in Chapter 6.
The ATLAS SCT specifications for efficiency and noise occupancy are achieved over a range of threshold values. In order to calculate the width of this window for various signal to noise ratios, the effect of the threshold setting on noise occupancy and efficiency will be studied.
The next section describes the capacitance measurements made on a miniature

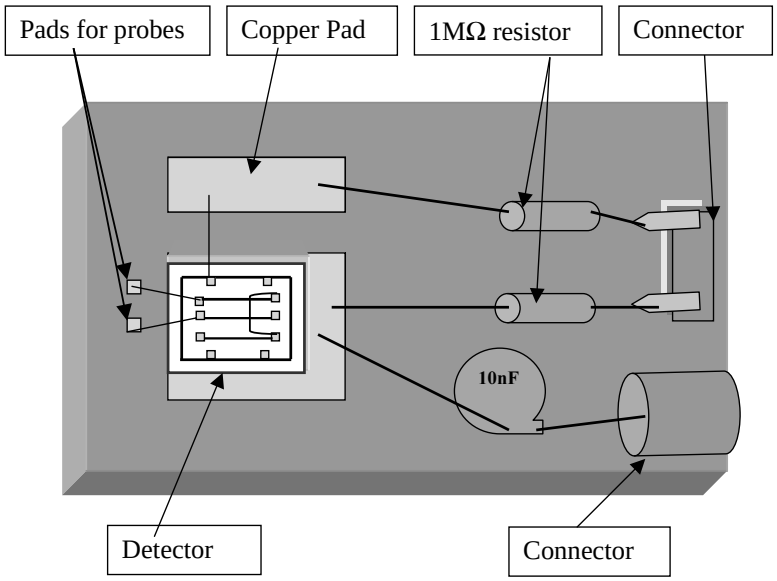

Figure 3.1: Schematic view of the setup for capacitance measurement

detector.

3.1 Capacitance measurements

The measurements are made on a miniature detector of 1 cm^2 area, 300 μm thick, with 98 strips and 8 mm strip length. All Al strips of the miniature detector are bonded together except the central one. The detector is glued using a conductive glue onto a copper pad on a PCB. For biasing purposes the guard ring pad is bonded to the nearby copper pad on the PCB. The schematic is shown in the Fig. 3.1. The central Al-strip is bonded to a copper pad on one side and similarly all the remaining Al-strips are bonded to a second pad. The purpose of using these two pads instead of directly using the detector pads is to prevent damaging the detector during repeated measurements. The detector is biased with the backside at positive high voltage and the guard ring at GND of the power supply. The probe station is shown in Fig. 3.2. On the left there is a Karl Suss PA200 semi automatic probe station enclosed in a dark box with microscope and color camera. On the right from top to bottom are a switching board, a Keithley 2001 (multimeter), a Keithley 237 (High voltage source measurement unit), a Hewlett-Packard 4284A (LCR meter), and a PC with Lab View [41] and control software. There is a control box in front of the PC from which the probe station can be controlled. The LCR meter is corrected for OPEN (means that needles are free in the air) and SHORT (means that two needles touch each other) in series mode and the series capacitance is measured. In this way the total calculated (interstrip

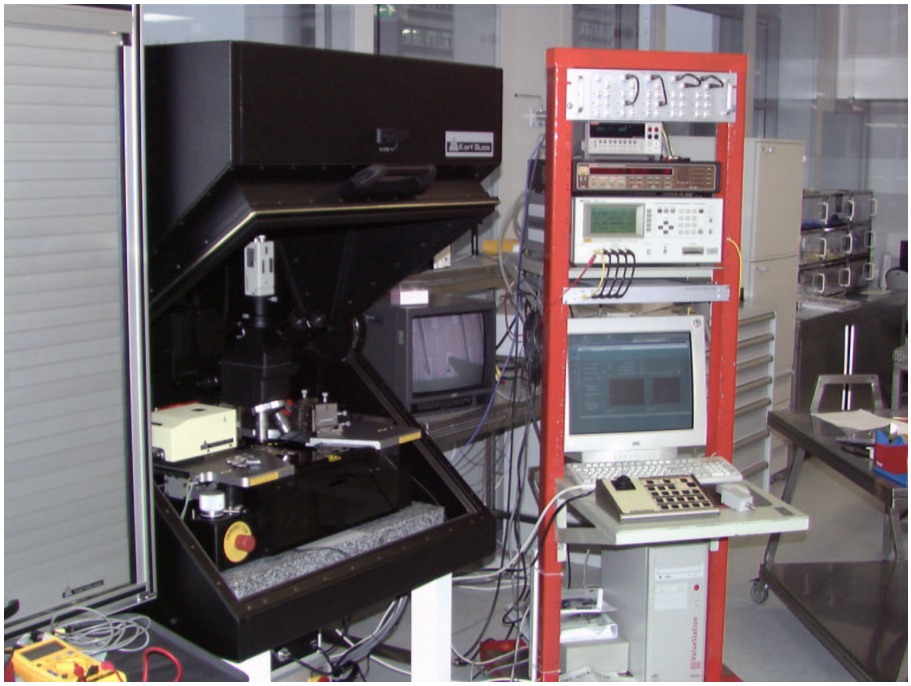

Figure 3.2: Photo of the Probe Station

capacitance + backplane per strip capacitance) and total measured capacitances were quite different. We performed those first measurements at 1 V voltage level of the LCR meter in series mode. Standard ceramic capacitors are measured using the LCR meter test fixture and then directly using the probes. A correction table is made that contains the ratio of fixture to probe capacitance measurements. It is found that in our measurement capacitance range there is 15% uncertainty in the test setup that comes from the cables and probes. We made the following changes in our final measurements.

- Two resistors (each 1 MΩ) are soldered on the module into the high and low lines in order to decouple the HV power supply and supply lines from the measurements and to protect the detector.
- Incase of interstrip capacitance measurement the backplane is locally grounded with the LCR meter ground via a 10 nF capacitor. Local grounding was better than on the switching board. There was no difference between the grounding with the LCR meter ground or with the shielding of the connecting wire.
- Open and Short corrections as well as measurements are made in parallel mode (this point is discussed in section 3.1.2).

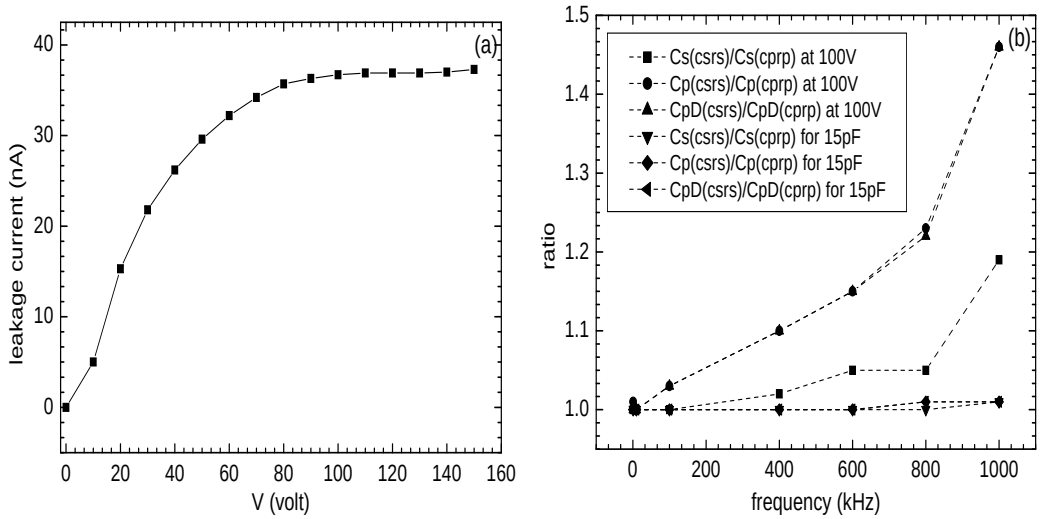

Figure 3.3: (a) Leakage current as a function of the reverse bias voltage measured on a detector of a surface area of 1 cm^2. (b) In the legend C_s and C_p stands for the series and parallel capacitance measured. In parenthesis C_sR_s and C_pR_p means that Open and Short corrections are made in series mode and in parallel mode, respectively.

- The measurements are made at 100 mV voltage level of the LCR meter.

Making all the above-mentioned changes the detector is biased and the IV-curve is taken up to 150 V as shown in Fig. 3.3 (a). All the measurements were made up to a bias voltage of at most 150 V.

3.1.1 Mode-dependence

At first we used the series mode for the measurements of capacitance and resistance but due to the difference found in measured and calculated total capacitance, we investigated in detail the mode-dependence. For this purpose, Open and Short corrections are made in series mode (discussed in the next section) and the inter-strip capacitance of the baby detector is then measured at 100 V first in series mode and then in parallel mode (discussed in the next section). Similarly the Open and Short corrections are made in parallel mode and the inter-strip capacitance is measured in series as well as in parallel mode. The same measurements are made for a 15 pF ceramic capacitor. The measurements for the detector and ceramic capacitor are plotted in Fig. 3.3 (b). The upper three curves show the inter-strip capacitance ratios at 100 V bias voltage when the open and short corrections are made in different modes and measurements are made in the same mode. The ratio is not 1 which indicates that data in different correcting modes are different. The lower three curves are for the ceramic capacitor of 15 pF. The ratio is 1

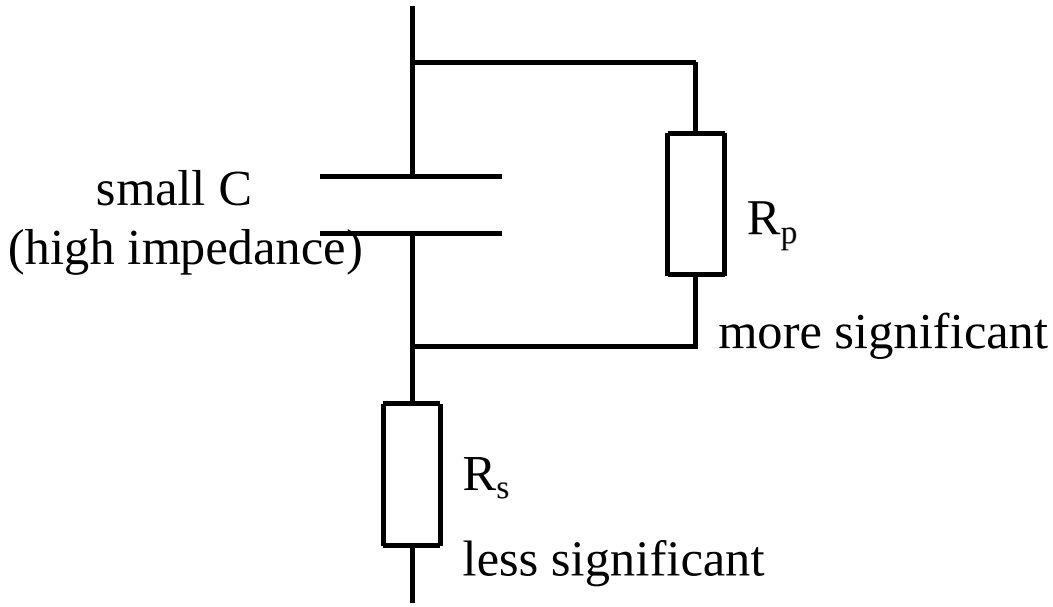

Figure 3.4: Capacitance circuit mode selection.

which shows that these measurements are mode-independent. This indicates that the detector is not a simple capacitor but a complex network of capacitors and resistors, in parallel as well as in series.

3.1.2 Mode Selection

To measure C and R there are two equivalent circuit models, the parallel and series modes. In each of these modes we can correct the LCR meter for Open and Short corrections and also can perform measurements. The circuit diagram is shown in Fig. 3.4. In case of small capacitance the reactance is large, which implies that the effect of the parallel resistance R_p has relatively more significance than that of series resistance R_s. The low value of series resistance represented by R_s has negligible significance compared with capacitive reactance and therefore the parallel mode should be used. In case of large capacitance the converse is true. For the parallel mode measurement we calculated $\frac{1}{\omega C}$ and compared it with the R_p measured directly with the LCR meter. The comparison of the $\frac{1}{\omega C}$ and R_p is shown in Fig. 3.5. Both X and Y-axis are on log scale. The plot shows that $\frac{1}{\omega C}$ is higher than the measured R_p in our working frequency range, therefore R_p is significant and we need to use parallel mode. The final measurements are performed in parallel mode, first making open and short corrections in this mode. These measurements are described in the following sections.

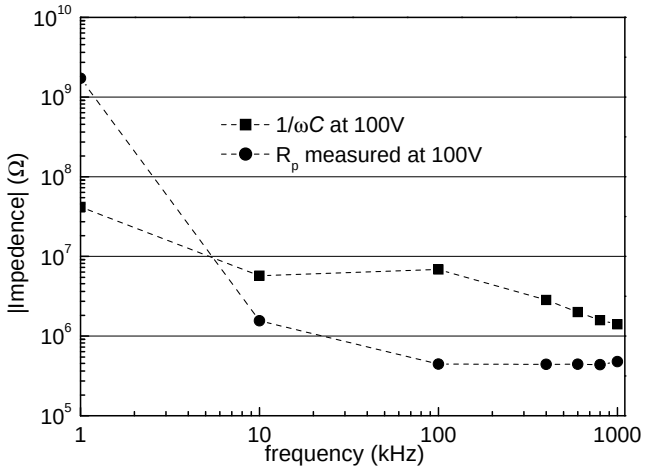

Figure 3.5: Comparison of $\frac{1}{\omega C}$ and measured R_p.

3.1.3 Backplane Capacitance

To measure the backplane capacitance Probe-1 is connected with the central strip and Probe-2 with all other strips. The two probes are then connected with the LDut(in) of the LCR meter. The backplane is connected to the Hdut(out) of LCR meter via Probe-3 with 10 nF capacitor. In this way the capacitance between all strips and the backplane is measured. To obtain the backplane capacitance for a single strip this data is divided by the total number (98) of strips of the

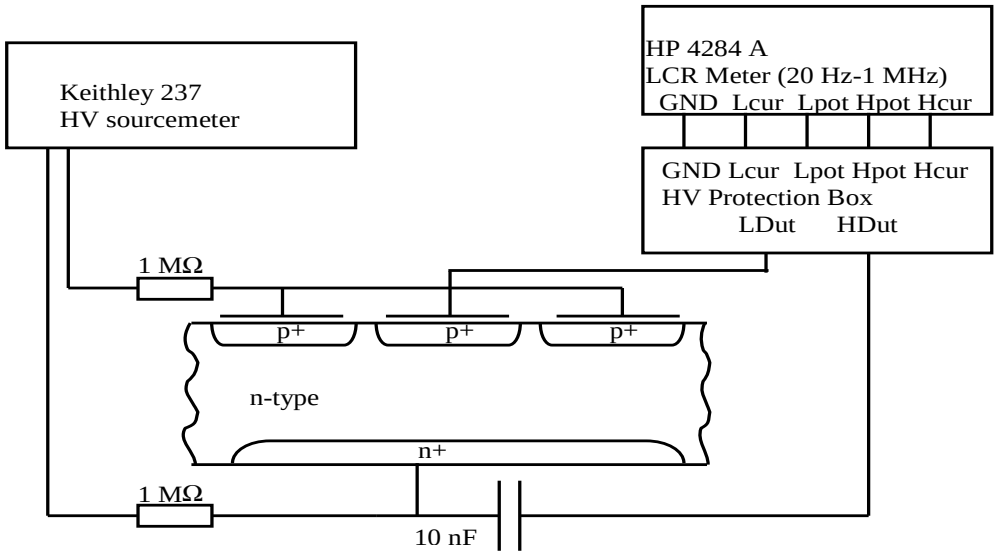

Figure 3.6: An overview of the set-up used to measure the strip to backplane capacitance of a miniature detector.

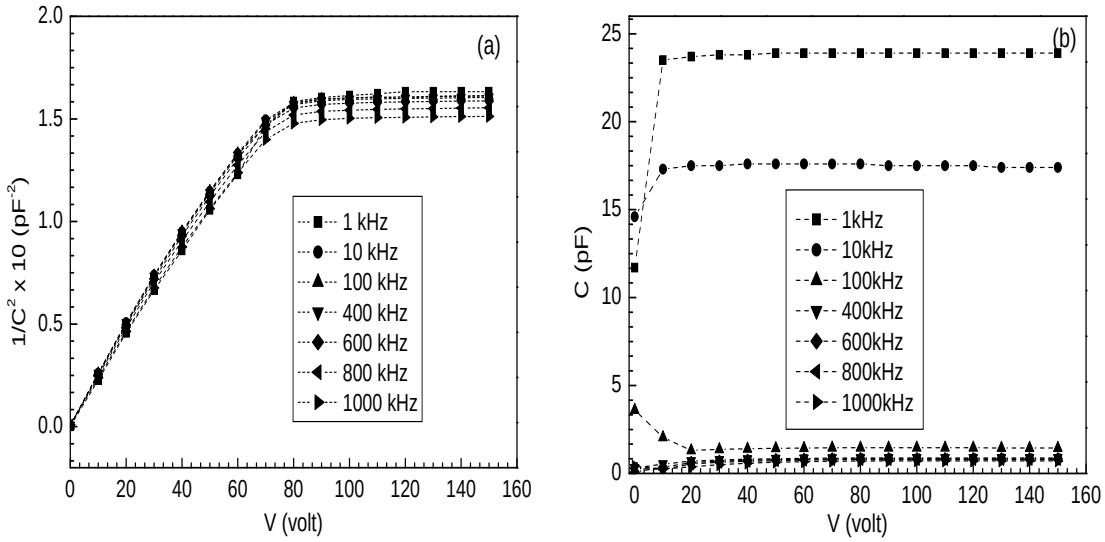

Figure 3.7: (a) $1/C^2$ versus V for the backplane at different frequencies in parallel mode. (b) Inter-strip capacitance as a function of bias voltage at various frequencies in parallel mode.

miniature detector. In this way the data is taken at various frequencies varying the bias voltage from 0 to 150 V. The $1/C^2$ as a function of voltage V is plotted in Fig. 3.7 (a). The depletion voltage can be studied from the above curves. All the curves become flat at around 80 V which indicates the depletion voltage.

3.1.4 Interstrip Measurements

Interstrip capacitance here means the capacitance of the central to all other strips. For this purpose the probe-1 is connected to the central strip, while probe-2 is connected to all other strips via copper pads. The backplane is grounded through a 10 nF capacitor to the LCR meter ground in order to get rid of the contribution due to the backplane capacitance. The probe-1 is then connected to HDut(Out) and Probe-2 to the LDut(In).
The interstrip capacitance is measured at various frequencies from 1 kHz to 1 MHz and biasing the detector up to 150 V. The capacitance as a function of biasing voltage is shown in Fig. 3.7 (b).

3.1.5 Total measured Capacitance

For this purpose three needles are used. Probe-1 is connected with the central strip via the copper pad. Probe-2 is connected to all the remaining strips via the

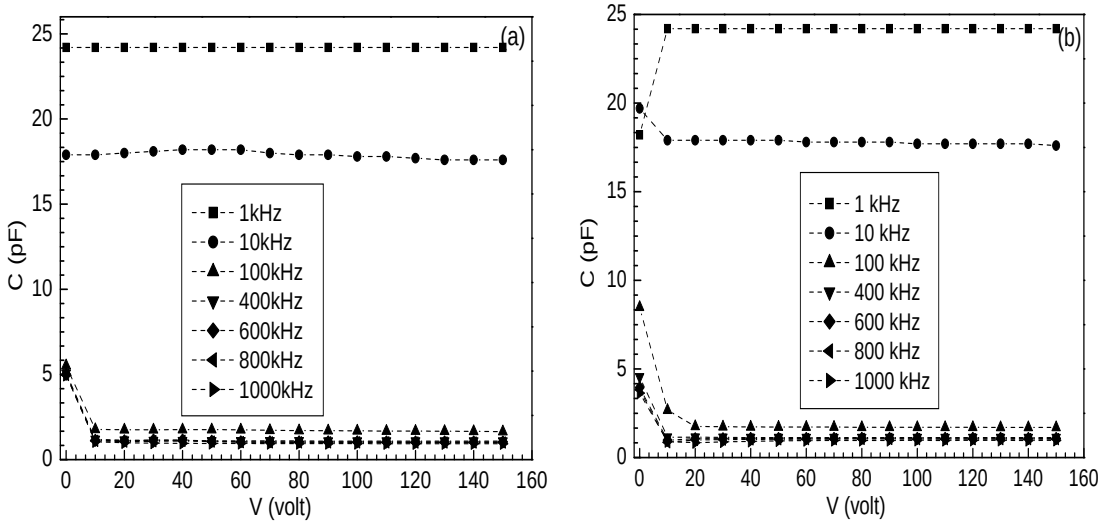

Figure 3.8: (a) Variation of total measured capacitance with the biasing voltage for different frequencies in parallel mode. (b) Total calculated capacitance (defined as the sum of inter-strip and backplane capacitance) per strip in parallel mode.

copper pad. Probe-3 is connected to backplane via a 10nF capacitor. Probe-2 and Probe-3 both are connected to the Hdut (Out) of the HV protection-box and Probe-1 to Ldut (In) of the HV protection-box.
In this way the total capacitance (which is the capacitance of the central strip to all other strips and to the backplane) is measured at various frequencies by varying the bias voltage from 0 V to 150 V. The plot for the total measured capacitance as a function of bias voltage at different frequencies is shown in Fig. 3.8 (a).

3.1.6 Calculated total capacitance

There are two ways to obtain the total capacitance. One way is to measure the total capacitance directly from the LCR meter as described above. A second way is to calculate it by adding the interstrip capacitance to the backplane capacitance per strip. In this chapter the first is called total measured capacitance and second referred to as the total calculated capacitance. The calculated capacitance as a function of biasing voltage at different frequencies is shown in Fig. 3.8 (b).

3.2 Comparison of calculated and measured total capacitance

The ratio for the total measured and total calculated capacitance for various frequencies is plotted in Fig. 3.9 (a). For comparison the ratio of the total measured

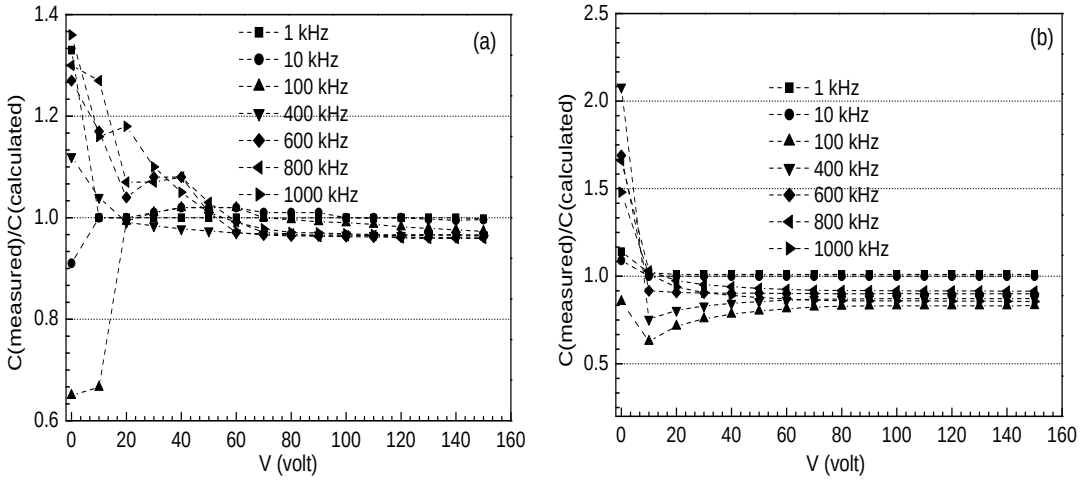

Figure 3.9: (a) Total measured to total calculated capacitance ratio for different frequencies in parallel mode. (b) Total measured to total calculated ratio for different frequencies in series mode.

capacitance to total calculated one when corrections are made in series mode is plotted in Fig. 3.9 (b). The ratio C_m/C_c vs frequency at 100 V in parallel mode is plotted in Fig. 3.10 (a). This plot shows that there is a 4% deviation between the measured and calculated capacitances at 100 V. The same plot at 100 V in series mode is given in Fig. 3.10 (b). The difference between the series and parallel mode measurements is clear by comparing the above plots. There is up to 17% deviation between the total measured and total calculated capacitance measurements

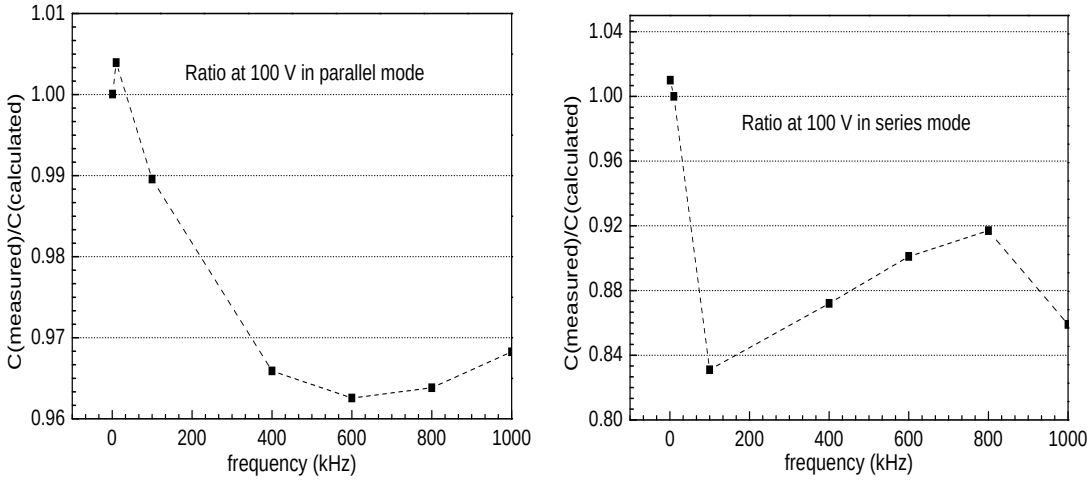

Figure 3.10: (a) Total measured to total calculated ratio versus frequency at 100 V in parallel mode. (b) Total measured to total calculated ratio versus frequency at 100 V in series mode.

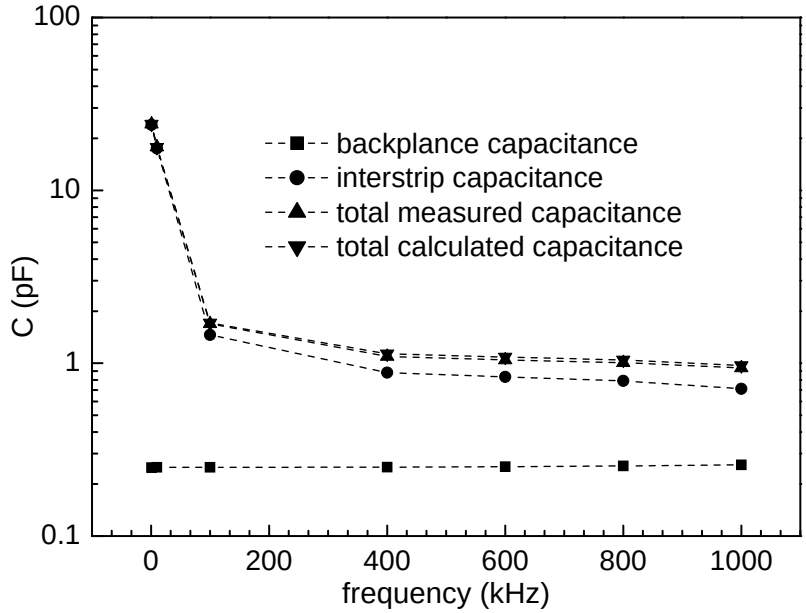

Figure 3.11: Capacitance versus frequency at 100 V for backplane, inter-strip, total measured and total calculated capacitance.

at 100 V in series mode. A comparison between different measurements is made by plotting them in the same plot as shown in Fig. 3.11. It should be noted that there is around 15% uncertainty in the above mentioned measurements, which comes from the measurement setup. A summary of the capacitance measurements at 100 V bias voltage and frequency of 600 kHz is given in Table 3.1.

Parameter	Parallel Mode (pF)	Series Mode (pF)	Parallel Mode (pF/cm)	Series Mode (pF/cm)
Inter-strip capacitance	0.83	1.51	1.04	1.89
Backplane capacitance/strip	0.25	0.30	0.31	0.38
Total calculated capacitance	1.08	1.81	1.35	2.27
Total measured capacitance	1.05	1.63	1.31	2.04

Table 3.1: Summary of the capacitance measurements obtained for a miniature detector with 8 mm strip length, at 100 V biasing voltage and 600 kHz frequency. These measurements includes 15% uncertainty, which comes from the measurement setup. The right columns shows capacitance per cm.

3.3 Capacitance Effect on Detector Noise

In the last section we discussed how to properly measure the detector capacitance. In this section the effect of detector capacitance on the SCT modules equivalent noise charge (ENC[1]) will be briefly discussed.
Different noise sources contributing to the total noise at the amplifier were introduced in section 2.3.2. The shot noise contribution which is independent of the detector capacitance is described there. Here will be presented only those sources, which are affected by detector capacitance.
One can show that the thermal noise at the input channel of the preamplifier is given by,

$$ENC_{cs} = \frac{e^3}{36q_e}\Big\{\frac{12kT_c}{T_p}(C_i + C_d)^2\Big(R_{bb} + \frac{kT_c}{2q_eI_c}\Big)\Big\}^{\frac{1}{2}} \tag{3.1}$$

where q is the electron charge, k is the Boltzmann constant, T_p is the peaking time of the shaper, R_{bb} is the base spreading resistance and T_c is the chip temperature. The capacitance C_i is the input capacitance of the amplifier and C_d is the detector capacitance. To calculate the total noise of a module, one has to include all the capacitances contributing to noise. Here we are only interested to see the effect of inter-strip and backplane capacitance, therefore we take the total detector capacitance to be equal to the sum of inter-strip and backplane capacitances, i.e $C_d = C_{int} + C_{back}$.
The ENC_{cs} can be calculated from Eq. 3.1, where the values of inter-strip and backplane capacitances are taken from Table 3.1. We assume that the module sensors will have capacitance per unit length in the same range and using $I_c = 220\ \mu$A, $T_p = 23$ ns and $R_{bb} = 272\ \Omega$ at $T_c = 8°$C, the ENC value is 1398 ± 210 electrons for an outer SCT module, where the error is assumed to come only from the test setup.
Noise from resistance of strips on the detector also depends on the detector capacitance and is given by,

$$ENC_{rs} = \frac{e^3}{36q_e}\Big\{\frac{3}{T_p}(C_i + C_d)^2\Big(4kT_sR_s\Big)\Big\}^{\frac{1}{2}} \tag{3.2}$$

where T_s is the sensor temperature. Using Eq. 3.2, the contribution to ENC_{rs} from inter-strip and backplane capacitance for resistance of 12 Ω/cm at sensor temperature of $-7°$C is 903 ± 135 electrons for an outer SCT module. The total noise contribution from the capacitance dependent sources is obtained by adding them in quadrature and gives a noise contribution of 1664 ± 250 electrons. The total noise of a module includes contributions from all noise sources e.g the capacitance

[1]ENC is the value of the input charge which gives a signal of the same amplitude as the rms output noise.

independent noise sources as described in chapter 2. Therefore the ENC will be a bit higher. The capacitance per cm and there-by the ENC calculated above are higher, however it should be noted that the miniature detector used is of second-grade quality.
It is clear that the noise is dominated by the capacitance dependent parts and therefore the capacitance understanding of the detector is very important. Higher noise occupancy can negatively affect the detector efficiency and therefore its proper understanding is very important. This will be the topic of discussion in the remaining part of the chapter. The noise occupancy will be described in the next section.

3.4 Noise Occupancy vs Threshold

In the presence of Gaussian noise, the noise occupancy as a function of threshold is described by the complementary error-function and the probability p of surpassing a threshold τ is given by,

$$p(\tau) = \frac{1}{2}\mathrm{erfc}(\frac{\tau}{\sqrt{2}\sigma}) \tag{3.3}$$

The noise occupancy has been calculated from Eq. 3.3 for various fixed sigma values as shown in Fig. 3.12. The specification for noise occupancy is indicated as a horizontal line. For a Gaussian noise sigma of about 1900 electrons, the noise occupancy reaches the specification at 1fC threshold. For a noise value of 2200 electrons the threshold should be raised to 1.16 fC in order to the specification.

3.4.1 Efficiency vs Threshold

The detection of charged particles by measuring their energy loss in thin silicon has led to widespread studies of the corresponding energy loss spectrum and is described in detail in ([42]–[45]). The statistical nature of the ionization process during the passage of a charged particle through matter results in large fluctuations of energy loss in absorbers, which are thin compared with the particle range. The probability density function describing the distribution of energy loss Δ in absorber thickness x is called the Landau distribution [46]. The Landau probability density function is given by,

$$\begin{aligned} f_L(x,\Delta) &= \frac{1}{\xi}\phi(\lambda) \quad \text{where} \\ \phi(\lambda) &= \frac{1}{2\pi\imath}\int_{c-\imath\infty}^{c+\imath\infty} exp(\lambda u + u\ln u)du \end{aligned}$$

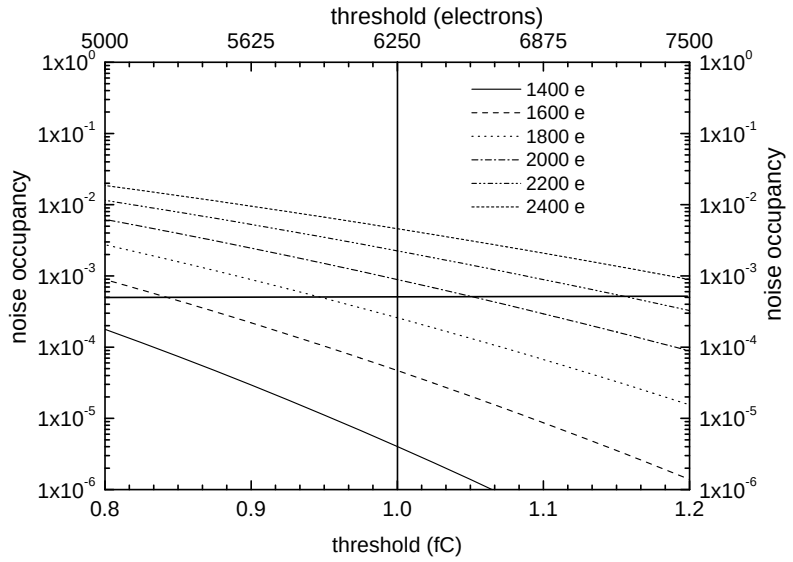

Figure 3.12: Noise occupancy vs threshold. Different curves correspond to different values of Gaussian noise. The SCT specification for noise occupancy is 5×10^{-4} and is indicated by a horizontal straight line.

$$\lambda = \frac{1}{\xi}\Big[\Delta - \xi(\ln\xi - \ln\frac{I^2}{\epsilon_m} - \beta^2 + 1 - C)\Big] \tag{3.4}$$

The quantity ϵ_m represents the maximum energy transferred to an atomic electron in a single collision with the incident particle of mass m and velocity βc. The parameter I is the average logarithmic excitation energy and has a value of 174 eV. The constant C is the Euler constant $C \approx 0.577215$ and the Landau parameter ξ depends on the material and also on the thickness traversed. The parameter ϵ_m and ξ are given by,

$$\begin{aligned} \epsilon_m &= 2m_e c^2\beta^2\gamma^2 \quad \text{with} \\ \gamma &= (1-\beta^2)^{\frac{1}{2}} \end{aligned} \tag{3.5}$$

and,

$$\begin{aligned} \xi &= \frac{2\pi z^2 e^4}{m_e c^2}\frac{NZx\rho}{A\beta^2}, \\ &= 0.01534(\frac{z^2}{\beta^2}\frac{Z}{A}x\rho) \quad \text{keV}, \\ &= 5.08 \quad \text{keV}, \quad \text{for 285 } \mu\text{m Si detector} \end{aligned} \tag{3.6}$$

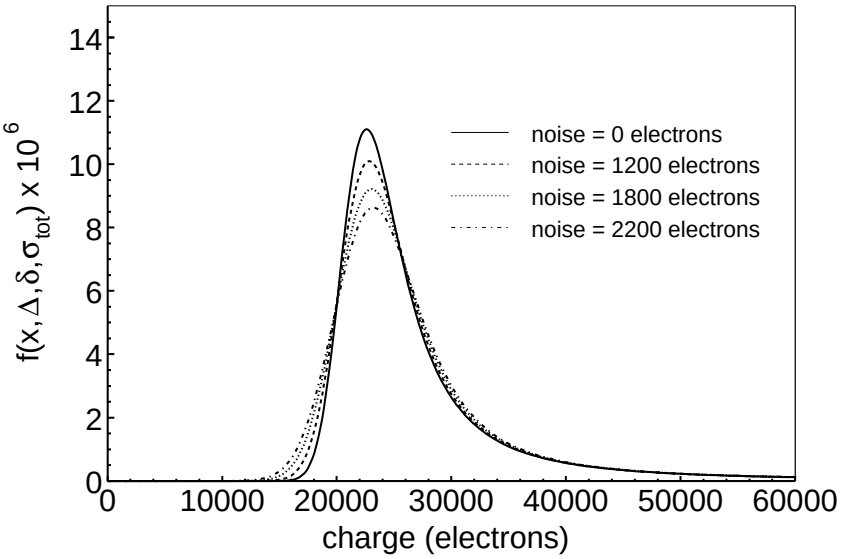

Figure 3.13: Corrected Landau distribution for 285 μm Si convoluted with a gaussian as described by Eq. 3.13. With the increase of Gaussian noise sigma, the width of the distribution increases. All curves include the binding energy correction for electrons with a width of $\delta_2 = 5$ keV.

where N is the Avagadro number, m_e and e are the electron mass and charge, respectively, z is the charge of the incident particle, and Z, A and ρ are the atomic number, atomic weight and density (g/cm^3) of the material.
The universal function ϕ has maximum at $\lambda \approx -0.225$, which corresponds to the most probable energy loss Δ_{mp} of the Landau distribution i.e $f_L(x, \Delta_m) = \frac{\phi(\lambda_0)}{\xi}$ and therefore λ in Eq. 3.4 becomes,

$$\begin{aligned} \lambda &= \frac{\Delta - \Delta_{mp}}{\xi} + \lambda_0 \quad \text{with} \\ \Delta_{mp} &= \xi\Big[\ln\frac{\epsilon_m \xi}{I^2} + 0.200 - \beta^2 - \delta\Big] \end{aligned} \tag{3.7}$$

the density effect denoted by δ is included in the expression of most probable energy loss which had not been used by Landau. Using the expression for $\delta = \ln\gamma^2 - 4.447$ from Eq. (4.9) of reference [47] for high-energy particle (i.e $\gamma \equiv (1-\beta^2)^{\frac{1}{2}} > 100$) and taking $\beta \simeq 1$, Eq. 3.7 becomes,

$$\begin{aligned} \Delta_{mp} &\simeq \xi\Big[\ln\frac{\epsilon_m \xi}{I^2} - \ln\gamma^2 + 3.647\Big] \\ &\simeq \xi\Big[\ln\frac{2m_e c^2 \xi}{I^2} + 3.647\Big] \quad \text{keV}, \quad \text{using } \epsilon_\text{m} \text{ from Eq. 3.5} \end{aligned} \tag{3.8}$$

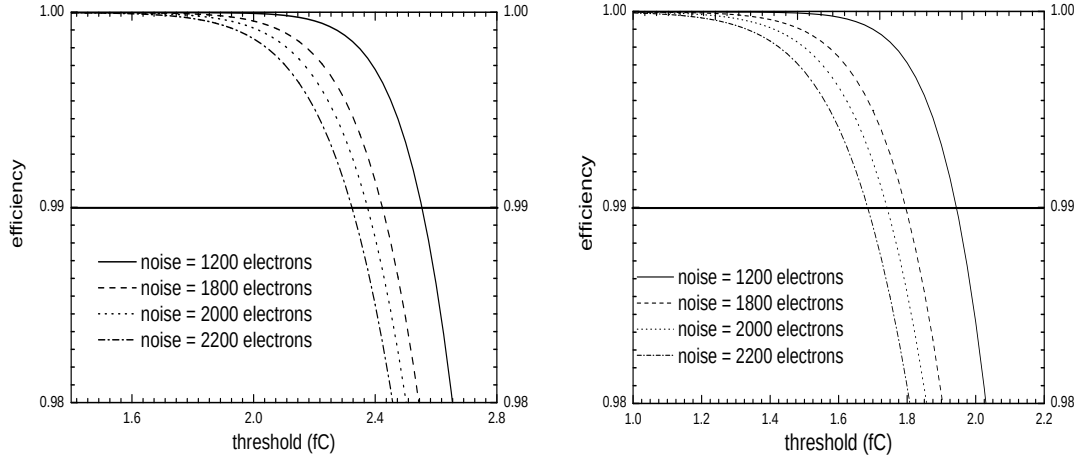

Figure 3.14: Efficiency as a function of threshold for different values of noise at 90% charge collection efficiency (a) and 70% charge collection (b). The SCT efficiency specification is indicated by a straight line.

Putting ξ from Eq. 3.6 for 285 μm detectors and $I = 174\ eV$ gives,

$$\Delta_{mp} \simeq 79.8 \quad \text{keV} \tag{3.9}$$

The Landau theory treats the electrons in very thin absorbers as free. To take into account the atomic binding of the electrons, the corrected energy-loss distributions can be expressed as the convolution of a Gaussian function with a Landau distribution as done in [45] and [47]. Thus

$$f_L(x, \Delta, \sqrt{\delta_2}) = \frac{1}{\sqrt{2\pi\delta_2}} \int_{-\infty}^{+\infty} f_L(x, \Delta') \times exp(-\frac{(\Delta - \Delta')^2}{2\delta_2}) d\Delta' \tag{3.10}$$

where $f_L(x, \Delta, \sqrt{\delta_2})$ is the modified Landau distribution with $\delta_2 = \sigma^2$ given by,

$$\delta_2 = \frac{8}{3}\xi \sum_i l_i (Z_i/Z) \ln(2m_e c^2 \beta^2 / l_i) \tag{3.11}$$

where Z_i is the number of electrons in the ith shell of the stopping material, l_i is the ionization potential of the ith shell, and the summation is performed over the shells for which $l_i < 2m_e c^2 \beta^2$. The Gaussian width $\sqrt{\delta_2}$ has been measured for a 300 μm silicon detector and for different incoming momenta. The values are given in the Table II of reference [45]. In this chapter the value used for $\sqrt{\delta_2}$ is 5 keV.
Eq. 3.10 represents the corrected Landau distribution with 100% charge collection

efficiency and no detector noise. The standard deviation σ_{tot} of the Gaussian distribution can be defined to take also into account the detector and electronic noise,

$$\sigma_{tot} = (\delta_2 + \sigma^2_{noise})^{\frac{1}{2}} \tag{3.12}$$

where σ_{noise} is the standard deviation of the Gaussian noise distribution. The probability distribution function can therefore finally be written as,

$$f_L(x, \Delta, \sqrt{\delta_2}, \sigma_{tot}) = \frac{1}{\sigma_{tot}\sqrt{2\pi}} \int_{-\infty}^{+\infty} f_L(x, \Delta') \times exp(-\frac{(\Delta - \Delta')^2}{2\sigma^2_{tot}}) d\Delta' \tag{3.13}$$

To calculate the efficiency, we need to evaluate Eq. 3.13. The integral can not be solved analytically but has to be calculated numerically. We used ROOT [49] to evaluate the above equation, where the Landau density function $\phi(\lambda)$ in ROOT is adapted from CERNLIB [50]. The convolution integration is done by summation in ROOT.
Fig. 3.13 shows the convoluted Landau distribution for different values of noise. It can be seen that with increasing noise the distribution broadens leading to lower efficiencies.
To calculate the detection efficiency, the effects caused by detector capacitances need to be considered. The inter-strip capacitance as described in the section 3.1.4 creates cross-talk between channels. In the ATLAS SCT modules most of the charge is collected on a single strip. Charge shared between neighbouring strips cannot be re-clustered in the binary readout scheme as it is predominantly below threshold. It is confirmed in a test beam [51] that clusters of more than one strip make up only a small fraction of the total and are concentrated in a narrow region in the center between strips.
We consider that charge is deposited on one strip and 10%[2] of the signal is lost from the strip and appears on its neighboring strips. Therefore, for 90% charge collection and different values of noise, the efficiency as a function of threshold is shown in Fig. 3.14 (a). The same for 70% charge collection, which corresponds to irradiated detector is shown in Fig. 3.14 (b). It can be seen that the efficiency is well above the SCT specification of 99% for a wide range of threshold. In practice the efficiency of the ATLAS SCT modules will be deteriorated by inefficient channels: such as dead electronic cells, noisy strips or due to bonding problems. The effect of inefficiencies on the single track reconstruction efficiency will be discussed in detail in chapter 6.

[2]The charge loss due to cross-talk between neighbouring channels is expected to be responsible for a charge loss of 6% i.e∼0.26 fC and the loss of median charge due to diffusion is 0.13-0.16 fC as confirmed by test beam measurements described in [52]. Therefore total charge loss due to charge sharing is expected to be∼ 0.4 fC i.e 10% of the median charge of 4 fC.

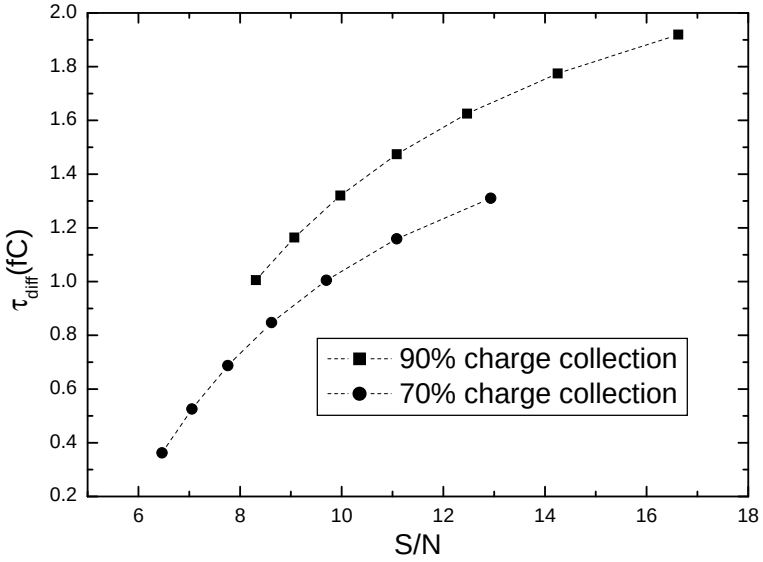

Figure 3.15: Difference between the threshold corresponding to efficiency and noise occupancy specification as a function of signal to noise ratio. The signal here is the most probable value of the distribution.

3.4.2 Difference between efficiency and noise occupancy specification threshold

It is evident in Fig. 3.12 and Fig. 3.14, that for a fixed noise, the specification thresholds for efficiency and noise occupancy are different. Here the difference between these two specification thresholds is denoted by τ_{diff}. This quantity has been calculated for different signal to noise ratios. For a fixed signal of most probable value 3.2 fC, τ_{diff} is plotted as a function of signal to noise ratio in Fig. 3.15. It is clear that with increasing noise the width of the window decreases, because the threshold needed to keep the noise occupancy at the specification value will increase, and the threshold corresponding to efficiency specification will decrease. For a noise value of 1800 electrons and 90% charge collection, the width of the threshold window is 1.5 fC. For 30% loss of charge as expected for irradiated detectors after 10 years of operation in ATLAS, the width of the threshold window as a function of signal to noise ratio is also shown in Fig. 3.15. For 2200 electrons which corresponds to signal to noise ratio of 7 and is expected after 10 years of operation [51], the corresponding threshold window is 0.52 fC. Thus the threshold window after irradiation is narrow. This effect is also confirmed by test beam data [51, 53], although the measured width of the threshold window is lower than the above calculated values, which may be due to differences between the simple model described in the previous section and more complicated charge loss and charge collection processes in the SCT modules.

Chapter 4

Measurement of Common Mode Noise in Binary Read-Out Systems

Estimators for the magnitude of common mode noise in a binary read-out system are studied using a simple Monte-Carlo program, and the theoretical background is explained. The occupancy per event is found to be a simple but very sensitive and specific test for common mode noise, which also leads to a quantitative measure of common mode noise. We introduce the observable Γ, which at 50% occupancy directly gives the common mode noise contribution. The autocorrelation function and the correlation matrix in addition provide information on the coherence length of common mode noise.
A function is proposed which can be used to measure common mode noise from the observable Γ for different occupancies. The statistical effects on the measurement of Γ are reported at the end of the chapter.

4.1 Introduction

This chapter describes methods to detect and measure common mode noise when silicon microstrip detectors are read out using a binary scheme in which the signals are compared to a threshold and converted to binary information very early in the read out chain, i.e. on the front end chip. However, the methods are very general and can be applied to any analysis of binary data emerging from analogue signals which may be affected by coherent distortions.
Common mode noise refers to a variation of the signal which affects groups of channels in a coherent way. It can be caused by a common electromagnetic pick-up, noise on the supply voltage etc. It adds to the noise and can eventually even create artificial hit patterns. The susceptibility to common mode noise depends

both on the individual detector module and on the system environment. The spectrum of the common mode noise is a priori unknown. Most difficult is the detection of Gaussian common mode noise.
In an analogue read-out scheme the common mode contribution can be measured on an event-by-event basis. For a group of channels the pedestals are subtracted from the raw signals and channels with real hits are excluded. Then the average signal seen on the channels is a good approximation to the common mode noise contribution, as the single channel random noise cancels to a large extent (depending on the number of channels in the group). This common mode contribution can be subtracted from the signals.
Common mode is of particular concern in binary read-out systems as it can not be measured on an event-by-event basis and therefore a correction for common mode is impossible. It can only be estimated on a statistical basis, analysing a sample of events. Therefore, it is vital for a digital system to have negligible common mode noise. This calls for methods to detect and measure coherent effects, which can then be used in the system evaluation and optimisation.
A simple Monte-Carlo program has been developed with which different methods can be tested. This program is described in the next section. The following section deals with the different methods.

4.2 Monte-Carlo Simulation

For the studies in this note a Gaussian common mode noise has been assumed as this is most difficult to detect. The generation of the data proceeds in the following steps:

- for a number of channels signals are generated, event-by-event, from a Gaussian distribution of a width which represents the single channel random noise of standard deviation σ

- for a group of channels for which a coherent noise with standard deviation s is to be simulated a single number is taken from a Gaussian distribution of width s (event-by-event) and added to all signals from that group

- a threshold τ is applied to all signals which generates a stream of binary data. In order to simulate channel-to-channel variations of threshold, gain and offset, a fixed set of Gaussian random numbers (one per channel) is generated at the beginning of a run. These numbers are added to the signals before the threshold is applied, if channel-to-channel threshold variation is to be simulated.

All signal and noise levels are normalised to the single channel random noise σ. Also the threshold τ is in units of σ. Unless otherwise stated, threshold variations are distributed with standard deviation 0.3σ.

4.3 Methods for Detection and Measurement of Common Mode Noise

4.3.1 Excess Noise

If the single channel random noise is well known, the common mode noise can be detected as excess noise. This method requires a very reliable understanding of the expected single channel random noise and it is not sensitive to the coherence of common mode. Therefore this is at best a very indirect measure of common mode noise. It is mentioned here only because it is sometimes used to guess the presence of common mode noise in a system. It will not be considered further.

4.3.2 $\log(occupancy)$ *vs.* $(threshold)^2$

If the intrinsic noise in a system is purely Gaussian, and in absence of other noise sources, the probability p of surpassing a threshold τ is given by the complementary error function

$$p(\tau) = \frac{1}{2}\mathrm{erfc}\left(\frac{\tau}{\sqrt{2}}\right) \tag{4.1}$$

For thresholds much larger than the single channel random noise ($\tau \gg 1$) this probability can be approximated by

$$p(\tau) \approx \frac{1}{\sqrt{2\pi}\tau}\exp\left(-\frac{\tau^2}{2}\right) \Rightarrow \ln(p) \approx -\frac{1}{2}\tau^2 - \ln\left(\sqrt{2\pi}\tau\right) \tag{4.2}$$

using the asymptotic series for the complementary error function [54]. In fact this is already a good approximation for $\tau > 1.5$, leading to the conclusion that purely Gaussian noise should give a straight line in the plot of the logarithm of the occupancy vs the square of the threshold over much of the useful range. Occupancy refers to the (normalised) total number of hits in all channels in a run. The power of this plot is to show non-Gaussian noise contributions as deviations from this linear fall-off. Gaussian noise contributions, on the other hand, just change the slope of the linear fall-off. As in the previous method, a good knowledge of the expected single channel random noise is needed if further conclusions about Gaussian common mode are to be drawn. This method also cannot distinguish between correlated and uncorrelated noise. Therefore it is not suitable to detect Gaussian common mode noise. Fig. 4.1 shows this plot for simulations without

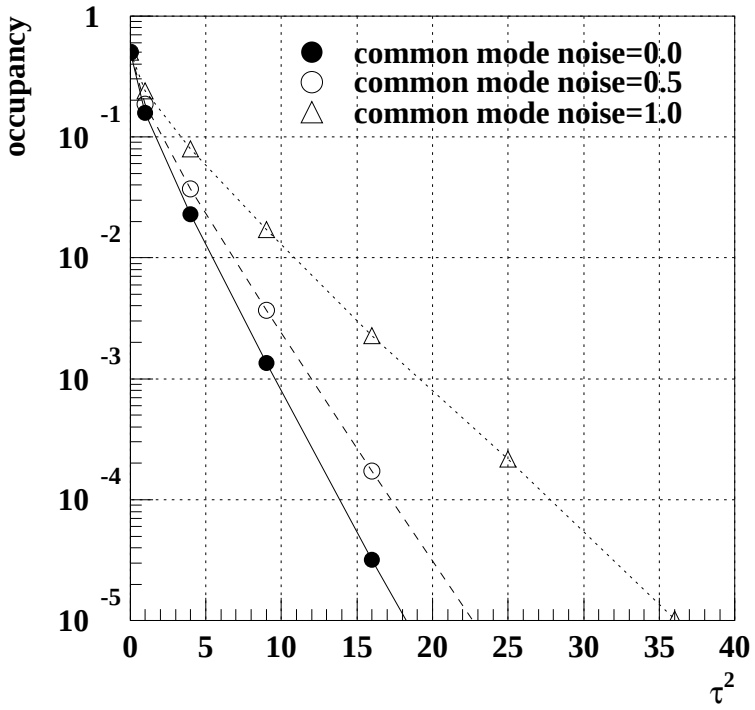

Figure 4.1: Occupancy (on a logarithmic scale) versus the square of the threshold τ (in units of the single channel random noise σ). The curves show the result of the simulation without common mode noise (solid circles), and with common mode noise of standard deviation 0.5σ (open circles) and 1.0σ (open triangles). Threshold variation across the channels is not included in this plot.

common mode noise, and with common mode noise of standard deviation 0.5σ and 1.0σ.

4.3.3 Raw Data Plot

The most basic display of the data is a plot in which the hit map is plotted in the plane spanned by channel number and event number. This plot is extremely useful in understanding the data quality as it shows immediately

- dead/noisy/sick channels

- channel occupancy
- uniformity across the channels
- uniformity across the events in a run and
- coherent effects on the channels in individual events.

Although this plot does not provide quantitative results, it is clearly an important diagnostic tool. Fig. 4.2 shows this plot for simulated events with a common mode noise of standard deviation 0.0σ (a), 0.5σ (c) and 1.0σ (e). The threshold is set to zero, i.e. the point of 50% efficiency. The first plot, from a simulation without common mode noise, shows some vertical band structure which is caused by the simulated threshold variation. The second plot, with common mode noise of standard deviation half that of the individual channel random noise, clearly shows an additional horizontal structure. It is even more pronounced in the third plot (common mode of same size as individual channel random noise).

4.3.4 Occupancy per Event

Common mode noise should lead to a large number of hits in some events and very few in others, compared with the expectation from the single channel random noise. Therefore the distribution of the number of hits in an event N_e should be a measure of coherent noise. Fig. 4.2 (b), (d) and (f) show the histograms of the number of hits per event (N_e) for the three cases considered in this figure. The number of simulated channels is 768. While the distribution is narrow without common mode noise (Fig. 4.2 (b)), it widens strongly when common mode noise is present ((d) and (f)). Actually one can easily calculate the width of the N_e distribution which is expected in the absence of common mode noise. In this case N_e has to follow a binomial distribution, which we denote as $\mathrm{Bin}(N_e; n, p(\tau))$ for n channels and a hit probability $p(\tau)$ for the given threshold τ. The mean number of hits is then

$$\overline{N_e} = \sum_{N_e=0}^{n} N_e \mathrm{Bin}(N_e; n, p(\tau)) = np(\tau). \tag{4.3}$$

Thus the probability p can be approximated by the observed mean number of hits per event divided by the number of channels n, and we find for the variance of the N_e distribution

$$\mathrm{Var}(N_e) = np(1-p) = \overline{N_e}\left(1 - \frac{\overline{N_e}}{n}\right) \tag{4.4}$$

Therefore the expected standard deviation can be calculated just from the observed average number of hits per event, without further assumptions. If the

observed distribution is wider, one can conclude that coherent noise is present. In a real system large channel-to-channel variations of the channel occupancy may be present, resulting for instance from large channel-to-channel threshold variations. It should be noted that these variations in general do not widen the N_e distribution. In the absence of common mode noise and for equal mean number of hits in all channels, the largest standard deviation is obtained for $\overline{N_e} = n/2$. A smaller or larger $\overline{N_e}$ leads to a more narrow distribution, according to the above formula. The N_e for a mixture of channels with different occupancies is the sum of values taken from narrow distributions and the resulting distribution itself will be narrow. If the observed $\overline{N_e}$ is close to $n/2$ and the channel occupancies vary, then the standard deviation calculated with the above formula is in fact an overestimate. Therefore a data distribution wider than this calculated standard deviation still indicates common mode noise.
In order to derive a measure for the common mode noise contribution, one has to calculate the mean and the variance of the N_e distribution in the presence of common mode noise. We note that the effect of a shift of the signal by a common mode noise contribution is equivalent to shifting the threshold by the same amount, but in the opposite direction. Therefore one can implement the effect of common mode noise by choosing the threshold τ in each event from a probability distribution $g(\tau)$. For the case of Gaussian common mode noise, which we will consider here, it is given by

$$g(\tau) = \frac{1}{s\sqrt{2\pi}} \exp\left(-\frac{(\tau - \tau_0)^2}{2s^2}\right), \tag{4.5}$$

where s is the standard deviation of the common mode noise in units of the single channel random noise σ, and τ_0 is the original threshold. The distribution of the number of hits per event N_e is then a superposition of binomial distributions for varying thresholds. Again, we call $\mathrm{Bin}(N_e; n, p(\tau))$ the binomial probability of having N_e hits in an event for n channels and a threshold τ, so that the hit probability $p(\tau)$ is given by eq. 4.1. The probability $P(N_e)$ to obtain N_e hits in an event when the threshold varies with $g(\tau)$ is then

$$P(N_e) = \int_{-\infty}^{\infty} \mathrm{Bin}(N_e; n, p(\tau)) g(\tau) d\tau \tag{4.6}$$

and the mean number of hits per event

$$\overline{N_e} = \sum_{N_e=0}^{n} N_e P(N_e) \tag{4.7}$$

$$= \int_{-\infty}^{\infty} \sum_{N_e=0}^{n} N_e \mathrm{Bin}(N_e; n, p(\tau)) g(\tau) d\tau \tag{4.8}$$

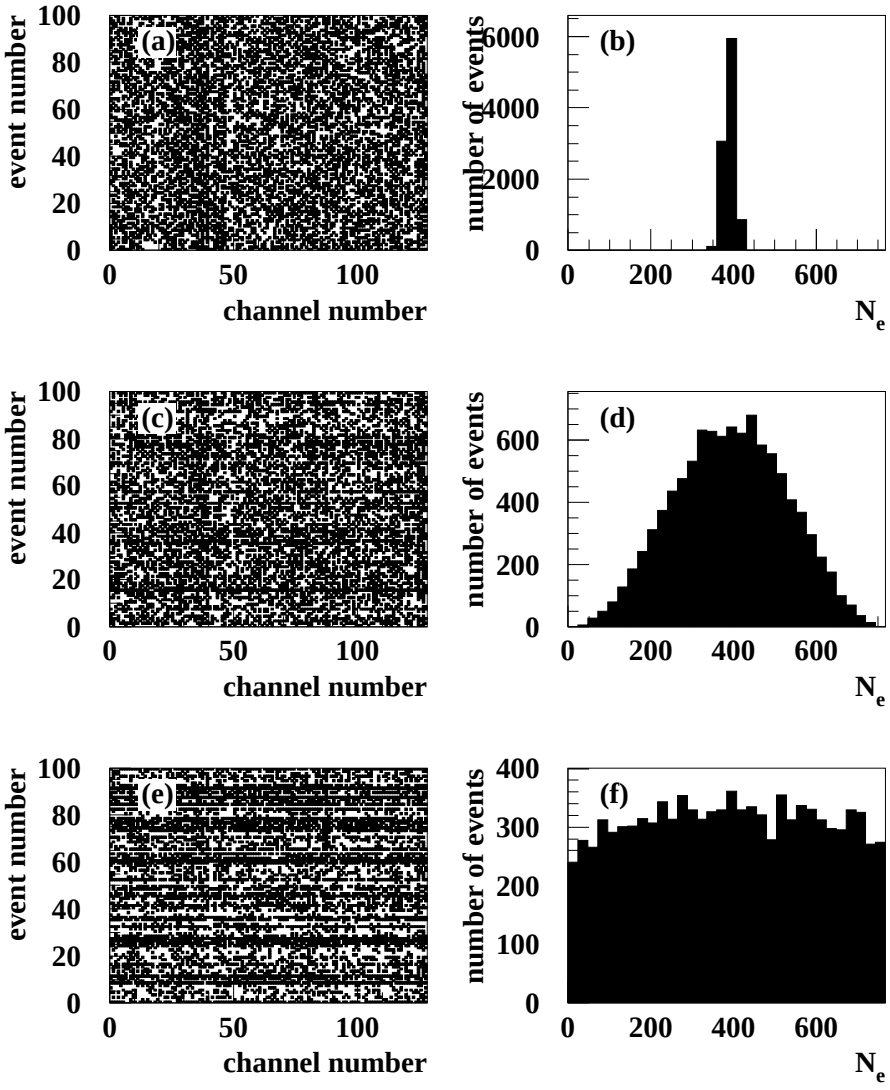

Figure 4.2: Hit map from simulations without common mode noise (a), and with common mode noise of 0.5σ(c) and 1.0σ(e). The corresponding histograms of the number of hits per event (N_e) are shown in (b), (d) and (f). 768 channels have been simulated, and the threshold has been set to zero.

$$= \int_{-\infty}^{\infty} np(\tau)g(\tau)d\tau. \tag{4.9}$$

The variance of N_e is

$$\begin{aligned}
\mathrm{Var}(N_e) &= \overline{N_e^2} - \overline{N_e}^2 && (4.10)\\
&= \left(\sum_{N_e=0}^{n} N_e^2 P(N_e)\right) - \overline{N_e}^2 && (4.11)\\
&= \int_{-\infty}^{\infty} \sum_{N_e=0}^{n} N_e^2 \mathrm{Bin}(N_e; n, p(\tau))g(\tau)d\tau - \overline{N_e}^2 && (4.12)\\
&= \int_{-\infty}^{\infty} \left(np(\tau)(1-p(\tau)) + (np(\tau))^2\right) g(\tau)d\tau - \overline{N_e}^2 && (4.13)\\
&= \overline{N_e} + (n^2-n)\int_{-\infty}^{\infty} p^2(\tau)g(\tau)d\tau - \overline{N_e}^2 && (4.14)\\
&= \overline{N_e}(1-\overline{N_e}) + n(n-1)\int_{-\infty}^{\infty} p^2(\tau)g(\tau)d\tau. && (4.15)
\end{aligned}$$

Here we have made use of the fact that for the binomial distribution $np(1-p) = \mathrm{Var}(N_e) = \overline{N_e^2} - \overline{N_e}^2 = \sum_{N_e=0}^{n} N_e^2 \mathrm{Bin}(N_e; n, p(\tau)) - (np)^2$.

At the 50% point (i.e. $\tau_0 = 0$, $\overline{N_e} = \frac{1}{2}n$) the integral in eq. 4.15 has a closed form [55]:

$$\begin{aligned}
\int_{-\infty}^{\infty} p^2(\tau)g(\tau)d\tau &= \frac{1}{4}\frac{1}{s\sqrt{2\pi}}\int_{-\infty}^{\infty}\left[\mathrm{erfc}\left(\frac{\tau}{\sqrt{2}}\right)\right]^2 \exp\left(-\frac{\tau^2}{2s^2}\right)d\tau && (4.16)\\
&= \frac{1}{4} + \frac{1}{2\pi}\tan^{-1}\left(\frac{s^2}{\sqrt{1+2s^2}}\right). && (4.17)
\end{aligned}$$

Solving eq. 4.15 for s we obtain in this way at the 50% point:

$$s^2 = \frac{\sin(\alpha)}{1-\sin(\alpha)}; \quad \text{with} \quad \alpha \equiv 2\pi\frac{\mathrm{Var}(N_e) - \frac{n}{4}}{n(n-1)}. \tag{4.18}$$

If the mean occupancy of the channels is 50%, then the common mode noise can be calculated from the observed mean and variance of the distribution of the number of hits per event using eq. 4.18.

A useful generalisation of this formula is found by identifying the $n/4$ term in eq. 4.18 with the binomial variance of N_e at the 50% point. We introduce the observable Γ defined as

$$\Gamma^2 \equiv \frac{\sin(\tilde{\alpha})}{1-\sin(\tilde{\alpha})}; \quad \text{with} \quad \tilde{\alpha} \equiv 2\pi \frac{\mathrm{Var}(N_e) - \overline{N_e}\left(1 - \frac{\overline{N_e}}{n}\right)}{n(n-1)}. \tag{4.19}$$

In the absence of common mode noise Γ is zero no matter how many channels there are or how the threshold is set. Fig. 4.3 shows the Γ distribution versus the common mode noise, as predicted by the simulation. The number of channels was set to $n = 768$. The different symbols correspond to different threshold settings. Γ increases strongly for increasing common mode noise. The strongest effect is observed for zero threshold, i.e. at the 50% point. In this case, by definition, the quantity Γ approximates the ratio of common mode noise over single channel random noise

$$\text{common mode noise} \approx \Gamma \times \text{single channel random noise} \quad \text{for } \overline{N_e} \approx \frac{n}{2} \tag{4.20}$$

The effect of channel-to-channel threshold variations is weak, as can be seen by the comparison of the solid and dotted lines in fig. 4.3, which represent the simulation results without and with channel-to-channel threshold variations of standard deviation 0.3σ, respectively.
It is obvious that the N_e plot and the observable Γ are very sensitive to common mode noise. In addition this method is highly specific to the coherence as any kind of single channel random noise does not broaden the N_e distribution.

4.3.5 Correlation Matrix

The most detailed information on the correlation between the signals from different channels is obtained from the correlation matrix. If we consider two channels x and y, then the correlation between them is

$$cor_{xy} = \frac{\langle xy \rangle - \langle x \rangle \langle y \rangle}{\sigma_x \sigma_y} \tag{4.21}$$

The standard deviation is

$$\sigma_x = \sqrt{\langle x^2 \rangle - \langle x \rangle^2} = \sqrt{\langle x \rangle - \langle x \rangle^2} \tag{4.22}$$

(similarly for y) as for the binary data $x_i = x_i^2$. Observing that $\langle x \rangle$ is just the occupancy in channel x, which we call Ω_x, and that $\langle xy \rangle$ corresponds to the

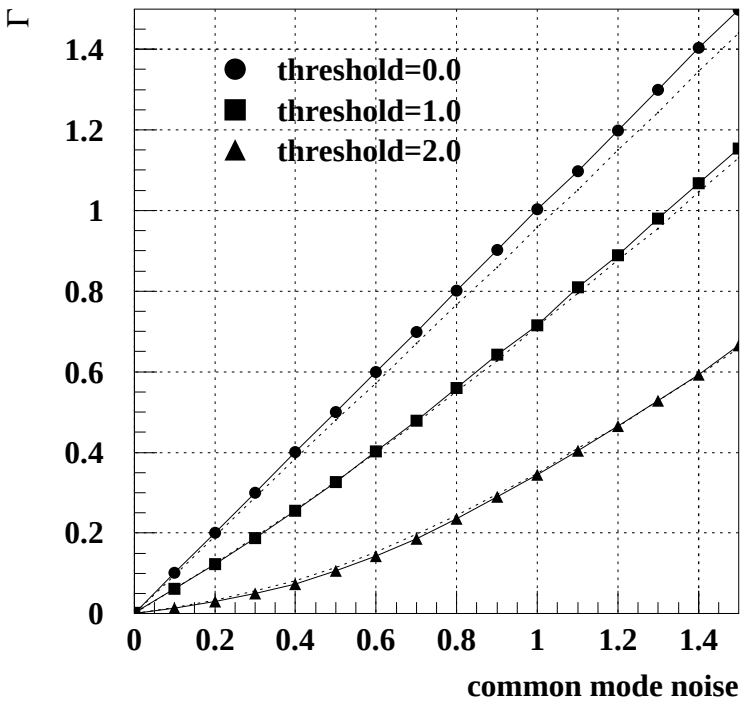

Figure 4.3: Γ as a function of the common mode noise. The different symbols correspond to different threshold settings, as indicated in the figure. Solid lines indicate the results obtained without simulation of channel-to-channel threshold variation, dotted lines include such a variation with standard deviation 0.3σ.

occupancy of a hypothetical channel representing the logical AND of the channels x and y (called $\Omega_{x\cdot y}$) we obtain for the correlation of channels x and y

$$cor_{xy} = \frac{\Omega_{x\cdot y} - \Omega_x \Omega_y}{\sqrt{\Omega_x - (\Omega_x)^2}\sqrt{\Omega_y - (\Omega_y)^2}} \tag{4.23}$$

with

$$\Omega_x = \frac{\text{number of events with a hit in channel } x}{\text{total number of events}} \tag{4.24}$$

$$\Omega_y = \frac{\text{number of events with a hit in channel } y}{\text{total number of events}} \tag{4.25}$$

$$\Omega_{x\cdot y} = \frac{\text{number of events with a hit in channels } x \text{ and } y}{\text{total number of events}} \tag{4.26}$$

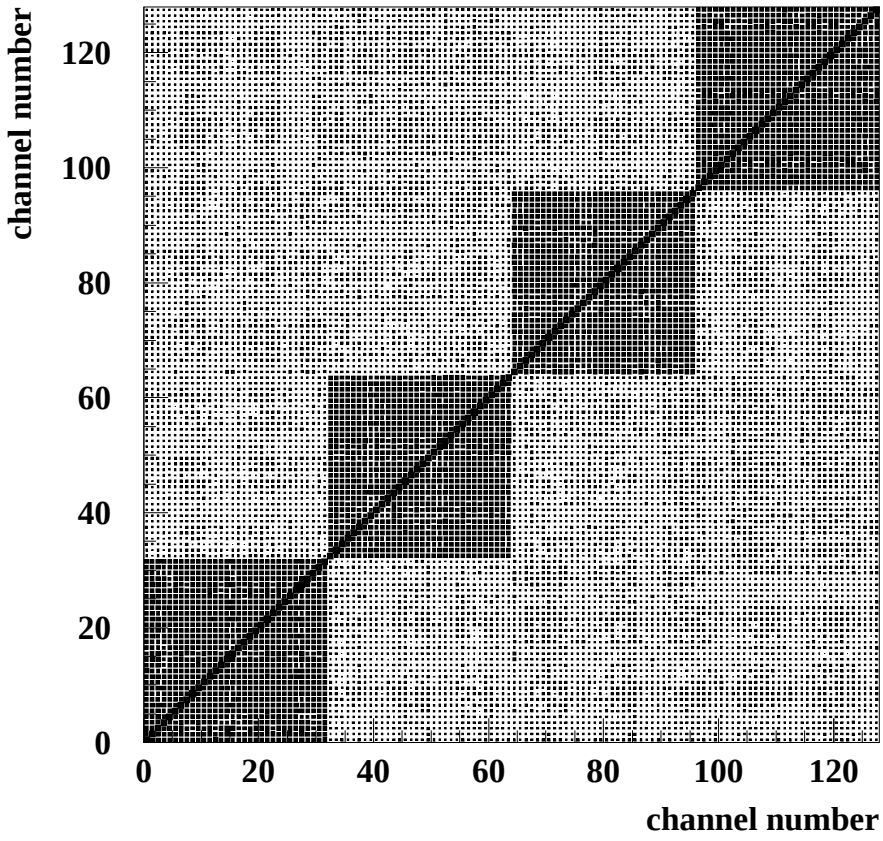

Figure 4.4: Graphical representation of the correlation matrix for a simulation in which common mode noise is generated for groups of 32 channels.

Calculating this quantity for all pairs of channels results in the full correlation matrix. In the absence of coherent noise (and for infinite statistics) the correlation cor_{xy} of two channels vanishes, no matter what the occupancy of the two individual channels is. Common mode noise will most likely lead to a positive correlation. In addition to the detection and quantification of common mode noise the correlation matrix provides information about the range of coherence. If common mode effects are bound, for instance, to each read-out chip and there are several chips in the system, the matrix will show square regions of non-zero correlation. Fig. 4.4 shows the correlation matrix for the case when common mode noise is simulated for groups of 32 channels. If the common mode is due to some cross talk between channels, the correlation matrix will show a band structure around the diagonal.

4.3.6 Autocorrelation

Autocorrelation is a powerful technique used in signal processing applications for revealing hidden periodicities in apparently random noise [56]. It is normally applied by multiplying the received signal by a copy of itself which is shifted in time; this is equivalent to taking one vertical column of the left plots in fig. 4.2 and multiplying it by a time-displaced copy of itself. For our purposes, we are looking for channel correlations rather than time correlations, and we shall define a discrete form of the autocorrelation function as:

$$A(m) = \sum_{i=1}^{n} x_i x_{(i+m)_{\mathrm{mod}n}}, \tag{4.27}$$

where n is the number of channels, and x_i is the signal in the i^{th} channel, here defined so that a 'hit' has a numerical value $+1$ and a 'zero' has value -1 (this facilitates later calculations). In this form, by analogy with fig. 4.2, we are taking a horizontal row and multiply it by a channel-displaced copy of itself. In our definition, channels which are shifted beyond n are 'wrapped around' using the mod function. The resulting function, $A(m)$, is the autocorrelogram for a given event.
At the 50% threshold (zero, in this case) and without correlated noise the time averaged value for $A(m)$ is

$$A_0(m) = \begin{cases} n \text{ for } m = 0 \\ 0 \text{ otherwise} \end{cases} \tag{4.28}$$

At other values of the threshold, the autocorrelogram may be calculated by considering the expectation value for the variable $x_i x_j (i \neq j)$. Given that the two are independent and obey Gaussian statistics, the average value is

$$\overline{x_i x_{j\neq i}} = (1-2p)^2 = \mathrm{erf}^2\left(\frac{\tau}{\sqrt{2}}\right) \tag{4.29}$$

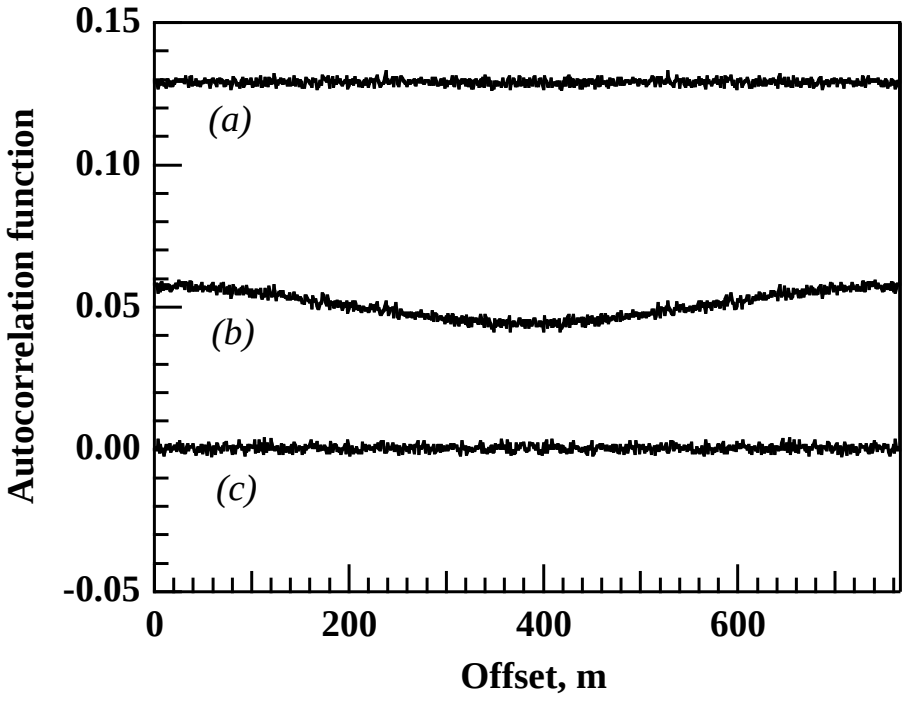

Figure 4.5: Normalized autocorrelation versus the offset m for a simulation of 768 channels. (a) constant common mode noise of 0.5σ across the channels, (b) common mode noise varying from 0.1σ at the centre channel to 0.5σ at the edges, (c) incoherent noise varying from 0.1σ at the centre channel to 0.5σ at the edges. Channel-to-channel threshold variation was not simulated.

since $p(\tau)$ is given by eq. 4.1.
The effect of common mode noise is to effectively change the threshold about its mean value across all the channels. The analogous result to eq. 4.29 in this case is

$$\overline{x_i x_{j\neq i}} = \frac{1}{s\sqrt{2\pi}} \int_{-\infty}^{\infty} \exp\left(-\frac{(\tau-\tau_0)^2}{2s^2}\right) \mathrm{erf}^2\left(\frac{\tau}{\sqrt{2}}\right) d\tau \tag{4.30}$$

where s is the common mode standard deviation and the common mode noise is assumed to be Gaussian. This function is most sensitive to common mode noise when $\tau_0 = 0$, for which the integral has the closed form in eq. 4.31.

$$\overline{x_i x_{j\neq i}} = \frac{2}{\pi} \tan^{-1}\left(\frac{s^2}{\sqrt{1+2s^2}}\right). \tag{4.31}$$

For small values of common mode noise, the function erf^2 in eq. 4.30 may be

replaced by its Maclaurin expansion around $\tau_0 = 0$, which yields

$$\overline{x_i x_{j\neq i}} \approx \frac{2}{\pi} s^2 \approx 0.64 s^2. \tag{4.32}$$

To explore the autocorrelation method, a simulation was performed as described in section 4.2 for 1000 events and 768 channels. The intrinsic noise standard deviation σ was set to 1 and the common mode varied to illustrate three situations:

(a) common mode noise constant across the channels, with standard deviation $s = 0.5\sigma$

(b) common mode noise varying from 0.1σ at the centre channel to 0.5σ at the edges

(c) additional incoherent noise varying from 0.1σ at the centre channel to 0.5σ at the edges

For each of these situations, the autocorrelogram was calculated at threshold $\tau = 0$. Each of the autocorrelograms has been normalised to its maximum value (= 768). The results are shown in fig. 4.5. While the autocorrelogram of (b) is highly suggestive of a position dependence of the underlying common mode noise, it is important to realise that the same autocorrelogram would result from common mode noise which is maximum at the centre and minimum at the edges, due to the commutativity of the multiplication. Interpretation is therefore not as intuitive as at first sight, and the abscissa should not be interpreted as the channel number, but as an offset.

4.4 Measurement of Common Mode Noise using the Observable Γ

This section describes a method to measure common mode noise from the observable Γ for arbitrary occupancy. At 50% occupancy Γ is a linear function of common mode noise as described in section 4.3.4. In presence of a fixed amount of common mode noise, the Γ versus occupancy follows nearly a parabolic shape. A function is proposed which can fit Γ versus occupancy for a given common mode noise. Therefore, for a measured Γ value, common mode noise can be calculated for different occupancies using this function.
A simple Monte-Carlo program is used as described in section 4.2 and [57] to simulate Γ as a function of occupancy for different values of common mode noise with the following settings,

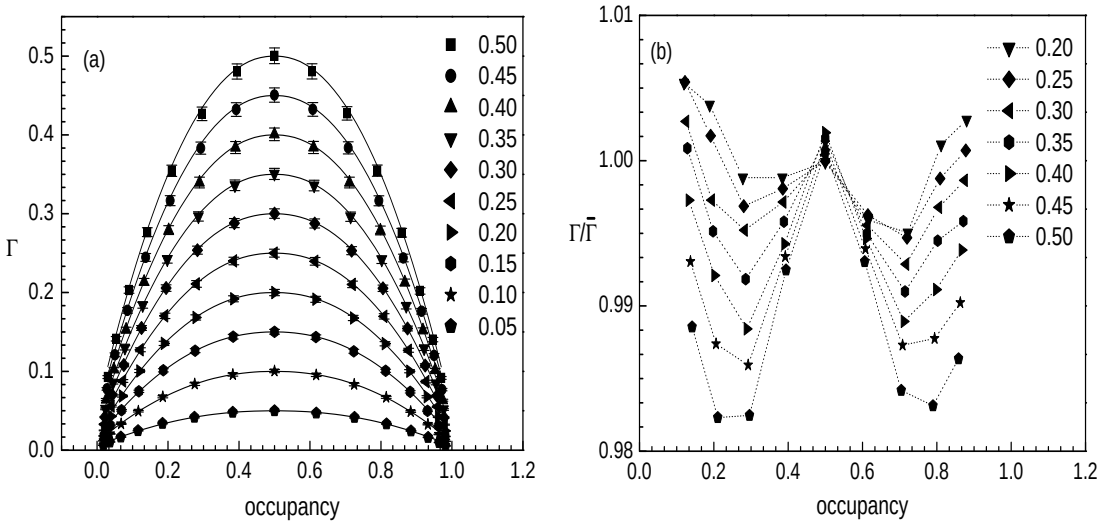

Figure 4.6: (a) Simulation data for Γ versus occupancy for different fixed values of common mode noise. The fit function $\overline{\Gamma}$ shown by solid lines fits within errors bars (which are defined as ±2%) over a wide range of occupancy. (b) Ratio of simulated over calculated Γ versus occupancy. Different lines correspond to different values of common mode noise.

- For a number of channels signals are generated, event by event from a Gaussian distribution of standard deviation 1 which represents single channel random noise

- A number is taken event by event from a Gaussian distribution of width s and added to all channels to simulate common mode noise

- To get different occupancies the threshold is varied

Γ as a function of occupancy for different common mode noise values is shown in Fig. 4.6 (a). The linear dependence of Γ on common mode noise at the 50% point can be seen in the plot. Γ is symmetric about 50% occupancy. A good fit of Γ as a function of occupancy and common mode noise is given by

$$\overline{\Gamma} = \Big(\frac{Common\ Mode\ Noise}{Single\ channel\ random\ noise}\Big)\Big(1 - \frac{\Big(|0.5 - Occupancy|\Big)^{2.15}}{0.25}\Big) \qquad (4.33)$$

This parametrization can be solved for the common mode noise contribution and can be used to estimate the common mode noise contribution from the measured

Γ i.e

$$\frac{Common\ Mode\ Noise}{Single\ channel\ random\ noise} \approx \frac{\Gamma}{\left(1 - 4 \times \left(|0.5 - Occupancy|\right)^{2.15}\right)} \tag{4.34}$$

For known values of common mode noise Eq. 4.34 fits within ±2% to the simulated data in Fig. 4.6 (a) over a wide range of occupancy. The ratio of simulated Γ to that calculated using Eq. 4.34 is plotted in Fig. 4.6 (b). Fluctuations are roughly symmetric around 50% occupancy.
The statistical error on this common mode noise measurement comes only from the error on Γ, as is clear in Eq. 4.34, neglecting the error on the occupancy. The error on Γ^2 given in Eq. 4.19 can be calculated using standard error propagation formulae [58] and is given by,

$$\begin{aligned}
\sigma^2_{\Gamma^2} &= \Big(\frac{\mathrm{d}\Gamma^2}{\mathrm{d}\overline{N_e}}\Big)^2 \sigma^2_{\overline{N_e}} + \Big(\frac{\mathrm{d}\Gamma^2}{\mathrm{d}Var(N_e)}\Big)^2 \sigma^2_{Var(N_e)};\ \text{ with} \\
\frac{\mathrm{d}\Gamma^2}{\mathrm{d}\overline{N_e}} &= \frac{2\pi}{n(n-1)}\Big(\frac{2\overline{N_e}}{n} - 1\Big)\Big(\frac{\cos(\tilde{\alpha})}{\Big[1 - \sin(\tilde{\alpha})\Big]^2}\Big) \\
\frac{\mathrm{d}\Gamma^2}{\mathrm{d}Var(N_e)} &= \frac{2\pi}{n(n-1)}\Big(\frac{\cos(\tilde{\alpha})}{\Big[1 - \sin(\tilde{\alpha})\Big]^2}\Big)
\end{aligned} \tag{4.35}$$

In the absence of common mode noise N_e follows binomial statistics and therefore errors on mean and variance of N_e in Eq. 4.35 are given by,

$$\begin{aligned}
\sigma^2_{\overline{N_e}} &= \frac{\sigma^2}{N} \\
\sigma^2_{Var(N_e)} &= \frac{1}{N}\Big(\sigma^2\Big(1 + 3\overline{N_e} - \frac{3\overline{N_e}^2}{n}\Big) - \sigma^4\Big)\ \text{ with} \\
\sigma^2 &= np(1-p) = Var(N_e)
\end{aligned} \tag{4.36}$$

where N denotes the total number of events and is assumed to be large.
In the presence of common mode mode noise, the error on mean and variance can be found using Gaussian approximation and are given by,

$$\begin{aligned}
\sigma^2_{\overline{N_e}} &= \frac{\sigma^2}{N} \\
\sigma^2_{Var(N_e)} &= \frac{2\sigma^4}{N}\ \text{ with} \\
\sigma^2 &= \langle {N_e}^2 \rangle - \langle N_e \rangle^2 = Var(N_e)
\end{aligned} \tag{4.37}$$

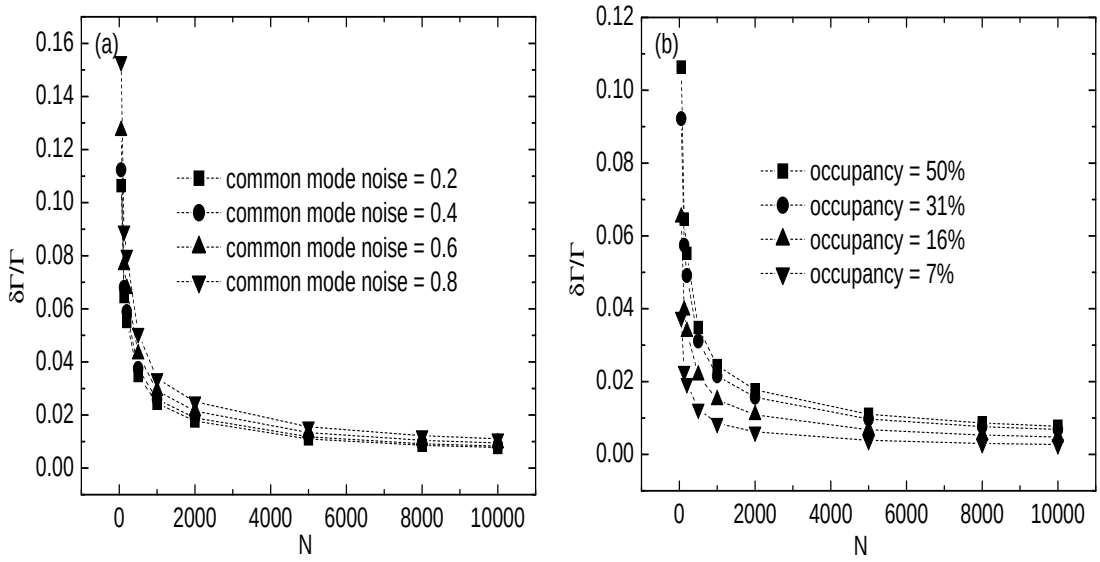

Figure 4.7: (a) Relative error on Γ versus number of events per run for simulation data at different common mode noise levels. In this plot the threshold is set to 50% occupancy. (b) Relative error on Γ versus number of events. Different curves correspond to different occupancy, with common mode noise fixed to 0.2. $\delta\Gamma$ is calculated using Eq. 4.38.

The error on Γ can be found by propagating the error on Γ^2 by,

$$\sigma_\Gamma = \frac{1}{2\Gamma}\sigma_{\Gamma^2} \tag{4.38}$$

Finally the error in the measurement of common mode noise using Eqs. 4.34-4.38 is given by,

$$\sigma_{CMN} = \frac{a}{\sqrt{N}} \times \frac{2\pi\sigma}{2n(n-1)\Gamma} \times \left\{ \frac{\cos(\tilde{\alpha})}{\Big(1-\sin(\tilde{\alpha})\Big)^2} \right\} \times \left\{ \Big(\frac{2\overline{N_e}}{n} - 1\Big)^2 + 2\sigma^2 \right\}^{\frac{1}{2}} \text{ with}$$

$$a = \frac{1}{\Big(1 - 4 \times \Big(|0.5 - Occupancy|\Big)^{2.15}\Big)} \tag{4.39}$$

4.5 Γ Dependence on the Number of Events per Run

Γ is calculated for samples with different number of simulated events and various values of common mode noise. As one can expect for lower number of events

Method	specific to coherence	sensitive to common mode non-Gaussian	sensitive to common mode Gaussian	range of coherence
excess noise	no	no	no	no
$\log(occ.)vs.thresh.^2$	no	yes	no	no
raw data plot	yes	yes	yes	yes
occupancy per event	yes	yes	yes	no
correlation matrix	yes	yes	yes	yes
autocorrelation	yes	yes	yes	yes

Table 4.1: Comparison of the methods.

per run Γ shows larger statistical uncertainties which flatten for large numbers of events per run. Fig. 4.7 (a) shows the relative error on Γ when many data samples with N events are simulated. Different curves correspond to different values of common mode noise. Fig. 4.7 (b) shows the relative error on Γ vs number of events for different occupancies, while the common mode noise is fixed at 0.2. This analysis shows that at least 500 events per run are needed for the relative error to be less than 5%.

4.6 Comparison and Conclusions

Table 4.1 summarises the features of the different methods considered in this chapter. As the first two methods are not specific to coherence, they are only useful if there is huge extra noise in the system or if this extra noise is non-Gaussian. For a basic understanding of the data quality, the raw data plot is very useful and provides qualitative information on coherent effects. The observable Γ, derived from the standard deviation of the number of hits per event, yields a quantitative estimate of the common mode noise and is computationally fairly simple to achieve, given that the normal diagnostics for a binary system include occupancy statistics in any case. It is very sensitive and specific to the coherence of common mode noise. The correlation matrix provides in addition detailed information about the range of coherent effects, as well as the strength of the correlation for each pair of channels. Similar information is obtained by the autocorrelation method.
A method to calculate common mode noise from the observable Γ at arbitrary occupancy is given. A parametrization for Γ as a function of occupancy and common mode noise is given which fits the numerical simulation within $\pm 2\%$ over a wide range of occupancy and common mode noise values.
The statistical uncertainty of Γ has been analyzed. Typically, data should contain at least 500 events in order to obtain a Γ value and there-by a common mode noise estimate with less than 5% statistical uncertainty.

In large silicon micro-strip detector systems like the ATLAS SCT, which are currently under construction, noise analysis has to deal with many thousands of detector modules and several millions of channels. Here it should be useful to quantify coherent noise on the module level by a single number, for instance the Γ variable, which will allow to survey all modules and identify problematic areas. Noise which is coherent between modules and bigger parts of the system can be assessed by combining channels into bigger units like chips or modules and using the number of hits in these units as input for the raw data plot or the correlation matrix.
The methods described in this chapter have been applied to the ATLAS semiconductor tracker (SCT) modules which will be discussed in the next chapter.

Chapter 5

Common Mode Noise Measurement on ATLAS SCT Modules

Methods for the measurements of common mode noise in binary read-out systems have been developed as described in the previous chapter. In the present chapter these methods are applied to ATLAS SCT silicon micro-strip detector modules. These modules are using binary readout scheme i.e signals are compared to a threshold and converted to binary information on the front end chip and therefore provide a good case for application of the common mode methods.
The electrical setup used for common mode noise measurement will be described briefly in the next section, followed by the results obtained with prototype modules.

5.1 Overview of the Measurement Setup

The SCT End-Cap will be covered by three kinds of modules; inner, middle and outer as described in chapter 2. These modules differ in the silicon detector dimensions. Outer and middle modules are made of two single sided silicon detectors on each side with active length of 12.11 cm and 11.7 cm respectively. Inner modules are formed with a single wafer of 6.1 cm on each side of the module. All three kinds of modules use the same hybrid and binary electronic chips.
Methods for the measurement of common mode noise described in chapter 4 have been applied to several Atlas SCT End-Cap modules. The results for one of the modules are presented here though similar results were obtained using the others. The modules were measured in the standard electrical tests setup at Freiburg.

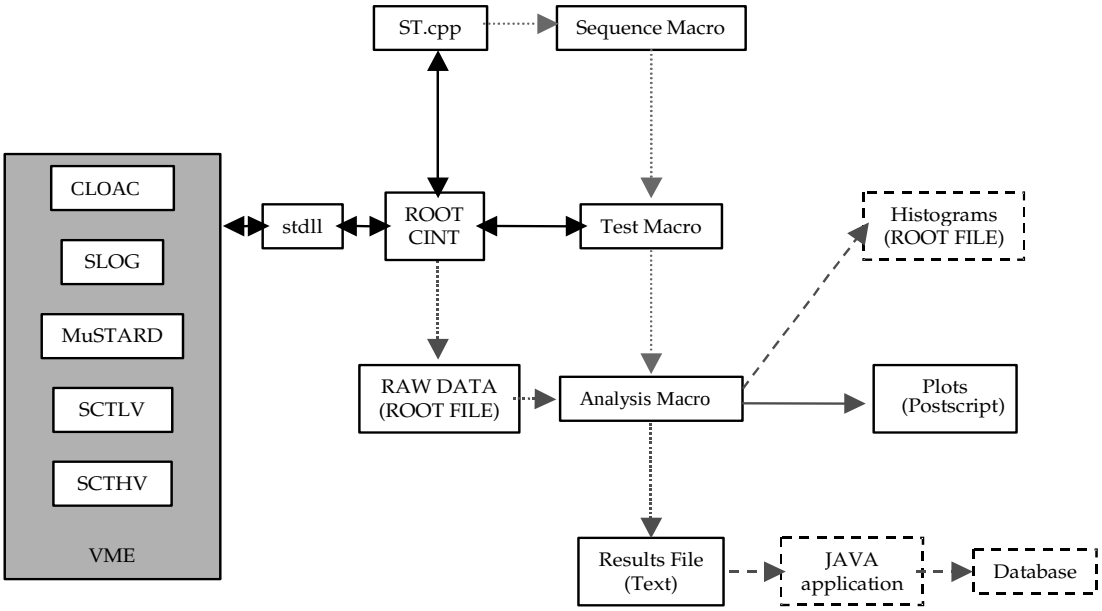

Figure 5.1: Schematics of SCTDAQ system.

Fig. 5.1 shows an overview of the VME[1] modules plus software used in the data acquisition. These are standard components used by the SCT community to verify the hybrid and module functionality. A brief description of these VME modules will be given here, where a more detailed description can be found in the corresponding references.

5.1.1 MuSTARD

The acronym MuSTARD [59] stands for Multi-channel Semiconductor Tracker ABCD Read-out. The purpose of the device is to receive, store and decode data from the modules. It can read out data from twelve data streams or six modules (each detector module produces two data streams, one for each side of the module).
The decoded data is used to fill internal histograms, allowing the system to accumulate the data resulting from a burst of triggers. When a burst is finished, the DAQ program running on the PC reads out the histograms.

[1]VME stands for VERSA Module Eurocard. A VME crate can hold several electronics modules and provides a standardised communication bus.

5.1.2 CLOAC

The CLOAC [60] stands for CLOck And Command. It generates the system clock of 40 MHz. It also generates fast commands such as L1A and reset commands for the SCT modules, in the absence of Timing, Trigger and Control system.
The CLOAC can be synchronised to an external clock and can use an external trigger signal.
The measurements described in this chapter do not use the CLOAC module. The clock is generated by a SLOG (see below) module in the Freiburg electrical test setup.

5.1.3 SLOG

The SLOG [61] stands for SLOw command Generator. It allows the generation of slow commands which are longer than 7 bits for the control and configuration of ATLAS SCT Front-End chips. It receives clock and fast commands from the CLOAC, and fans them out to up to 12 detector modules. In the Freiburg test setup the SLOG is used in stand-alone mode. An internal 40 MHz clock is selected, allowing SLOG to generate clock and commands.

5.1.4 SCTLV

The SCTLV [62] module provides low voltage power for the digital and analogue part of the chips (Vdd and Vcc). Each SCTLV module can provide low voltage power for two detector modules and reads out the thermistors mounted on the SCT modules.

5.1.5 SCTHV

The SCTHV [63] module provides detector bias for four detector modules at up to 500 V and a maximum current of 5 mA. The absolute over-current limit protection is at the 5.2 mA.

5.2 Software

SCTDAQ [64] is the data-acquisition software used together with the ROOT histogramming and analysis package [49]. Fig. 5.1 shows an overview of the SCTDAQ. The System Test Dynamic Link Library (STDLL) can store the required settings of a module and the way that module is connected to the system, by reading the system and module configuration files. It is dynamically linked to ROOT, and its functions and classes are made available in CINT, the ROOT

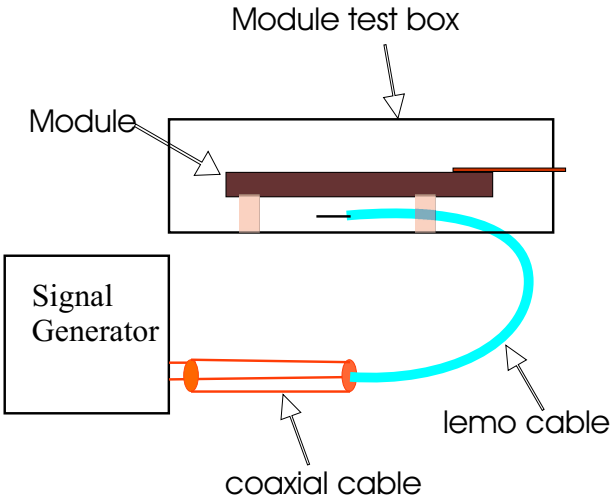

Figure 5.2: An overview of the set-up used for noise injection.

C++ interpreter.
The system is started by running an interpreted macro that calls upon the functions of the shared library to initialise the VME boards and to configure the SCT detector modules to their default conditions. A set of standard test macros allows more sophisticated control of the hardware. The system can be controlled either interactively via macro or via the graphical push-button SCTDAQ menu-bar. The test macros also make use of the analysis macros, which analyse the histograms and produce three types of output files: the basic histograms (stored in ROOT histogram files), the plots (stored in postscript form) and summary data in the form of ASCII files, which can be uploaded to the SCT-database [65] using Java script. For the common mode analysis some additional macros were written to analyse the data.

5.3 Application of Methods to ATLAS SCT End-Cap Modules

For common mode noise measurements the End-Cap prototype modules are tested in a Freiburg test box, which provides mechanical support as well as cooling. The hybrid substrate (GND) is electrically connected to the cooling box and the box is flushed with Nitrogen. The module is cooled with silicone oil as coolant provided by a Julabo FP50 chiller. The results presented in this chapter for inner module E03 are obtained at 15°C chiller temperature, which corresponds to 35°C as measured by the hybrid thermistor. All measurements are performed biasing the module at 100 V. Only the common mode noise results for module E03 are

described in this chapter, the complete electrical characterization results can be found in [66].
The coherent noise effects in the test system are small. In this test common mode noise was created by injecting a 10 MHz signal of amplitude 0.5 V. The signal injection was done in a straight forward way by putting the output cable from the signal pulse generator underneath the module inside the module box. The cable acts as an antenna emitting a radio frequency. An overview of the set-up is shown in Fig. 5.2. In this way the extra signal injected is not necessarily all common mode but we see a significant amount after injection. Results with and without the signal injection will be compared to see the difference and usefulness of the common mode noise methods described in the previous chapter.

5.3.1 $\log(occupancy)$ *vs.* $(threshold)^2$

A scan of noise occupancy as a function of threshold was performed as shown in Fig. 5.3 without noise injection. The log of noise occupancy as a function of threshold squared is linear and agrees very well with the assumption of Gaussian noise as described in section 4.3 in the previous chapter.
Fig. 5.4 shows the same plot in the presence of injected noise. The extra noise changes the slope of the line but does not lead to a specific feature in this plot. This plot is mainly sensitive to non-Gaussian noise contribution.

5.3.2 Raw Data Plot for Module E03

SCT modules are using ABCD3T [32] binary read-out chips. For the binary architecture one of the most critical issues is the uniformity of the parameters of the front-end circuit and especially matching of the discriminator threshold and the gain. The ABCD3T implements an individual threshold correction in every channel using a 4-bit DAC (trim DAC) per channel with four selectable ranges. The module E03 is properly trimmed before performing the measurements presented here in order to minimize the impact of threshold non-uniformity.
The hit maps for the front and back sides of module E03 at 50% occupancy, without and with extra noise injection are shown in Fig. 5.5 and 5.6. Common mode noise which can be seen in the form of horizontal bands in the hit map is very small in Fig 5.5 and is clearly visible in particular on the back side of the module in Fig 5.6.
The extra noise is injected from a cable underneath the module, therefore common mode noise is expected to be more pronounced on the back side as compared to the front side of the module. As mentioned in the previous chapter this plot does not give any quantitative information but it is a very useful diagnostic tool.

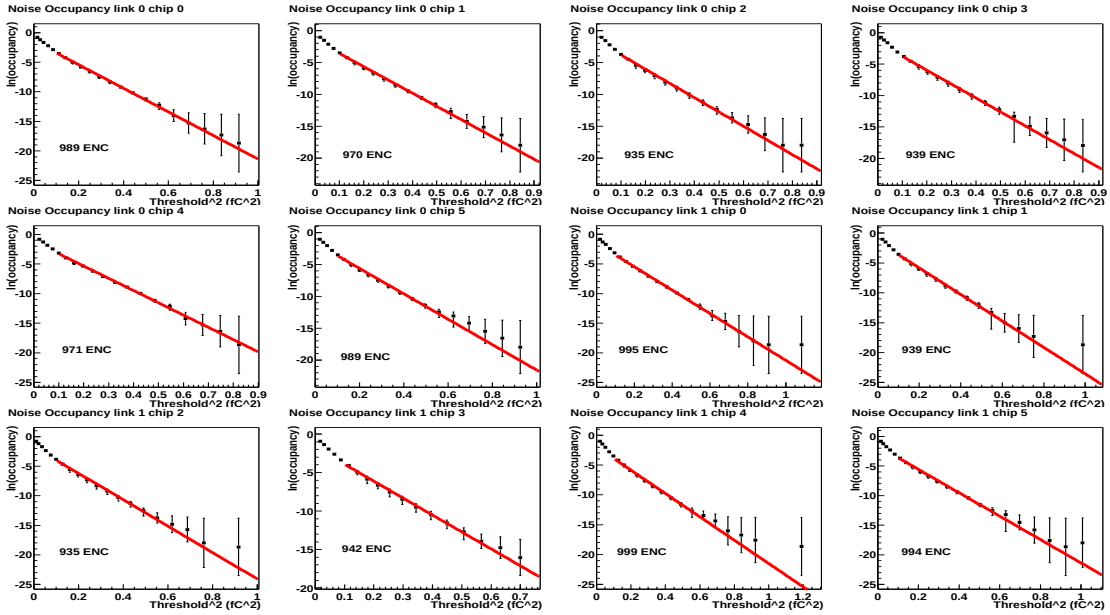

Figure 5.3: Log of noise occupancy as a function of threshold squared (fC^2) for the 12 chips on module E03 measured in the Freiburg electrical test setup. The noise is given for each chip.

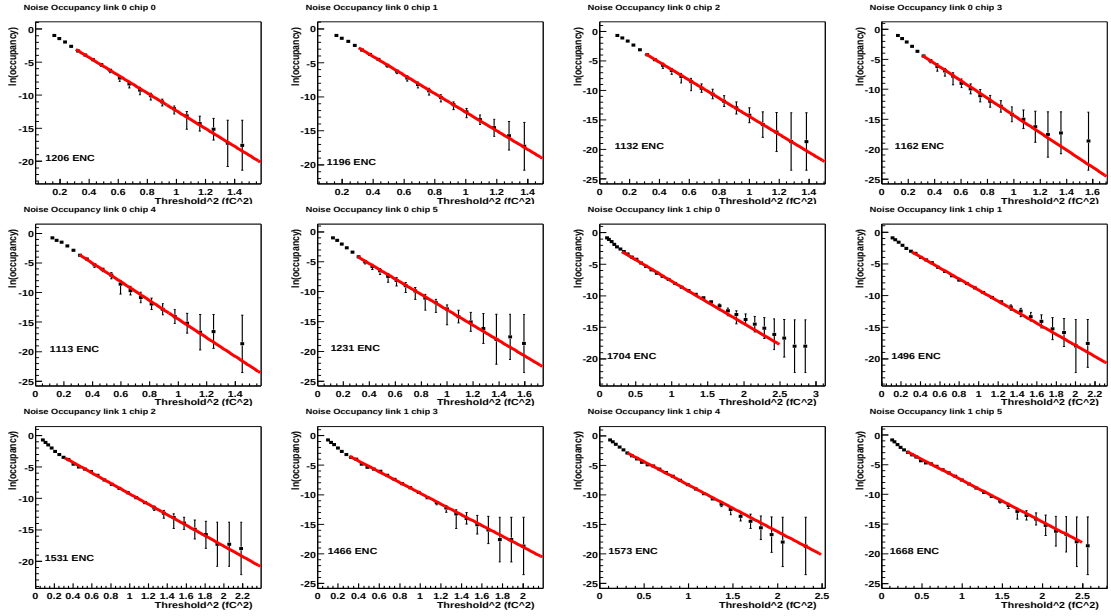

Figure 5.4: Log of noise occupancy as a function of threshold squared (fC^2) for the 12 chips on module E03 measured in the Freiburg electrical test setup with extra noise due to noise injected.

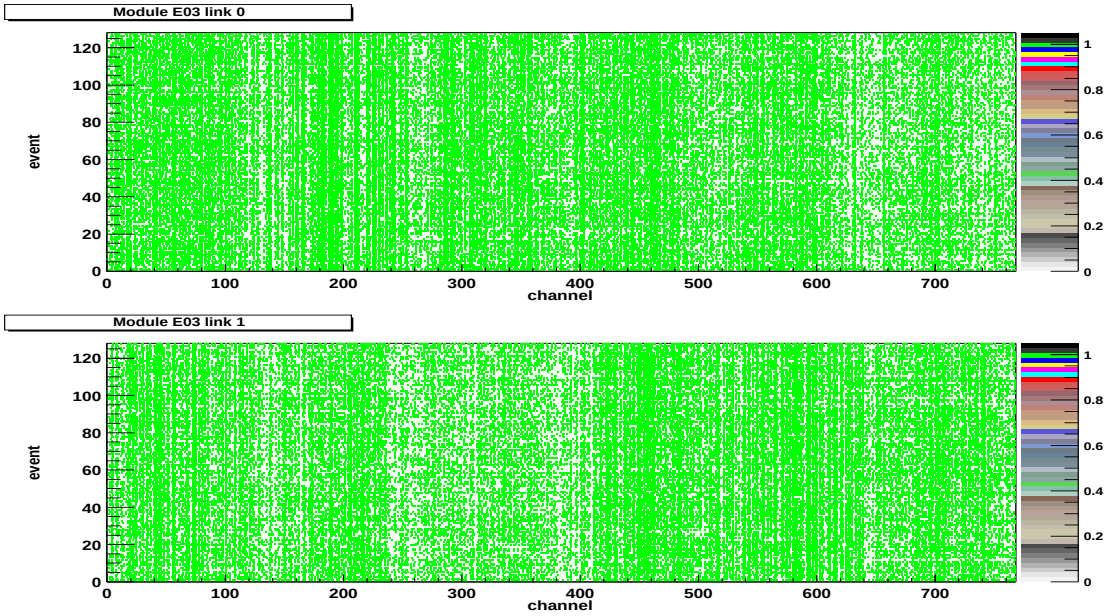

Figure 5.5: Hit map for front and back side of module E03 at 50% noise occupancy without noise injection.

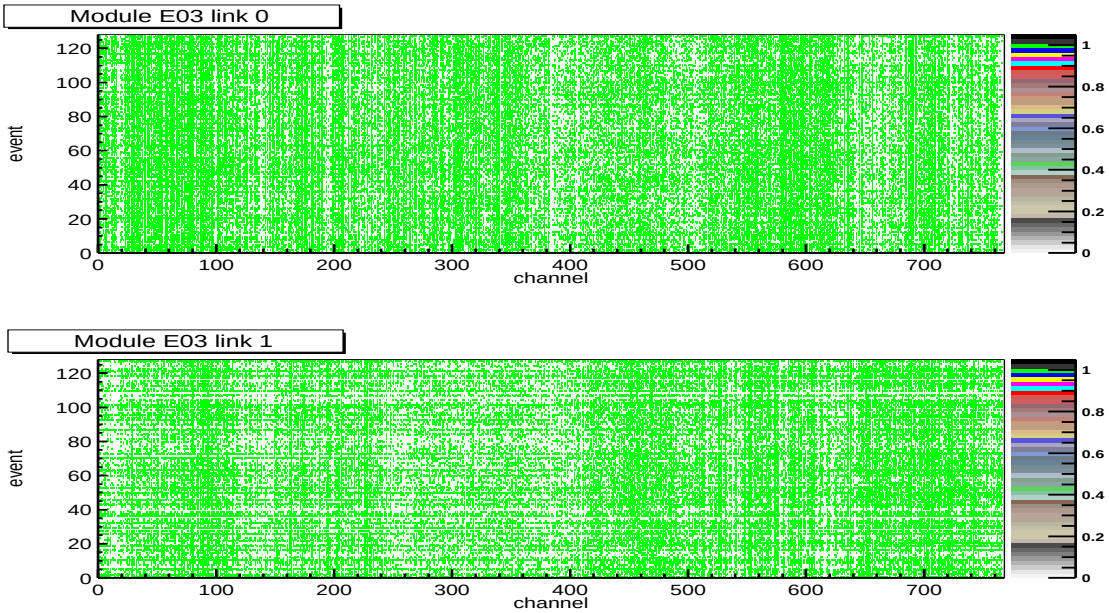

Figure 5.6: Hit map for front and back side of the module E03 at 50% noise occupancy with extra noise injected as described in the text.

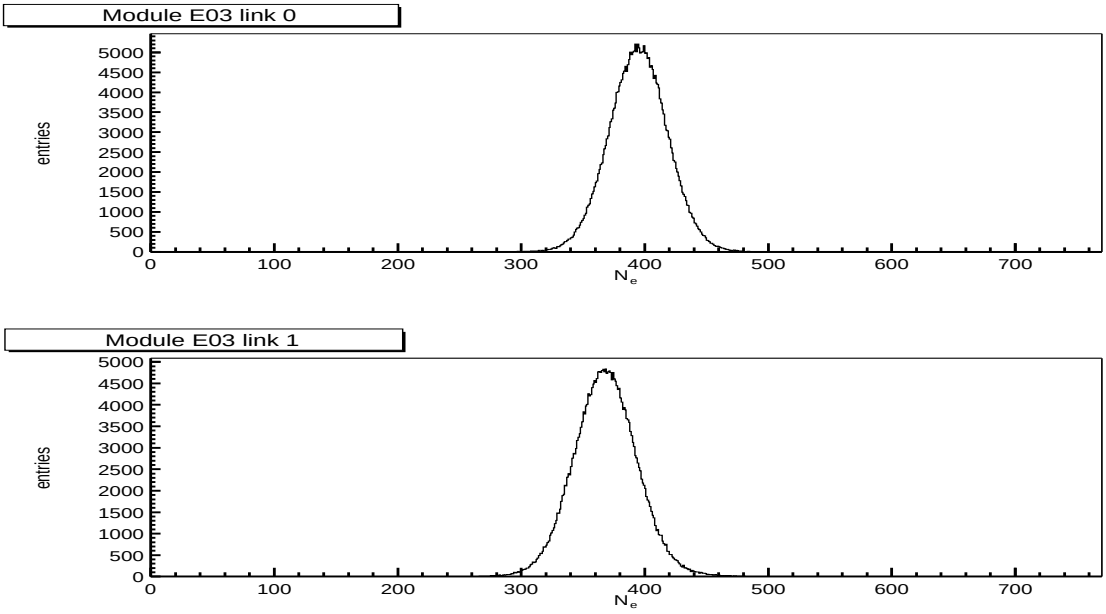

Figure 5.7: Distribution of occupancy per event for front and back side of the module E03. No noise injected here.

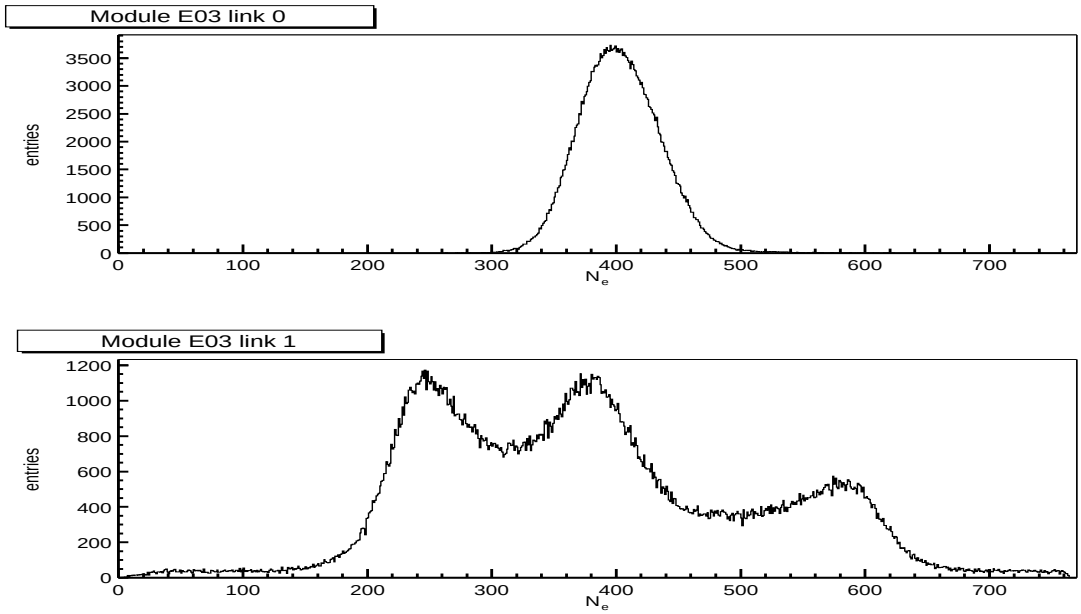

Figure 5.8: Distribution of occupancy per event for front and back side of module E03 with extra noise injected.

5.3.3 Occupancy per Event

The occupancy per event for the front and back side of module E03 at 50% occupancy is shown in Fig. 5.7. In the absence of injected noise the distribution is Gaussian for both front and back side of the module. The plot is based on a sample of 300 000 events. The Gaussian fit gives a standard deviation of 23.65 and 25.32 on the front and backside of the module respectively. The standard deviation is roughly twice the expected standard deviation (13.85) using binomial statistics. The effect of extra common mode noise on these distributions can be seen in Fig 5.8, which is measured when injecting extra noise. Due to more coherent noise on the back side, the distribution of occupancy per event is wider than on the front side of the module. The peaks on the back side of the module in Fig 5.8 show that, common mode noise is not uniform across all chips. This is also clear in Fig. 5.6. In addition the occupancy varies slightly from chip to chip. The distributions of occupancy per event for all chips without and with extra noise injection are shown in Fig. 5.9 and 5.10. In the presence of more coherent noise, the difference in the distributions of occupancy per event among chips can be seen. Under the influence of coherent noise, the occupancy per event distribution no longer follows binomial statistics, therefore, the observable Γ has to be used to measure the common mode noise contribution.

5.3.4 Correlation Matrix

The correlation matrix obtained for all 12 chips with noise injection is shown in Fig. 5.11. Higher correlation among the chips is visible on the back side of the module due to the higher level of coherent noise.

5.4 Common Mode Noise Measurement from the Observable Γ

To quantify the amount of common mode noise present in the system, the Γ method described in section 4.4 of chapter 4 has been applied to Atlas SCT End-Cap modules. Eq. 4.34 predicts how the common mode noise σ_C normalized to random noise σ_R varies with the measured Γ and occupancy. However, intrinsic random noise will generally be unknown, as only the total noise σ_T, containing random and common mode noise sources can be measured. Since the common mode noise adds in quadrature to random noise, therefore using Eq. 4.34 and $\sigma_T^2 = \sigma_C^2 + \sigma_R^2$, we get,

$$\sigma_C^2 = \frac{\sigma_T^2 \cdot a^2 \cdot \Gamma^2}{1 + a^2 \cdot \Gamma^2} \quad \text{with}$$

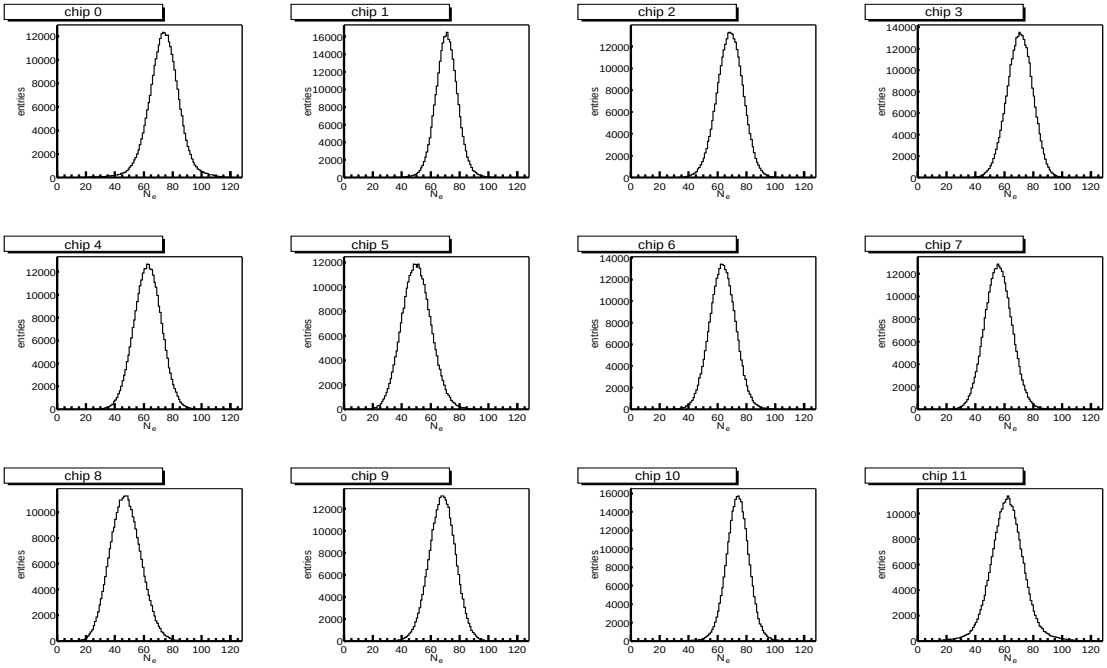

Figure 5.9: Distribution of number of hits per event without noise injection for all chips of module E03.

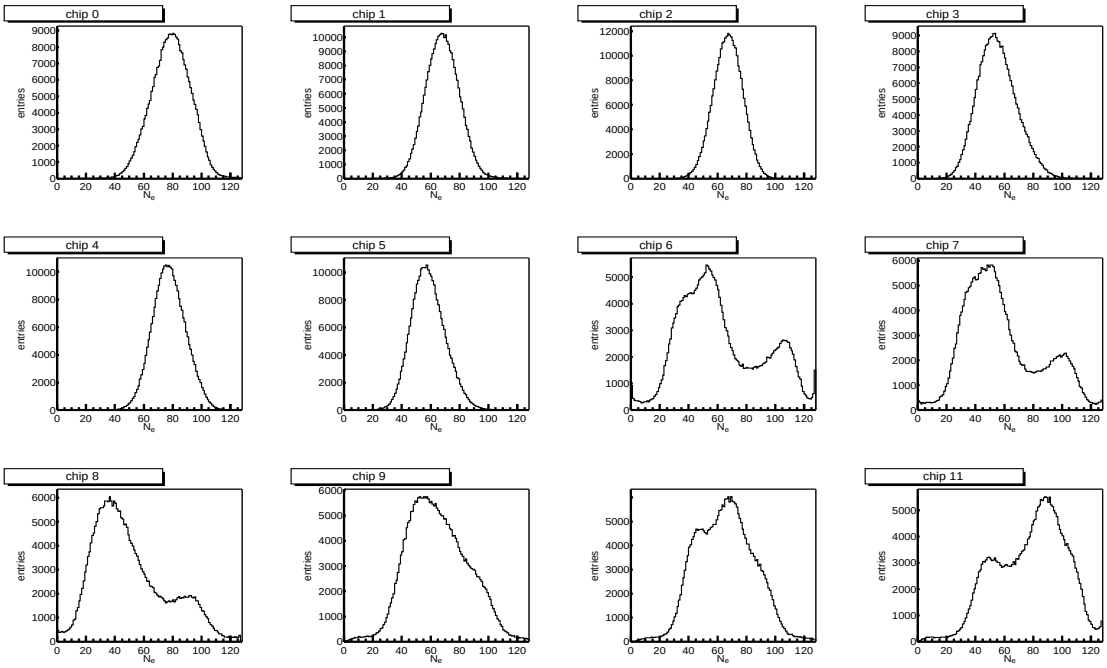

Figure 5.10: Distribution of number of hits per event with noise injection for all chips of module E03.

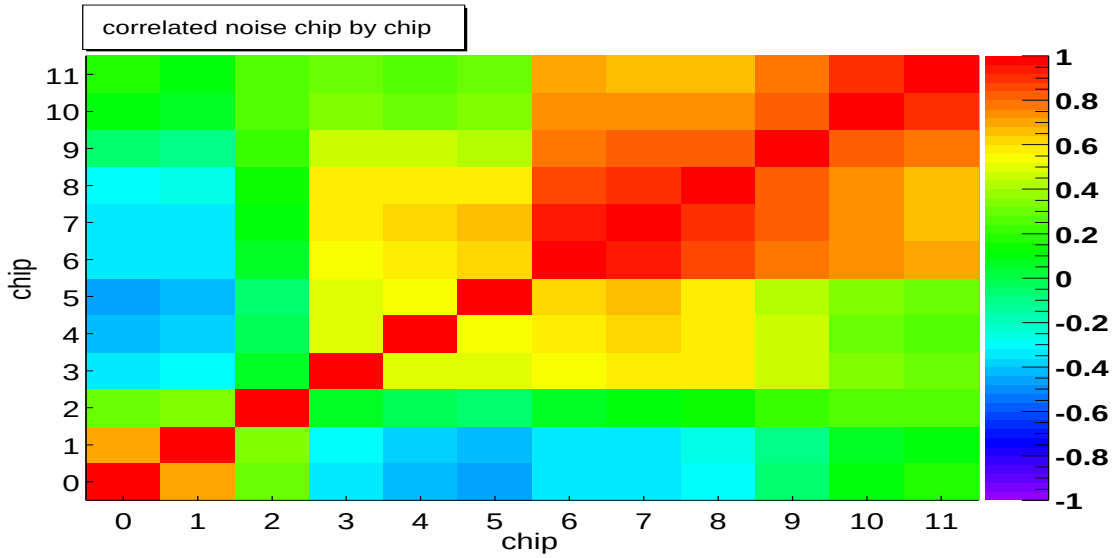

Figure 5.11: Correlation matrix chip by chip. The scale shows the amount of correlation.

$$a = \frac{1}{\left(1 - 4 \times \left(|0.5 - Occupancy|\right)^{2.15}\right)} \tag{5.1}$$

The common mode noise contribution can be calculated from the measured Γ at a given occupancy (threshold) and total noise σ_T using Eq. 5.1, where the total noise σ_T is measured from the S-curve[2] for every channel of each of the twelve chips and the results averaged by chip.

The common mode noise calculated for each chip of the module E03 at a threshold corresponding to 50% occupancy, is shown in Fig. 5.12 (a). The data sample contains 300000 events, errors on the measurement of common mode noise are smaller than markers. The relative contribution of common mode noise to the total noise is small because it adds in quadrature to random noise. Fig. 5.12 (b) shows the average common mode noise on the module as a function of occupancy. To generate this plot the threshold is varied in 0.025 fC steps. The common mode noise is decreasing with increase in occupancy both for the front and backsides of module. To understand this effect a simulation result for common mode noise contribution of 155 electrons is also shown in Fig. 5.12 (b). It is clear that simulation result is independent of occupancy and therefore this special feature must come from the module.

The common mode noise by chip in the presence of extra noise due to noise injection is shown in Fig. 5.13 (a). Due to high coherent noise on the back side of the module the common mode contribution is high. Here again one can see, the

[2]S-curve is the plot of number of hits as a function of threshold.

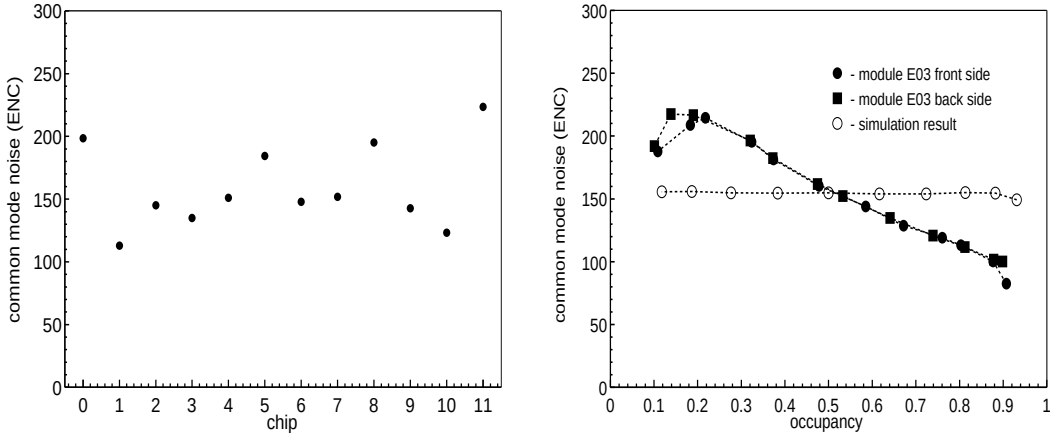

(a) (b)

Figure 5.12: (a) Common mode noise by chip for module E03 using Eq. 4.34 for measured values of Γ and Occupancy. (b) Common mode noise as a function of occupancy for the front and backsides of module E03 without noise injection.

common mode noise varies from chip to chip and might be a reason of peaks on the back side of the module in Fig. 5.8, as discussed in subsection 5.3.3. Fig. 5.13 (b) shows the average common mode noise for the module as a function of occupancy. There is around 100 electron decrease in common mode noise with increase in occupancy from 10% to 90%.

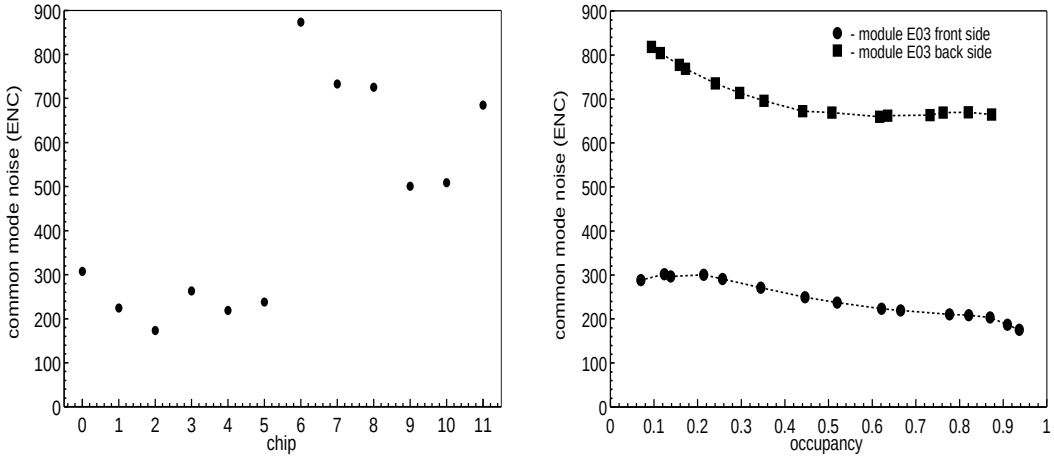

(a) (b)

Figure 5.13: (a) Common mode noise by chip for module E03 for measured values of Γ and Occupancy. (b) Common mode noise as a function of occupancy for the front and backsides of module E03 with noise injection.

5.5 Conclusions

Common mode noise in a system where the data is read out using a binary scheme can be measured in several ways as described in previous chapter. Those methods are successfully applied to measure the common mode noise contribution in ATLAS SCT modules. The common mode noise contribution on the prequalification modules equipped with ABCD3T chips is small. Extra noise was injected to verify all common mode noise methods. To quantify the common mode noise contribution the Gamma method is found giving the best results.

Chapter 6

SCT Simulation and Reconstruction

Monte Carlo simulation techniques are widely used in High Energy Physics in order to compare theoretical models to the experimental results and to make studies of the potential of a physics experiment. Simulations are also important during the detector design phase to develop a detector with optimal discovery potential. The most sophisticated simulations are full Monte Carlo studies which track individual particles through a detailed description of the detector geometry. There are several factors that can degrade the detector performance. In this chapter the effects of increased SCT noise and inefficiency on single track reconstruction efficiency of the ATLAS Inner detector is presented.

6.1 SCT Simulation Flow

The ATLAS Inner detector simulation under Athena framework [67] consists of several steps as shown in Fig. 6.1. The first step of simulation is the hit data creation. As shown in the diagram there are two ways to get hit data under Athena. One way is to read hits from the Zebra files. This can be done using data converters. The Zebra files are generated using the Geant3 simulation for Data Challenge 1 (DC1[1]) [68].
The second way is to generate hit data using GEANT4 [70]. Both methods are used in this chapter to generate hit data for the SCT.

[1]ATLAS computing planned a series of Data Challenges in order to validate its Computing Model, its software, its data model, and to ensure the correctness of the technical choices to be made. The purpose of DC1 was to generate several data sets for high-level trigger studies and for physics analysis.

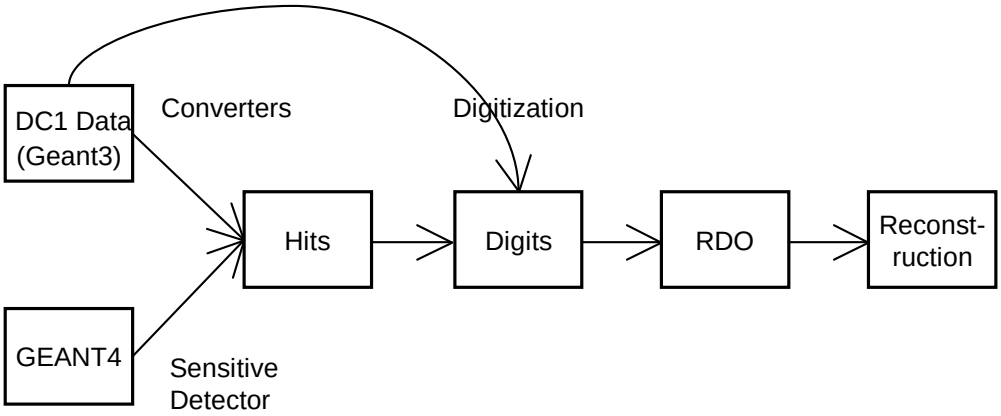

Figure 6.1: Simulation flow diagram under Athena framework.

6.1.1 Hits

The simulation of hit data has to start with a description of the detector geometry. The SCT geometry is described in FADS/Goofy [71] and is available under Athena since release 6. The geometry parameters are taken from the Nova database. A particle passing through the geometry undergoes different physics processes. At this stage Geant4 takes care of the passage of particles through the SCT. The most important physics processes simulated for the Inner Detector are multiple scattering, continuous energy loss, bremsstrahlung for electrons, conversions for photons and nuclear interactions for hadrons. The particle passing through the SCT deposits energy in the silicon and produces a hit. A hit in GEANT4 is a snapshot of the physical interaction of a track in the active volume of a detector. The hit produced in the silicon trackers is characterized by two three dimensional positions inside the silicon sensors (start and end position), a deposited energy, a time of deposition, and a track number corresponding to the particle which produced the hit by interacting with silicon.

6.1.2 Digits

The second part of the simulation is to convert hits produced by GEANT4 into digits. For each sub-detector there is a model of how the ionization in the active detector element is changed into the digital output of the readout electronics. This step is called the digitization phase. The output from digitization corresponds to the real life silicon module output, obtained by using binary electronics. The digit is mainly characterized by a readout cell, within one of the electronic circuits of the detector element[2], which has recorded a signal above a given threshold. The

[2]For the SCT a detector element is one side of the SCT module

simulation of noisy and dead channels in the electronics is a part of digitization. The inefficiency and extra noise in the SCT is introduced in the digitization phase.

6.1.3 RDO and Reconstruction

The output from the digitization is the so called Raw Data Object (RDO). This is the format which the reconstruction package needs as input. There exist algorithms in the ATLAS cvs [69] repository to read RDOs and fill a ROOT ntuple(tree [49]). The author of this thesis provided such an algorithm for the SCT and this algorithm is now in the cvs repository and forms part of the ATLAS software release. The last step is to run reconstruction on RDOs. The reconstruction in a detector simulation involves the reconstruction of the kinematic information and particle identification. For the Inner Detector tracks are reconstructed from the hits in the individual detector elements. The standard reconstruction packages xKalman++ [72] and iPatRec [73] are used. Reconstruction results only from iPatRec will be presented in this chapter.

6.2 Software Tools

The ATLAS offline software is composed of a set of packages running under the Athena framework. The programs are written in object oriented C++ and perform various simulation tasks as described in the previous section. The software tools used to obtain the results presented in this chapter are described below. The Athena framework is described in the next subsection and a summary of the relevant software is given in the following subsections.

6.2.1 Athena Framework

Athena is a framework, which is a specific ATLAS implementation of an underlying GAUDI [74] architecture. The GAUDI architecture originally developed by the LHCb experiment has been extended through collaboration with ATLAS. The overall principle of the framework is the separation of algorithms and data. The Athena-Gaudi object diagram is shown in Fig. 6.2. The most important Athena components are:

- Algorithms: the basic building blocks of user applications, generally accept input data, manipulate it in some way, and generate new output data. An algorithm inherits from the framework algorithm abstract class and contains three methods, initialize() which is executed at the start of the job, execute()

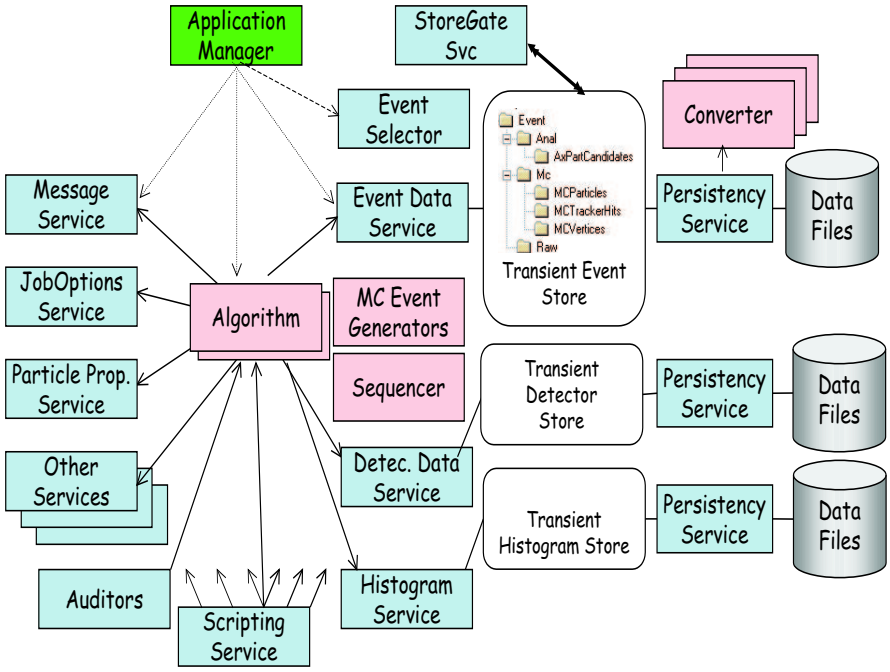

Figure 6.2: Athena Object diagram.

which is executed for every event and a finalize() which is executed at the end of the job.

- Data Object: produced/accessed by algorithms, acting as their input and output.

- Transient Data Stores (TDS): There exist several transient stores acting as temporary repository for data objects. The idea is to reduce the coupling between algorithms. Thus, an algorithm will locate input information from a TDS, and write out newly generated information derived from its processing into the TDS again, where it can be later retrieved by downstream algorithms. The various transient stores are:

- Event Data Store (TES)

- Detector Data Store

- Histogram and Ntuple Store

- Services: provide specific capabilities of the framework e.g Histogram Service, Persistency Service, Random Number Generator Service. Services hide behind abstract interfaces, the specific implementation is selectable at run

time. The different persistency services provide the functionality needed to populate the Transient Data Stores from persistent data and vice versa.

- Properties: are adjustable parameters for algorithms and services. They allow run time configuration and they are specified via a text file, or Python script at the startup phase of the application.

- Data Converters: convert Data Objects within the transient stores to and from an equivalent set of persistent objects.

6.2.2 GEANT4

The acronym GEANT [70] comes from GEometry ANd Tracking. GEANT4 is a toolkit for simulating the passage of particles through matter. It provides a complete set of tools for all the domains of detector simulation including geometry, tracking, detector response, physics models, run, event and track management, visualization and user interface. It exploits advanced software engineering techniques and Object Oriented technologies and hence provides the possibility of validating the physics results at the LHC scale.

6.2.3 FADS/Goofy

FADS/Goofy [71] is the development framework for ATLAS simulation based on the GEANT4 toolkit. The name stands for Framework for ATLAS Detector Simulation/GEANT4-based Object-Oriented FollY. FADS/Goofy is a framework and one needs to use the Goofy executable available under the standard installation. It is necessary to plug in user-defined modules (like geometry, sensitive detector, persistency module or magnetic field etc) dynamically to this running framework, which is available under Athena. Simulation results in this chapter are obtained using FADS/Goofy.

6.2.4 SCT Digitization

The simulation of the electronic response of the detector to particles for the SCT is provided by the SCT digitization package. The digitization is the last step of the full simulation of a detector. The output from digitization is similar to that which is expected from the readout electronics. The output are the so called RDOs. A RDO contains a pair of numbers: a strip number and a length of the cluster above threshold. The RDO will also be used for real data.
The SCT digitization package consists of five classes. It is available under Athena and is described in detail in [75] and [77] respectively. The SCT digitization works

as a part of the digitization scheme implemented in the SiDigitization package [76]. The latest developments and status can be found in [78].

6.2.5 iPatRec and xKalman++

The final stage is to convert the digitization output into physical quantities such as energies, momenta etc. The two pattern recognition programs used are iPatRec and xKalman++.
The xKalman++ pattern recognition starts the pattern recognition in the TRT using a histogramming method. This method takes advantage of the many hits on each track in the TRT to find tracks as spikes in a 2-dimensional (φ,$1/p_T$) distribution. From each track candidate found in the TRT a Kalman filtering method [79] is used to propagate the track candidate parameters through the silicon detectors, layer by layer towards the primary vertex. Each track reconstructed in the precision layers is then extrapolated back into the TRT and the drift-time information of the straw hits are used in the fit.
The iPatRec algorithm takes advantage of the low occupancy in the outermost layers of the silicon detectors. Reconstruction is performed in roads which join the vertex region to a seed region defined on the outer surface of the inner detector. A list of modules in the road is created. The digital information in these modules is decoded, locally clustered and space-points are built from pixel-clusters and stereo strip-intersections within the same layer. After forming clusters and space points, track finding proceeds by building a track candidate in a combinatorial search through space points from the silicon detector, and then adding pixel hits. Track quality is assessed at each stage of the build by applying quality cuts on the number of silicon detector hits and the χ^2 of the track. The TRT hits are included in the final stage of the track fit by a histogramming method in a narrow road around the reconstructed helix of the track. More details can be found in [73] and [20].

6.3 Hits Creation in the SCT

The first step of the full simulation of a detector is simulating the response of the active (sensitive) part of the detector. To show the response of a charged particle in the SCT as implemented in FADS/Goofy, random straight tracks are generated at the vertex as shown in Fig. 6.3. For 200 GeV muons there is not much bending in the magnetic field because of the muons high energy. Muons passing through the sensors deposit energy in silicon and create hits as described in section 6.1.1. Each of these hits has an energy following the Landau distribution. Energy distribution both in the Barrel and Endcap parts of the SCT is shown in Fig. 6.4.
The low energy tail is caused by hits produced by secondary tracks. A muon

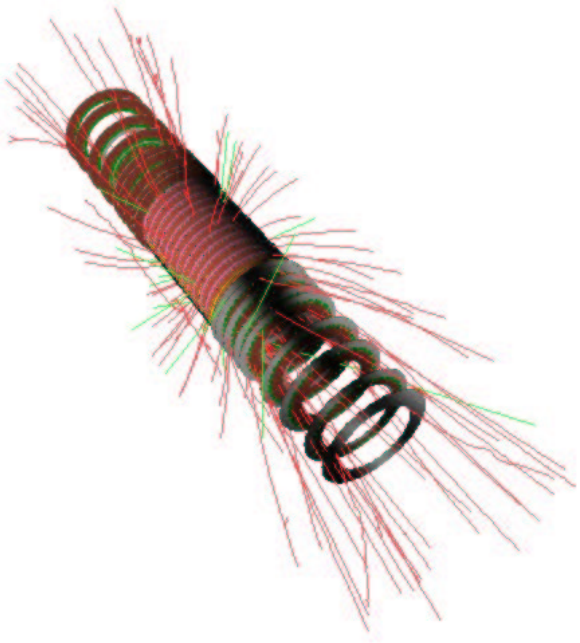

Figure 6.3: SCT geometry in FADS/Goofy with 100 μ^- tracks in the ATLAS magnetic field.

passing through the silicon looses energy by continuous processes like ionization and bremsstrahlung and thus creates a hit. Beside this first hit there exists a small probability to create a delta ray. The energy deposited in delta rays can give rise to a second hit. Therefore there could be two hits due to one parent track in the same sensor. In the digitization phase the charge generated by the second hit is collected into the appropriate strip and therefore we will have a single digit. To understand the low energy tail, the energy deposited by primary and secondary tracks are shown separately in Fig. 6.5. It is visible that mainly secondary hits contribute to the low energy tail. A slight contribution to low energy tail also comes from hits in the overlap region (there is a tilt angle for each module in the barrel SCT and hence two nearby layers have an overlap region).
Hit positions in both barrel and endcap SCT modules are shown in Fig. 6.6. The upper two plots show local hit positions, while the lower plots show hit positions in global coordinates. Local coordinates are measured in the module reference frame for both barrel and endcap parts of the SCT and are shown in plots Fig. 6.6 (a) and (b). Different shapes of the barrel and endcap sensors are visible in the local coordinates plot. The hit global coordinates in X-Y and Y-Z projection are shown in Fig. 6.6. Plot (c) shows the X-Y view of the barrel SCT in global coordinates and (d) plot shows the Y-Z view of the endcap SCT.
The R vs Z plot for the whole SCT is shown in Fig. 6.7. Four Barrel SCT layers

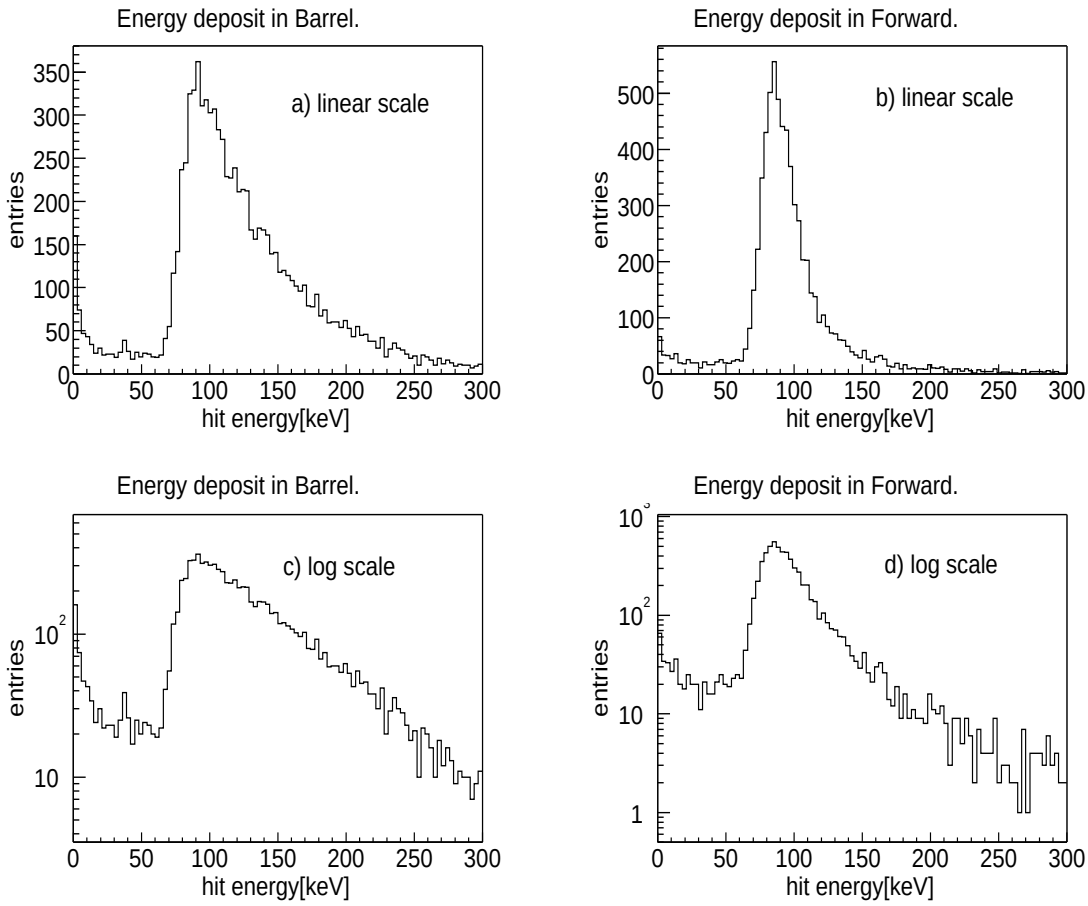

Figure 6.4: Energy deposited by μ^- in (a) Barrel and (b) Forward SCT modules. Plots (c) and (d) are the same as (a) and (b) with log scale.

and 9 disks on both sides are visible. The offset in Z between modules can be seen in the R vs Z plot. In the barrel region there is a tilt angle of 10° for each module and therefore hits can be seen within around 1 cm in the radial direction in the R vs Z plot.

6.4 Digitization

Digitization is the last step of the full simulation of a detector. Its output are the digits, comparable to the raw data produced by the real detector.
For the full simulation of the ATLAS detector, it is assumed that all events are independent. Therefore, digitization of the SCT or Pixel is performed in each event. An event which is to be digitized may include hit information from several

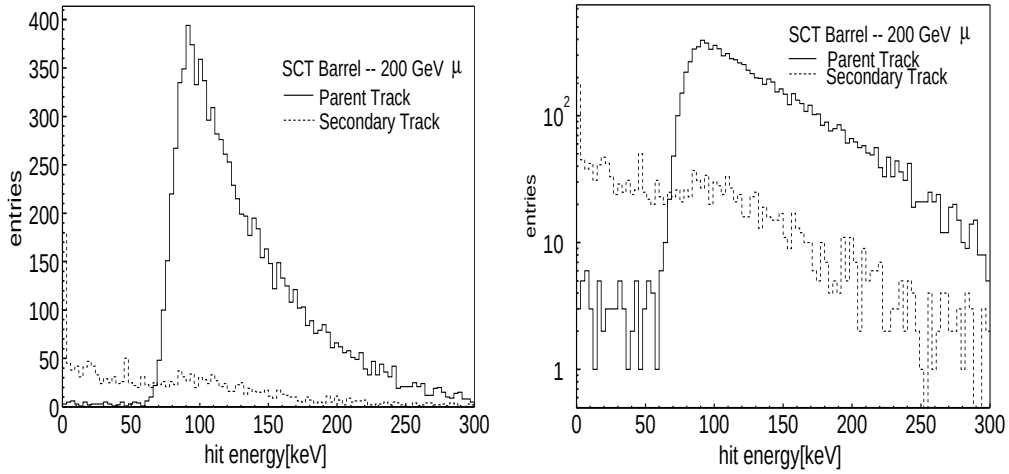

Figure 6.5: Energy deposited in Barrel SCT module on a linear (left) and log scale (right).

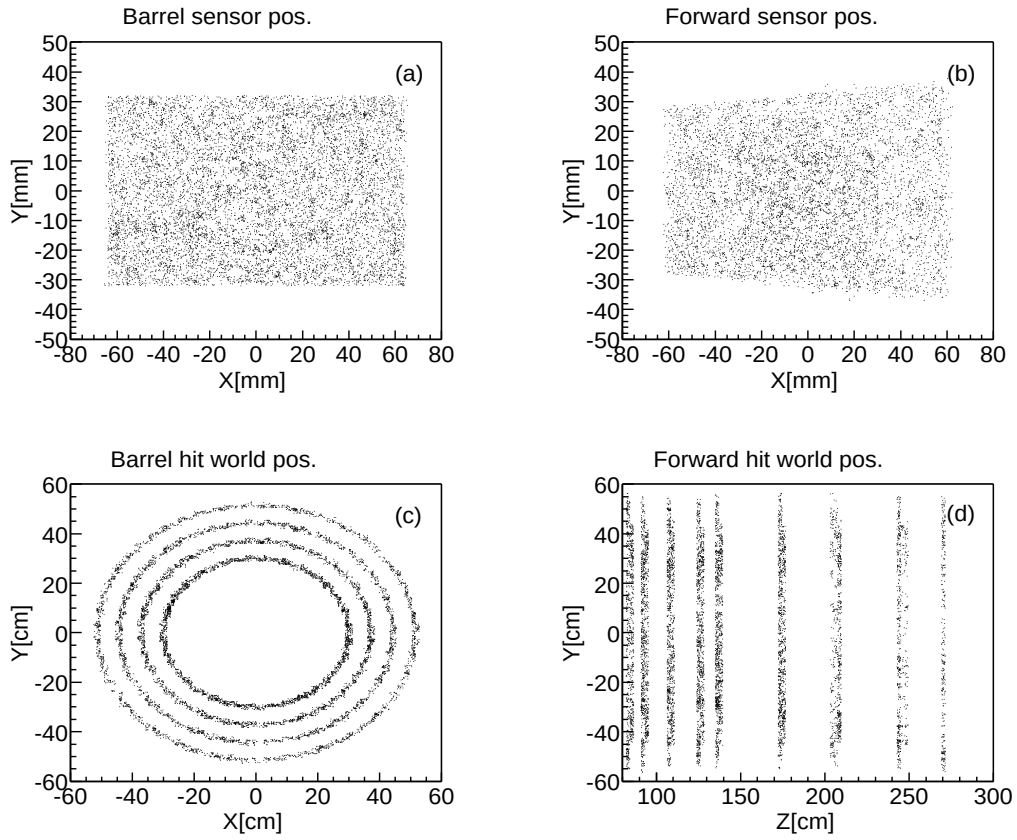

Figure 6.6: Hits in both Barrel and Forward parts of the SCT. See text for details.

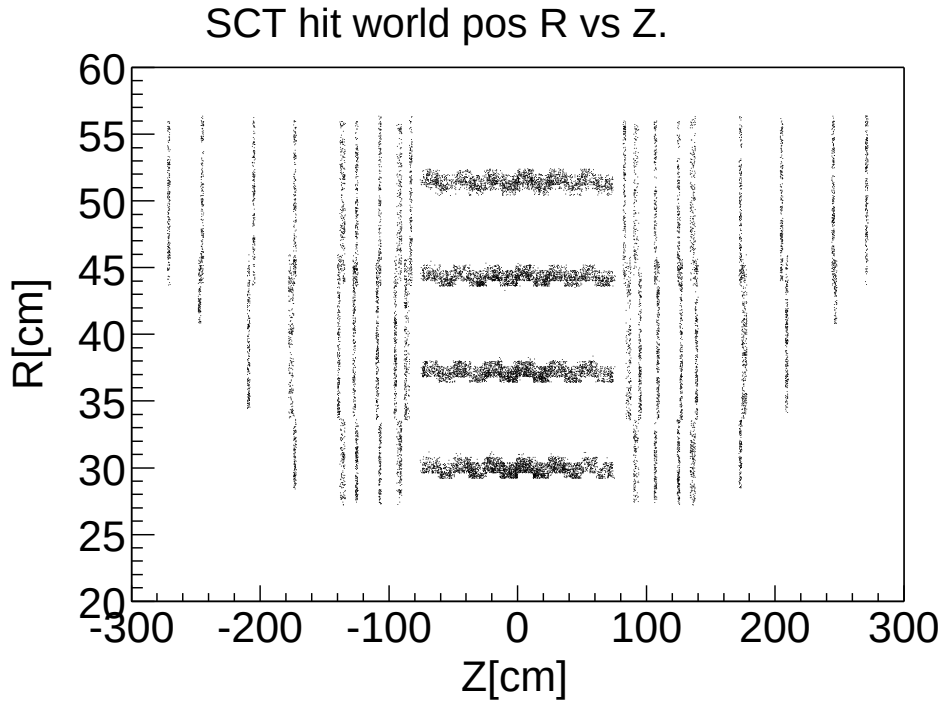

Figure 6.7: R vs Z plot of the SCT.

"piled-up[3]" collisions, depending on the instantaneous luminosity being simulated. The basic detector element defined in the digitization is a full module in the Pixel detector: one silicon sensor and its associated electronics, and one side of a module in the SCT: one or two electrically connected silicon sensors and their associated electronics. All these detector elements are independent, therefore the digitization is performed independently for each detector element. Due to the independence of events and detector elements, a collection of hits or digits contains the hits or digits for a single detector element and a single event.
The creation of simulated digits from simulated hits requires three main steps:

- the deposited energy is converted into a cloud of charges and this cloud is then drifted towards the sensor surface. For silicon modules, 2.76×10^2 electron-holes pairs are created per keV of deposited energy,
- the charges are then assigned to individual strips to create charged diodes. The diode level effects such as cross talk between diodes and leakage current noise etc, are then simulated by processing these charged diodes,

[3]At the LHC design luminosity, there will be an average 23 p-p events superimposed in a single bunch crossing. These events are referred to as pile-up.

- the charged diodes are then connected to the corresponding readout cells. The readout cell level effects such as discrimination, noisy cells generation etc, are implemented here.

For the SCT binary electronics, no pulse-height information will be recorded for firing strips; only the fact that they were above threshold is known. It should be noted as mentioned in section 6.2.4, that the SCT data digits do not correspond to single strips. The ABCD chips cluster the detector data. The smallest unit of the SCT data is in fact a pair of numbers: a strip index and a length of the cluster. In order to have the simulated SCT digits in the same format as the data, the SCT digitization performs clustering of pre-digits[4]. Pre-digits corresponding to neighbouring strips are merged into one pre-digit if they are both above threshold. In the simulation along with the digits, the noise, threshold and inefficiency flags are also stored. In the next subsection the digitization data produced under Athena will be discussed.

6.4.1 Digits Creation

The SCT digitization under Athena is unable to digitize hits from GEANT4 at the time of writing this thesis, i.e Release 7.0.0. The reason is the unavailability of the Geant4 geometry description in the digitization. This feature will be added to the digitization package in the near future.
The SCT digitization under Athena can digitze hits from DC1 (Data challenges) Zebra files. These hits were produced by GEANT3 simulation. The files also contain the digits created by Geant3 digitization. Therefore, it is possible to compare the output from the digitization under Athena to the old digits. The digitization gives the RDOs as output into the store gate. The reconstruction is reading its input from the store gate.
For the digitization study a 20 GeV single muons DC1 dataset is used. The DC1 dataset number is 002217. Since the DC1 geometry description is available in the digitization, it is possible to get the digits local and global information. Digits global coordinates in X-Y and R-Z projection are shown in Fig 6.8 (a) and (b). Comparing the digits global coordinates with the hit coordinates in Fig. 6.7, it can clearly be seen in the R-Z projection that the coordinate along the strip (stereo measurement) is not measured by one side of an SCT module and digits are given at the position of the module center in this coordinate (Z in barrel, R in end-caps). The charge generated by 20 GeV muons and the cluster size in the barrel SCT is shown in Fig. 6.9. These results are obtained with modules at 0^0C, 1% bad channels, 10% charge sharing with side strips and 7% charge sharing to the backplane.

[4]A pre-digit is the same as a regular digit. The difference between a digit and pre-digit is that digits cannot be modified by the user where as pre-digits have to be modified by the user.

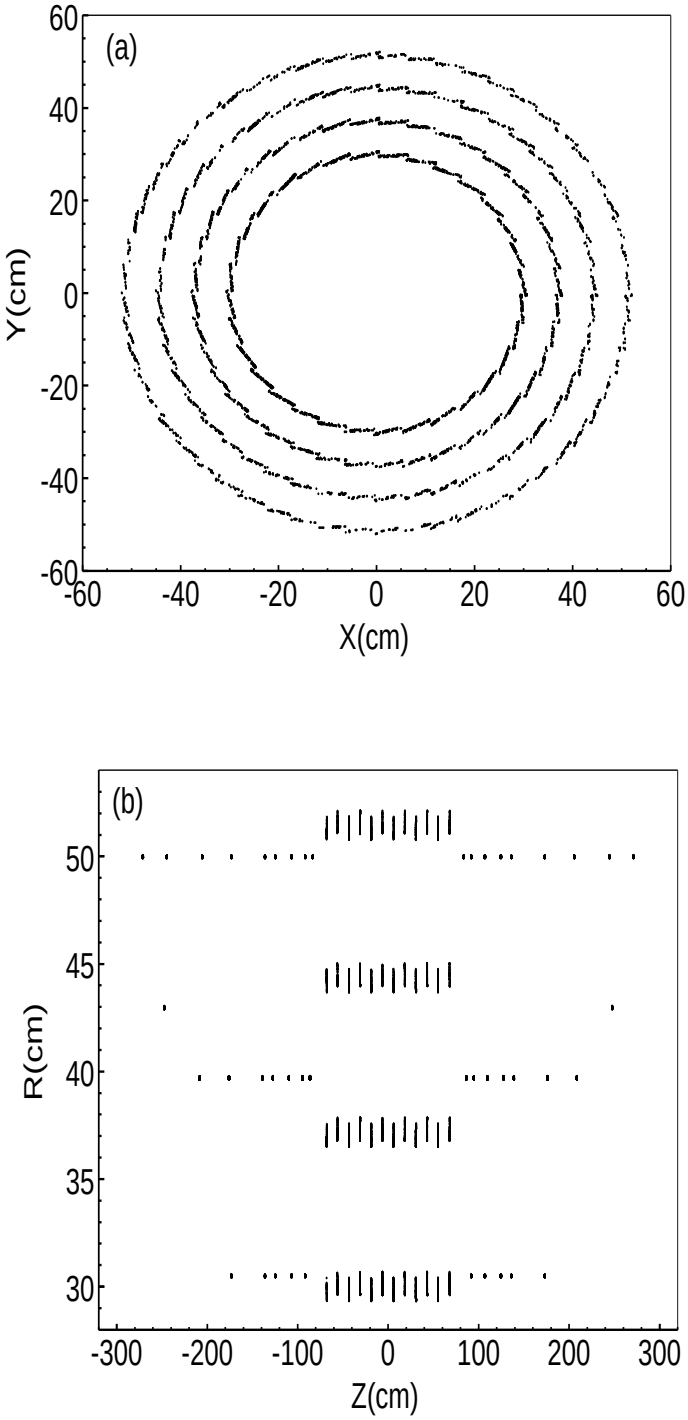

Figure 6.8: SCT Barrel XY view(a) and RZ view(b).

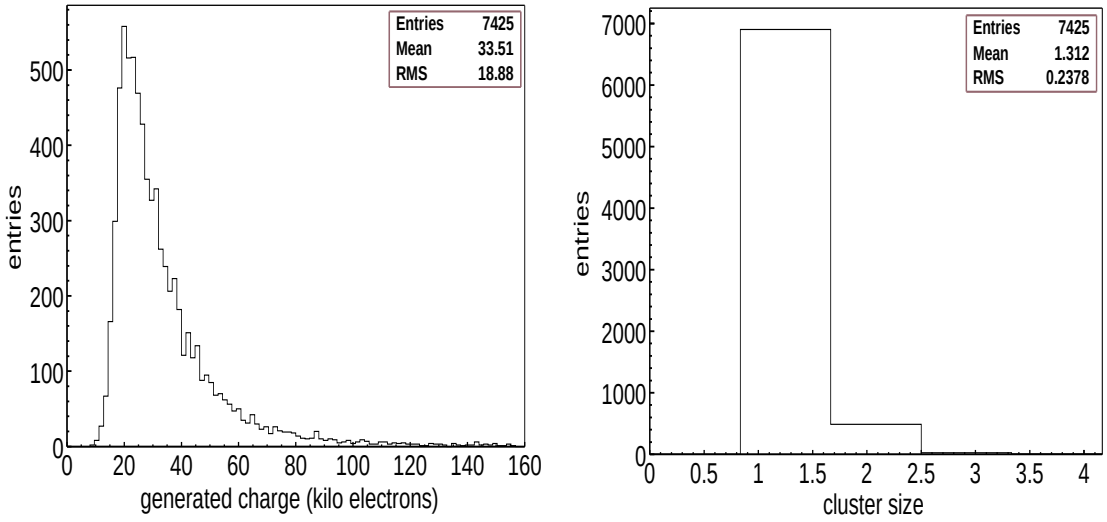

Figure 6.9: Charge generated in barrel SCT (left) and cluster size (right) by 20 GeV muons.

A threshold of 1 fC is applied in SCT binary electronics. A default Gaussian noise sigma of 1875 electrons is included in these plots.

6.4.2 Comparison of the Reconstructed Quantities for the Digitization under Athena and GEANT3 digitization

Tracks are reconstructed using the reconstruction programs described in section 6.2.5. The input to reconstruction are the RDOs from the digitization. The DC1 Zebra files also contain the digits obtained by the GEANT3 digitization. Therefore, GEANT3 digits are also used as input to reconstruction. The reconstruction results obtained from both digitizations are compared in this section.
The output from the reconstruction is the combined ntuple (CBNT). The CBNT allows the output from the different algorithms in the Transient Event Store to be dumped in one common ntuple (hbook or root) and is described in detail under [80]. The ntuple contains information from reconstructed tracks and also truth information from HepMC[5]. Residuals distributions of momentum for RDOs obtained from both digitizations is shown in Fig. 6.10 (a). The residual is defined here as the difference between the reconstructed and generated parameter. For 20 GeV muons there is a difference of 40 MeV in the mean values of the two distributions. To understand the quality of the reconstructed tracks the pull dis-

[5]The HepMC package is an object oriented event record written in C++ for High Energy Physics Monte Carlo Generators. More details can be found in [81] and [82].

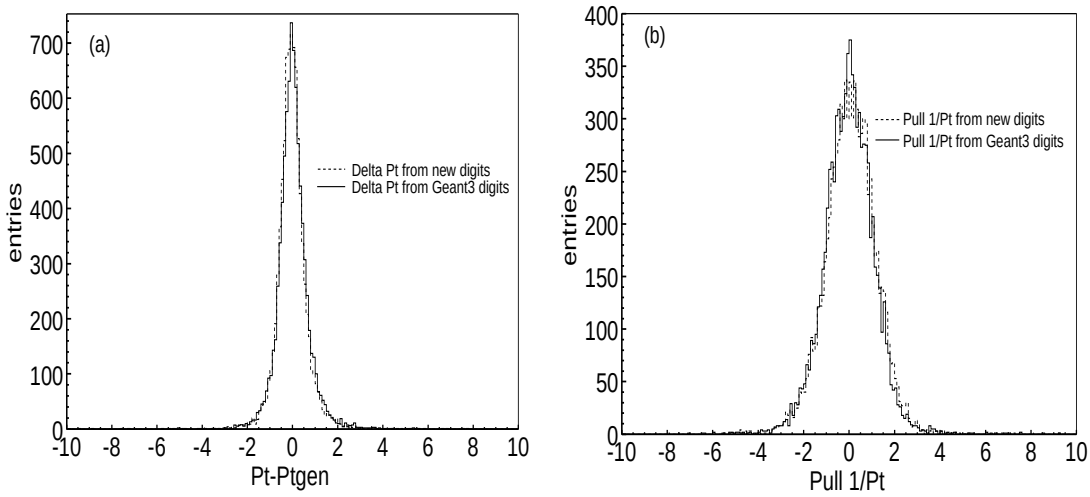

Figure 6.10: (a) Momentum residuals for 20 GeV muons using digits from SCT digitization under Athena and Geant3 digitization. (b) Pulls in 1/Pt for 20 GeV muons, summed over all η using SCT digitization and Geant3 digits.

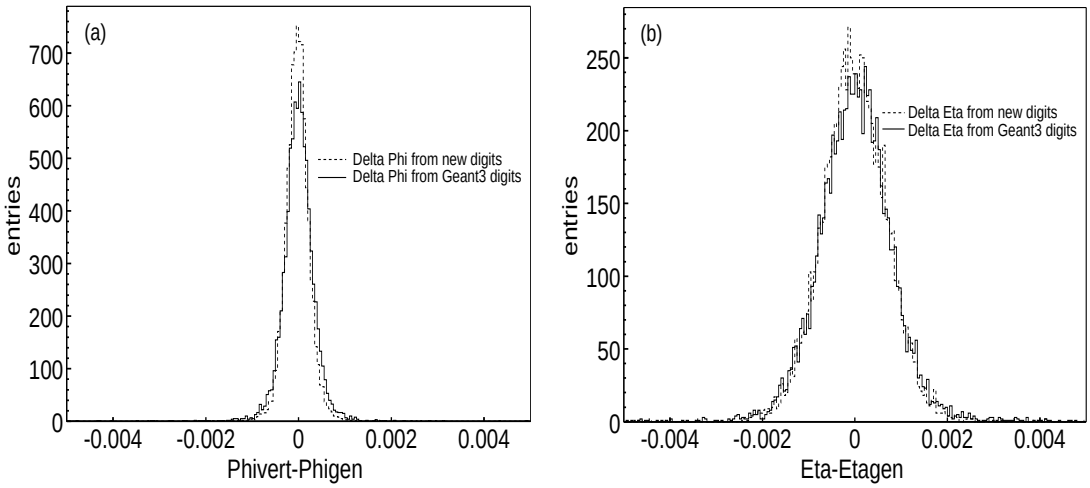

Figure 6.11: (a) Distributions of phi residuals for 20 GeV muons using digits from the SCT digitization under Athena and GEANT3 digitization. (b) Distributions of η residuals for 20 GeV muons.

tribution of $1/p_T$ for 20 GeV muons is shown in Fig. 6.10 (b). The pull is defined as the difference between the reconstructed and generated parameter, normalised by the error on the reconstructed parameter. Although there is a slight difference of the r.m.s of the pulls, it is clear that there are few events in the tails.

The residuals distributions of ϕ and η are shown in Fig. 6.11 (a) and (b). Here ϕ is the angle of the tangent to the track at the point of closest approach to origin

in the transverse plane, with tan$\phi \equiv p_y/p_x$ and the pseudorapidity is defined as η = -ln $tan(\theta/2)$. The matching between the reconstructed quantities using the two different digitization schemes seems reasonable. The digitization plots discussed in the previous subsection and the reconstructed parameters comparison give the confidence to use the digits obtained by using the SCT digitization under the Athena framework as input to reconstruction. The reconstruction results are discussed in the next section.

6.5 Reconstruction Results

The basic aim is to study the effects of increased SCT noise and inefficiency on the single track reconstruction efficiency of the ATLAS Inner Detector. The inefficiency can result from signals below threshold or can also arise from technical reasons: dead electronic cells, bad bonding contacts or pixels (or strips) masked because they are noisy.
In the present study hits for both Pixel and SCT are taken from the single 20 GeV muons DC1 dataset with number 002217 and digitized using Pixel and SCT digitizations respectively. Muons have a Gaussian vertex smearing in x, y and z with $\sigma_x = \sigma_y = 15$ mm and $\sigma_z = 5.6$ cm.
For the Pixel digitization the default job options were used, while for the SCT different noise and inefficiency were simulated. The SCT threshold has a default value of 1fC or 6242 electrons. For the SCT the sigma of the Gaussian noise distribution is by default set to 1875 electrons giving on average 5 in 10^4 strips above the acceptance threshold. The noise and inefficiency were generated only in modules crossed by at least one particle. The SCT inefficiency is simulated by randomly flagging 1% of strips as being inefficient. In the digitization phase the random disabling is done by a processor which iterates on all pre-digits of the given collection and for each of them, sets the disable flag randomly, according to the given probability.
For the TRT the digits are taken directly from the Zebra file.
The SCT inefficiency has been varied from 0% to 25% and the SCT noise sigma has been varied from 0 to 2200 electrons. When varying the detector efficiency the noise sigma is kept constant at the default value and vice versa.
The single muon reconstruction efficiency is used as a measure of the detector performance to study the effect of increased noise and inefficiency.
The single muon reconstruction efficiency is defined as the ratio of accepted reconstructed tracks to total tracks. A reconstructed track is accepted if it has:

(a) At least 7 out of an average of 11 hits (ignoring overlaps) from the precision (Pixel and SCT) layers.

(b) At least 2 out of an average of 3 hits (ignoring overlaps) in the Pixel layers.

(c) An impact parameter[6] $|d_0| < 1$ mm.

The numbers in this definition are somewhat arbitrary. One can in principle define an accepted track so that the single track efficiency is always 100%. However, in addition to finding the muon tracks, the pattern recognition algorithm would also reconstruct many fake tracks. These fake tracks can be due to pile-up tracks in the case of isolated track searches and randomly aligned noise hits. In the present study we took the simplest case of single muons tracks without pile-up and therefore fake tracks are rare and not to be discussed here.
A second definition of efficient tracks is also used in this chapter. This is the so called TDR [20] definition, and is similar to the above efficiency cuts but requires 9 (instead of 7) precision hits and a hit in the B-layer. This definition is the same as used in the TDR and therefore allows comparison with results given in it.
The cuts prove very useful, especially when it is important to ensure that a track comes from the primary vertex or a short-lived particle, such as b-hadron. The cut on the impact parameter mostly rejects decays of long lived particles, conversions and interactions in the detector materials and fake tracks. A cut of 1 mm is chosen so virtually no tracks from B-decays are lost. A hit in the B-layer is required as the impact parameter resolution depends on the hit closest to the interaction point.

6.5.1 Effect of SCT Inefficiency

The muon reconstruction efficiency as a function of pseudorapidity for standard (7 precision hits) and TDR cuts is show in Fig. 6.12 (a) and (b). In this plot the SCT threshold is set to 1 fC or 6424 electrons and the sigma of the Gaussian noise distribution has the default value of 1875 electrons. It can be seen that with increasing SCT inefficiency, efficiency decreases throughout the pseudorapidity coverage. There is a clear overall degradation in the endcap for $|\eta| > 1.5$. This is due to the change in the Pixel layout and improves if the pixel hits cut is relaxed from 2 to 1. The muon reconstruction efficiency as a function of pseudorapidity for standard cuts but 1 hit in pixel layers is shown in Fig. 6.13 (a). The decrease in efficiency with increasing inefficiency is fairly uniform throughout the pseudorapidity coverage. One can conclude that many tracks are passing through gaps in the pixel endcap.
The variations of standard and TDR efficiencies with SCT inefficiency are shown in Fig. 6.13 (b). In this plot the average value of efficiency is plotted in the best pseudorapidity coverage i.e for $|\eta| < 1.5$. In both cases the muon reconstruction efficiency decreases with increasing SCT inefficiency. With the standard cuts the

[6]The minimal orthogonal distance to the z-axis; signed according to the reconstructed angular momentum of the track about the axis.

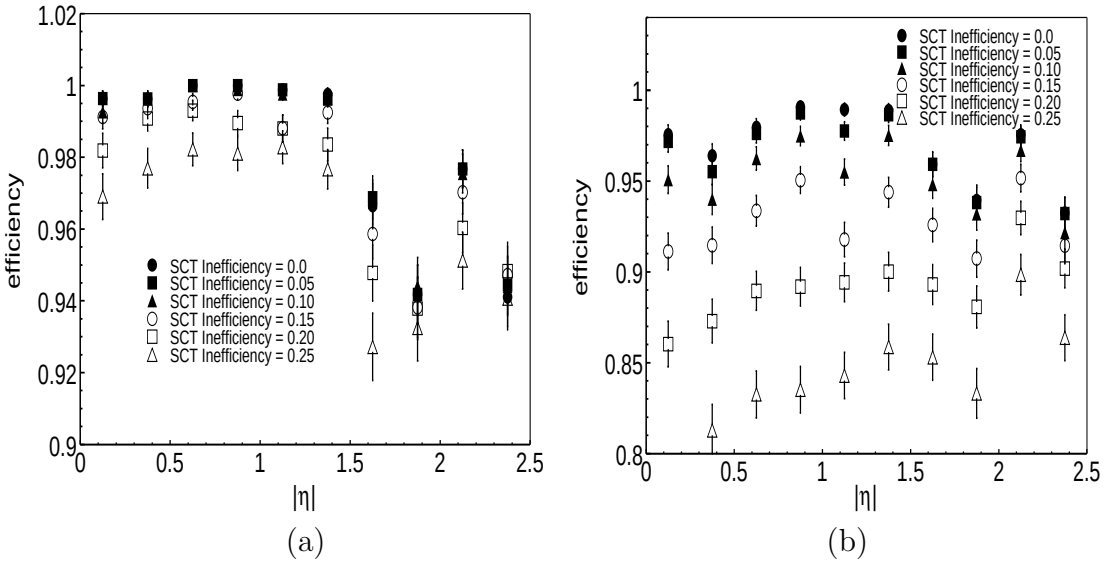

(a) (b)

Figure 6.12: Efficiency for finding muons versus pseudorapidity for different SCT inefficiencies. Standard cuts(7 precision hits) (a) and TDR cuts(9 precision hits with 1 hit in B-layer) (b).

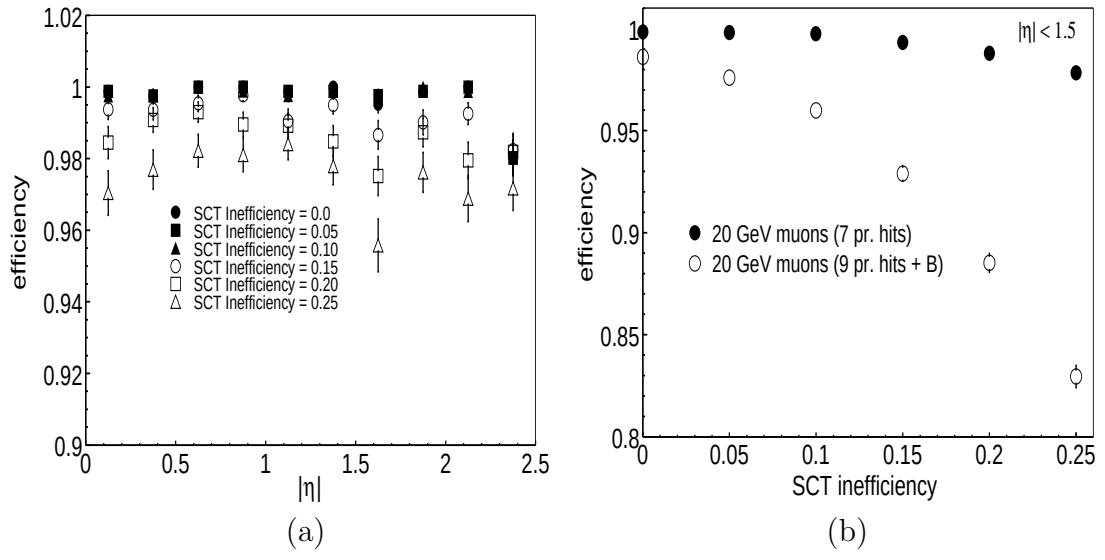

(a) (b)

Figure 6.13: Efficiency for finding muons versus η for different SCT inefficiencies with standard cuts but 1 pixel hit (a). Efficiency versus SCT inefficiency with both standard and TDR cuts (b).

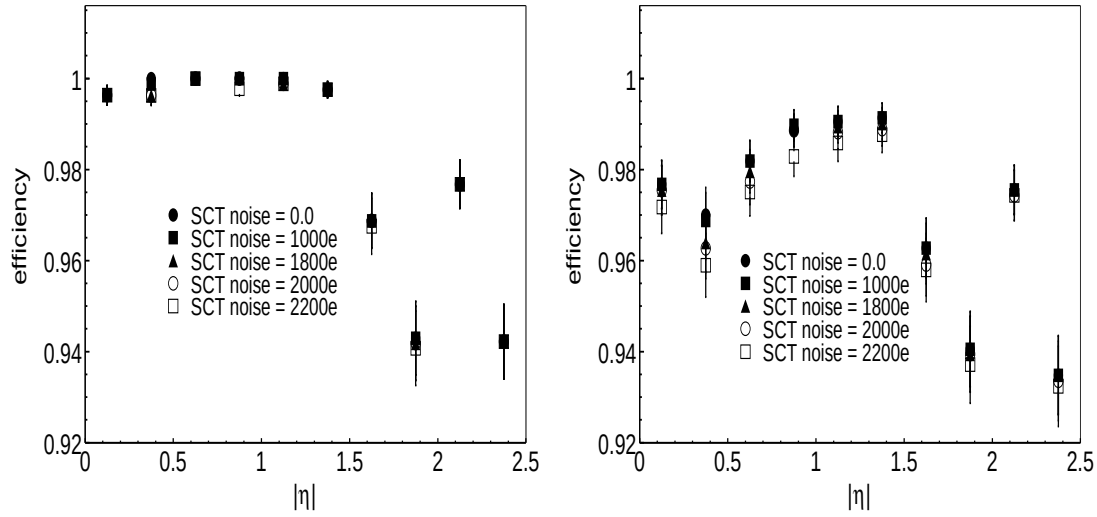

Figure 6.14: Efficiency for finding muons as a function of η for different SCT noise (a) with standard cuts and TDR cuts (b).

efficiency is above the 95% specification level even at 25% SCT inefficiency. For the TDR cuts the efficiency falls to the 95% specification value around 11% SCT inefficiency.

6.5.2 Effect of Increased SCT Noise

To see the effects of increased SCT noise on the single muon reconstruction efficiency, the SCT inefficiency is set to the default value of 1%. The threshold is set to the default value of 1 fC and the noise sigma is increased from 0 to 2200 electrons (0.35 fC). A noise of 2200 electrons will give rise to 0.5% noisy channels at the SCT default threshold of 1 fC.
Fig 6.14 shows the muon reconstruction efficiency as a function of pseudorapidity for different SCT noise values. Fig 6.14 (a) is obtained with standard cuts and Fig 6.14 (b) with the TDR cuts. In both cases, the efficiency is not much affected by the increase in SCT noise up to a maximum of 2200 electrons.
It should be noted that the maximum permissible noise will be determined by the fake rates, not by the efficiency. The reason is that, with a higher fraction of strips above threshold, the probability of forming fakes will increase. It is therefore essential that a study of single track efficiency is complemented by a study of fake rates.
The efficiency of finding muons as a function of different SCT noise values is shown in Fig. 6.15. It can be seen that for both the standard and TDR cuts the efficiency is above the specification value of 95% up to the maximum noise of 2200 electrons.

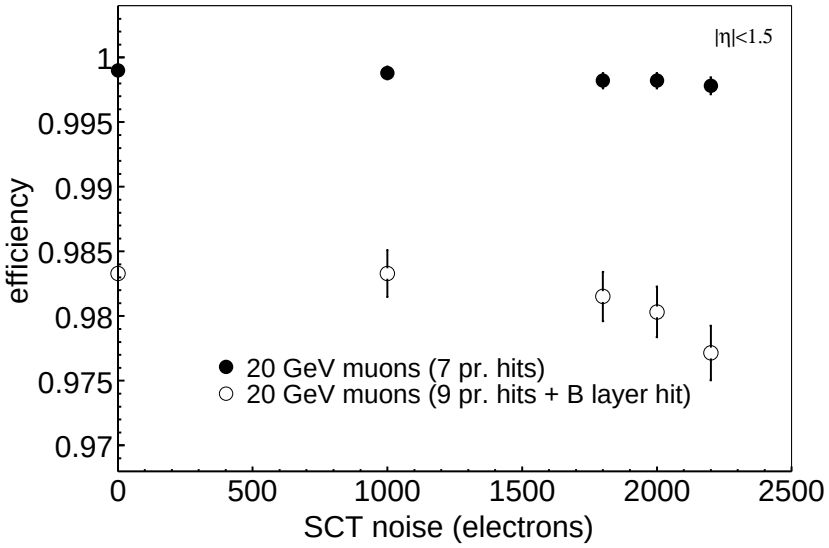

Figure 6.15: Efficiency as a function of noise for 20 GeV muons.

6.5.3 Precision Hits

The specification on the number of precision hits (space-points) is ≥ 5 for $\eta \leq 2.5$ and this should be satisfied for the complete lifetime of ATLAS. The layout of the precision detectors was designed so that a stiff track would cross ≥ 2 pixel layers and ≥ 4 SCT stereo layers. In addition the B-layer will provide an extra space-point for as long as is technically feasible.
To get a feeling of how the inefficiency affects the number of precision hits (space-points), the average number of precision hits as a function of pseudorapidity is shown in Fig. 6.16 (a). It should be noted that a default value of 1% inefficiency and a noise charge of 1875 electrons is included in this plot. It is clear that there is a degradation in the Pixels in the endcap. Many tracks are passing through the gaps and do not create any hit. In this plot less than 2 hits in the Pixel layers are not visible because the of hits is averaged over $|\eta|$.
By design there is an increasing number of precision hits at large $|\eta|$ to compensate for the loss of bending power and to cope with the non-uniformity of the solenoidal magnetic field as clear in Fig. 6.16 (a). The decrease in the number of precision hits as a function of inefficiency is shown in Fig. 6.16 (b). The number remains above the specification value. This again is a proof of the robustness of the Inner Detector to increased SCT inefficiency.

6.5.4 Discussion

The SCT/Pixel digitization under Athena can read DC1 hits and gives its output as RDOs. The results of the digitization can be filled into a ntuple by reading

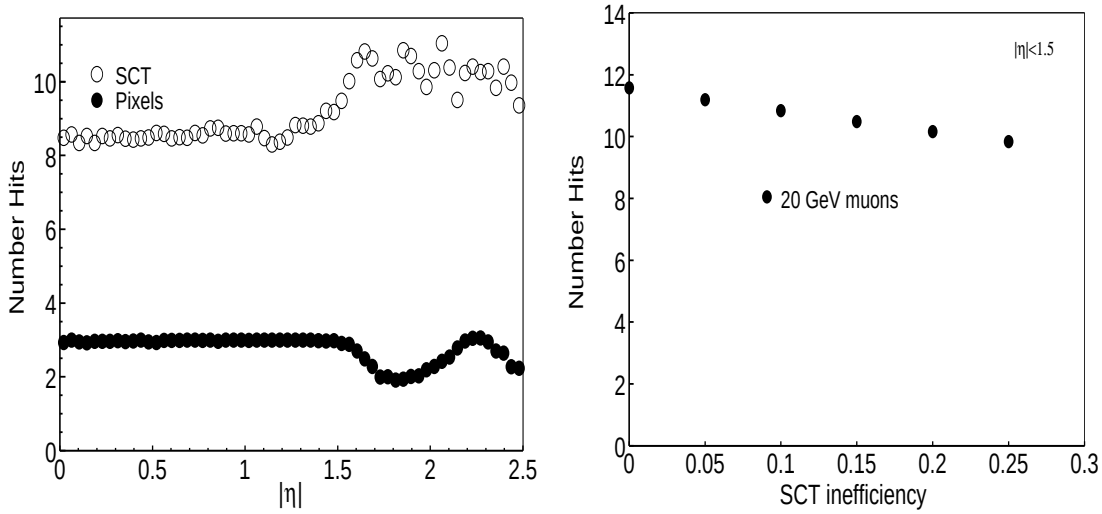

Figure 6.16: (a) Number of hits seen for 20 GeV muon tracks in the precision layers. (b) Number of precision hits versus SCT inefficiency.

the RDOs or can be linked to reconstruction. The comparison between the SCT digitization under Athena and the GEANT3 digitization has been done and the results from both digitizations are similar.
The effects of increased SCT noise and inefficiency on the single track reconstruction efficiency have been studied. The DC1 layout shows a degradation in the Pixel layout where many tracks can pass through the gaps. The single track reconstruction efficiency decreases to the specification value of 95% for SCT inefficiency of around 11% in the range $|\eta| < 1.5$. It should be noted that inefficiency is introduced in an unrealistic way by randomly killing strips. In the real detector the inefficiency might be caused by dead readout chips, which will result in more correlated inefficiency. The increased noise does not have a significant effect on single track reconstruction efficiency up to a maximum of 0.5% noisy channels.

Summary and Conclusion

The ATLAS detector will surround one of the four interaction points of the Large Hadron Collider at CERN. ATLAS is a multi-purpose detector and is designed to discover and investigate a wide range of possible new physics.
The ATLAS Semi-Conductor Tracker (SCT) is positioned in between the other two tracking detectors (Pixel and TRT). The SCT will provide precision tracking for charged particles using silicon micro-strip detectors. The active elements of the SCT, 4088 detector modules, will be tiled on four barrel cylinders and eighteen end-cap disks. The silicon sensors of each module have strip layout and are readout by twelve front-end ASICs featuring binary readout. The performance of the SCT system mainly depends on two parameters, which are noise occupancy and detection efficiency. Both of these parameters deteriorate with increasing noise in the system. If the noise occupancy grows, more hits that are not associated to any track will be found which will increase the fake track rate. Reading out more data can cause buffer overflows and hence inefficiencies in the read-out chain. It is therefore very important to understand the effects of noise and to develop efficient methods to minimize it.

It is known that silicon detectors contribute to total noise (ENC) mainly via their capacitances. Capacitance measurements on silicon micro-strip detectors are described. A detailed description of the effects of noise on the SCT modules with binary readout is given. The efficiency of a SCT module is calculated using a Landau distribution and its convolution with a Gaussian. The width of the window between thresholds corresponding to efficiency and noise occupancy specifications is calculated. The calculation predicts that the efficiency will not be affected if the threshold is increased after 10 years of ATLAS operation in order to keep a clean signal. However, testbeam measurements on irradiated modules indicate, that after 10 years of operation the margin of operation will actually be smaller than predicted by the model, which must be attributed to more complicated charge collection and loss mechanisms.

Common mode noise is of particular concern in binary read-out systems as it can not be measured on an event-by-event basis. Methods to measure common mode noise in binary read-out systems are described. An observable Γ is introduced,

which is derived from the standard deviation of the number of hits per event and at 50% occupancy directly gives the common mode noise contribution. The Γ gives a quantitative estimate of the common mode noise and is computationally very simple to evaluate. A method to calculate common mode noise from the observable Γ at arbitrary occupancy is also given. A parametrization for Γ as a function of occupancy and common mode noise is given which fits the numerical simulation within $\pm 2\%$ over a wide range of occupancy and common mode noise levels. The statistical uncertainty of Γ has been analyzed, it is shown that a data sample should contain at least 500 events in order to obtain a Γ value and there-by a common mode noise estimate with less than 4% statistical uncertainty.

A part of the work on common mode noise is published already in Nuclear Instrument and Methods section A [57]. The remaining part will be published as ATLAS note.

Methods for measurements of common mode noise in binary read-out system have been successfully applied to ATLAS SCT end-cap modules. These methods are now in use in the SCT community to measure the common mode noise contribution. Software for the implementation of these methods is available as a part of the SCT DAQ.

A Geant4 based simulation for the SCT is performed under the Athena framework. It is shown that mainly secondary hits contribute to low energy tails of the Landau distribution. The comparison between the SCT digitization under Athena and Geant3 digitization has been made. For 20 GeV muons there is a difference of 40 MeV between the mean values of the momentum residual distributions.

The effects of increased SCT noise and inefficiency on the single track reconstruction efficiency have been studied. The DC1 geometry shows a degradation in the Pixel layout where many tracks can pass through the gaps. The single track reconstruction efficiency decreases to the specification value of 95% for SCT inefficiency of around 11% in the range $|\eta| < 1.5$. The increased SCT noise does not have a significant effect on the single tracks reconstruction efficiency up to a maximum of 0.5% noisy channels.

Bibliography

[1] S. Weinberg, *A model of leptons*, Phys. Rev. Lett. **19** (1967) 1264-1266.

[2] A. Salam, *Weak and electromagnetic interactions*, 1969. *Proc. of the 8th Nobel Symposium on 'Elementary particle theory, relativistic groups and analyticity', Stockholm, Sweden, 1968*, edited by N. Svartholm, p.367-377.

[3] S. Glashow, *Partial symmetries of weak interactions*, Nucl. Phys. **22** (1961) 579-588.

[4] P. Higgs, *Broken symmetries and the masses of gauge bosons*, Phys. Rev. Lett. **13** (1964) p:508.

[5] P. Higgs, *Spontaneous symmetry breakdown without massless bosons*, Phys. Rev. **145** (1966) p:1156.

[6] F. Englert and R. Brout, *Broken symmetry and the mass of gauge vector mesons*, Phys. Lett. **13** (1964) p:132.

[7] S. Myers, *The LEP collider from design to approval and commissioning*, Yellow Report, CERN-1991-008 (1991).

[8] LEP Higgs Working group, *Searches for the neutral Higgs bosons of the MSSM: Preliminary combined results using LEP data collected at energies up to 209 GeV*, hep/ex-0107030 (2001).

[9] LEP Electrowral Working Group, *A combination of preliminary electroweak measurements and constraints on the standard model* (2001).

[10] Y. Fukuda et al., *Evidence for oscillation of atmospheric neutrinos*, Phys. Rev. Lett. **81** (1998) 1562-1567.

[11] S. Fukuda et al., *Constraints on neutrino oscillations using 1258 days of Super-Kamiokande solar neutrino data*, Phys. Rev. Lett. **86** (2001) 5656-5660.

[12] Q. R. Ahmad et al., *Measurement of the Rate of* $\nu_e + d \longrightarrow p + p + e^-$ *Interactions produced by B-8 solar neutrino at the Sudbury Neutrino Observatory*, Phys. Rev. Lett. **87** (2001) 071301.

[13] LHC study group, *The LHC conceptual design report*, CERN-AC-95-05, (1995).

[14] ATLAS Collaboration, Technical Proposal, CERN/LHCC/94-43, (1994).

[15] CMS Collaboration, *The Compact Muon Solenoid*, Technical Proposal, CERN/LHCC/94-38, CERN, (1994).

[16] ALICE Collaboration, *A Large Ion Collider Experiment at LHC*, Technical Proposal, CERN/LHCC/95-71, CERN, (1995).

[17] LHC-B Collaboration, *A Large Hadron Collider Beauty Experiment for the Precision Measurements of CP Violation and Rare Decays*. Technical Proposal, CERN/LHCC/98-4, CERN, (1998).

[18] ATLAS Collaboration *ATLAS Detector and Physics Performance Technical Design Report volume 1*. CERN/LHCC/99-14, CERN, (1999).

[19] ATLAS Collaboration, *ATLAS Detector Physics Performance Technical Design Report volume 2*. CERN/LHCC/99-15, CERN, (1999).

[20] *ATLAS Inner Detector Technical Design Report volume 1.* CERN/LHCC/97-16, (1997).

[21] *ATLAS Inner Detector Technical Design Report volume 2.* CERN/LHCC/97-17, (1997).

[22] *ATLAS Liquid Argon Calorimeter, Technical Design Report*, CERN/LHCC/96-41, CERN, (1996).

[23] *ATLAS Tile Calorimeter, Technical Design Report*, CERN/LHCC/96-42, CERN, (1996).

[24] *ATLAS Muon Spectrometer, Technical Design Report*, CERN/LHCC/97-22, CERN, (1997).

[25] *ATLAS First-Level Trigger, Technical Design Report*, CERN/LHCC/97-14, CERN, (1998).

[26] *DAQ, EF, LVL2 and DCS Technical Design Report*, CERN/LHCC/97-16, CERN, (1998).

[27] *ATLAS SCT Barrel Module Final Design Review*, (2001).
`http://atlas.web.cern.ch/Atlas/GROUPS/INNER_DETECTOR/SCT/module/SCTbarrelmod.html`

[28] ATLAS SCT Endcap Module Final Design Review, (2002).
`http://sct.physik.uni-freiburg.de/feld/sct/module/FDR.htm`

[29] G. Lutz, *SemiConductor Radiation Detectors*, Springer-Verlag (1999).

[30] E. Barberis et al., *Temperature effects on radiation damage to silicon detectors*, Nucl. Instr. and Meth. **A 326** (1993) 373-380.

[31] H. J. Ziock, et al., *Temperature Dependence of Radiation Damage and its Annealing in Silicon Detectors*, IEEE Trans. Nucl. Sci. **40** (1993) p:344.

[32] W. Dabrowski et al., *Design and performance of the ABCD chip for the binary readout of silicon strip detectors in the ATLAS Semiconductor Tracker*, IEEE Trans. Nucl. Sci. **47** (2000) 1843-1850.

[33] W. Dabrowski et al., *Progress in development of the readout chip for the ATLAS Semiconductor Tracker*, *Cracow 2000, Electronics for LHC Experiments*, (2000) 115-119.

[34] *ABCD3T ASIC Requirements and Specification*, Vol. SCT-ASIC-PRR,(2001).
`http://sct.physik.uni-freiburg.de/feld/sct/module/FDR.htm`

[35] M. Dentan et al., *Dmill (durci mixte sur isolant logico-lineaire): A mixed analog-digital radiation hard technology for high energy physics electronics*, Nucl. Phys. Proc. Suppl. **32**, (1998) 530-534.

[36] J. Kaplon et al., *DMILL implementation of the analogue readout architecture for position sensitive detectors at LHC experiments*, *Presented at the 2nd Workshop on Electronics for LHC Experiments, Rome, Italy, (1998)*, p:21-25.

[37] F. Anghinolfi. et al., *SCTA- A Rad-Hard BiCMOS Analogue Readout ASIC for the ATLAS Semiconductor Tracker*, IEEE Trans. Nucl. Sci. **44** (1997) 298-302.

[38] P. Riedler. *Radiation damage effects and performance of silicon strip detector using LHC readout electronics*, Ph.D. thesis, CERN, (1998).

[39] S. Peeters, `The ATLAS SemiConductor Tracker Endcap`, Ph.D. thesis, NIKHEF, (2003).

[40] L. Feld, *Forward modules components*, ATL-IS-EN-0009.
`https://edms.cern.ch/document/316211`

[41] *LabView User Manual*, National Instruments, (2001).
`http://www.ni.com/pdf/manuals/320999d.pdf`

[42] D. W. Aitken et al., Phys. Rev. **179** (1969) 393.

[43] E. M. Bellamy, et al., Phys. Rev. **164** (1967) 417.

[44] H. D. Maccabee et al., Phys. Rev. **165** (1968) 469.

[45] S. Hancock et al., Phys. Rev. A **28** (1983) 615.

[46] L. Landau, J. Phys.(Moscow) **8** (1944) 201.

[47] H. Bichsel, Rev. Mod. Phys. **60** (1988) 615.

[48] H. Bichsel, Phys. Rev. A **11** (1975) 1286.

[49] R. Brun and F. Rademakers, *ROOT-an Object Oriented data analysis framework*, Nucl. Instr. and Meth. A **389** (1996) 81-86.
`http://root.cern.ch/`

[50] K. S. Klbig and B. Schorr, *A program package for the Landau distribution*, Computer Phys. Comm. **31** (1984) 97-111.

[51] C. Lacasta et al., *Electrical results from prototype Modules* (2002).
`http://ific.uv.es/ lacasta/ElectricTeam/FDR/FDR-Electrical_results.pdf`

[52] M. Vos et al., *Charge collection with binary readout from a test beam perspective*, *ATLAS Internal Note*, ATL-INDET-2003-011.

[53] G. F. Moorhead et al., *Beam tests of ATLAS SCT silicon strip detector prototypes*, to be published in Nucl. Instr. and Meth. A.

[54] Larry C. Andrews, *Special Functions of Mathematics for Engineers*, Oxford University Press, ISBN 0-8194-2616-4.

[55] Alexander Apelblat, 'Table of Definite and Infinite Integrals', Elsevier (1983).

[56] K. G. Beauchamp, 'Signal Processing Using Analog and Digital Techniques', publ. George Allen & Unwin, (1973).

[57] L. Feld, S. Roe, A. Ahmad and S. Snow, Nucl. Instr. and Meth. A **487** (2002) 557-564.

[58] Philip R. Bevington, *Data Reduction and Error Analysis for the Physical Sciences*, McGraw-Hill, Inc., New York, second edition (2003).

[59] M. Morrisey and M. Goodrick, MuSTARD (1998).
http://hepwww.rl.ac.uk/atlas-sct/mm/Mustard/MUSTARD.PS

[60] M. Postranecky, CLOAC.
http://www.ucl.ac.uk/atlas/sct/cloac/Welcome.html

[61] M. Morrisey, SLOG.
http://hepwww.rl.ac.uk/atlas-sct/mm/Slog/SLOG.PS

[62] J. Stastny, SCTLV.
http://www-hep2.fzu.cz/Atlas/WorkingGroups/Projects/MSGC.html

[63] E. Gornicki, SCTHV.
http://www-hep2.fzu.cz/Atlas/WorkingGroups/Projects/MSGC.html

[64] P. Phillips et al., *Electrical Tests of SCT Hybrids and Modules*, ATL-COM-INDET-2003-004.

[65] A. Clark, et al., *The ATLAS SCT Production Database*, ATL-INDET-2002-015.
http://wacap.unige.ch:3146/phyprdwww/sctprd/welcome.html

[66] *E03 module Electrical Tests*.
http://james.physik.uni-freiburg.de/~atlas/sct/module_assembly/Documents/E03/E03.htm

[67] *Athena The ATLAS Common Framwork*, *User Guide and Tutorial*, Version 2, (2001).

[68] Data Challenge 1, N. A. McCubbin and G. Poulard, ATL-ENEWS-2001-094.
http://atlas.web.cern.ch/Atlas/GROUPS/SOFTWARE/DC/DC1/

[69] Atlas CVS Repository.
http://atlas-sw.cern.ch/cgi-bin/cvsweb.cgi/

[70] S. Agostinelli et al., *Geant4 Collaboration*, *GEANT4: A Simulation Toolkit*, Nucl. Instr. and Meth. A **506** (2003) 250-303.
http://geant4.web.cern.ch/geant4/

[71] FADS/Goofy, *Atlas Detector Simulation Framework*.
http://atlas.web.cern.ch/Atlas/GROUPS/SOFTWARE/OO/domains/simulation/

[72] xKalman++ in Athena.
`http://maupiti.lbl.gov/atlas/xkal/`

[73] R. Clifft and A. Poppleton, *IPATREC: inner detector pattern-recognition and track-fitting*, ATL-SOFT-94-009, (1994).
`http://pop.home.cern.ch/pop/iPatRec.html`

[74] *Gaudi Developers Guide*. version 2 (2001).
`http://proj-gaudi.web.cern.ch/proj-gaudi`

[75] S. Gadomski, *SCT Digitization Package*.
`http://gadomski.home.cern.ch/gadomski/SCT_Digitization.html`

[76] D. Calvet, *Silicon trackers digitization framwork*, ATL-SOFT-2001-006, 18 Sep 2001.

[77] S. Gadomski, ATL-SOFT-2001-005, (2001).

[78] Inner Detector Simulation webpage.
`http://atlas.web.cern.ch/Atlas/GROUPS/INNER_DETECTOR/SOFTWARE/Simulation/IDSim.html`

[79] P. Billoir, Nucl. Instr. and Meth. A **225** (1984) 352.

[80] CBNT in Athena.
http://atlas.web.cern.ch/Atlas/GROUPS/SOFTWARE/OO/domains/Reconstruction/packages/CBNT_Athena/CBNT_Athena.htm

[81] M. Dobbs and J. B. Hansen, Comput. Phys. Commun. **134** (2001) 41.

[82] HepMC web page, http://cern.ch/HepMC

Acknowledgements

I would like to thank many people who made my Ph.D time stimulating and enjoyable.

Firstly, I would like to thank my supervisor Prof. Dr. Kay Runge, who offered me the opportunity to carry out the research that has led to this thesis.

I would like to thank PD. Dr. Lutz Feld for introducing me to the exciting field of silicon detectors as well as stimulating discussions, continuous support and expertly guiding me through my Ph.D work. And especially for his patience in answering to my questions. I simply learned a lot from him.

I wish to thank Prof. Dr. Karl Jakobs for his support, especially for allowing me to continue my work, and to use the departmental facilities.

I had fruitful discussions with Prof. Dr. Jens Ludwig especially on topics related to the MEDIPIX project and would like to thank him for his help and guidance.

I wish to thank Dr. Ulrich Parzefall for his support and help during my thesis. He is always ready to help whenever you happen to need it.

I am indebted to Dr. Davide Costanzo at BNL and Dr. Grant Gorfine at NIKHEF for their help and guidance on simulation and software related topics.

Thanks also to all my colleagues, Christian Ketterer, Dr. Jens Meinhardt, Simon Eckert, Dieter Joos, Markus Webel, Carmen Carpentieri and many more for making my stay in Freiburg an enjoyable one, and having contributed to friendly and pleasant working atmosphere.

Finally, I would like to thank my wife for her patience and understanding especially during the last months of my thesis.